6-2013

Zone of Intrusion for Permanent 9.1-degree Single Slope Concrete Barriers

Cale J. Stolle
University of Nebraska-Lincoln, cale.stolle@huskers.unl.edu

ZONE OF INTRUSION FOR PERMANENT 9.1° SINGLE-SLOPE CONCRETE BARRIERS

by

Cale Stolle

A THESIS

Presented to

The Graduate College at the University of Nebraska

In Partial Fulfillment of Requirements

For the Degree of Master of Science

Major: Mechanical Engineering and Applied Mechanics

Under the Supervision of Professor John D. Reid

Lincoln, Nebraska

May 2013

ZONE OF INTRUSION FOR PERMANENT 9.1° SINGLE-SLOPE CONCRETE BARRIERS

Cale Stolle M.S.

University of Nebraska, 2013

Advisor: John D. Reid

Three WDOT 9.1-degree single-slope concrete barriers, with top heights of 36 in. (914 mm), 42 in. (1,067 mm), and 56 in. (1,422 mm) (Standard 14B32), were analyzed for Zone of Intrusion (ZOI)' and working width using nonlinear finite element analysis (FEA). Tire-barrier friction, vehicle-barrier friction, barrier stiffness, mesh size, tire deflation, and suspension component failures were all found to have effects on simulation results. The zone of intrusion and working width were evaluated for each barrier under varying tire deflation and suspension failure conditions and determined to have a maximum value of 12.2 in. (310 mm) for the front fender and 9.4 in. (240 mm) for the rest of the vehicle. The working width for each barrier was determined to be 24 in. (610 mm).

Dedication

In the course of my studies, I have encountered many people who have inspired me and pushed me to grow and learn. I want to thank Jesus Christ for his sacrifice and willingness to do the impossible out of love. His influence has driven me my whole career, and will continue to drive me far into the future.

I would also like to thank my family for their continued support and strength, for instilling in me the virtues I have and pushing me always to improve. I would like to give a special thanks to my nephew Jojo for his hugs and creativity. You've shown me that even the littlest among us can inspire us.

To all the staff at the Midwest Roadside Safety Facility, I would like to thank you for your work to improve roadside safety research for the good of drivers everywhere. Advancements that you have made are saving lives already, and you work to teach others and promote safety everywhere. You have helped train me and instilled a desire in me to help others that will not soon pass.

I'd like to thank the Wisconsin Department of Transportation for funding this effort and for showing a proactive role in performing research in critical areas of roadside safety.

To the many friends, professors, classmates, and co-conspirators – thank you for putting your effort into working alongside me to help me grow as an individual.

TABLE OF CONTENTS

Dedication iii

TABLE OF CONTENTS iv

List of Figures vii

List of Tables ix

1 INTRODUCTION 1
- 1.1 Background 1
- 1.2 Project Objective 2

2 PROCEDURE 3

3 LITERATURE REVIEW 4
- 3.1 Introduction 4
- 3.2 Concrete Barrier Testing History 4
- 3.3 ZOI Studies 6
  - 3.3.1 ZOI Values from NCHRP Report No. 350 Testing 14
  - 3.3.2 ZOI Values from MASH Testing 15
- 3.4 In-Depth Suspension Behavior Analysis 17
  - 3.4.1.1 Damage Documentation 18
  - 3.4.1.2 Damage Interpretation 26
  - 3.4.1.3 Damage Summary 27
- 3.5 Suspension Damage for 2270P Pickup Trucks 27
  - 3.5.1 Free-Standing, Restricted-Motion, and Permanent Barrier Systems 30
  - 3.5.2 Vehicle Climb Up the Barrier 34

4 SIMPLIFIED VEHICLE MODEL 39
- 4.1 Simplified Model Setup 39
- 4.2 Simplified Model Stages 40
- 4.3 Pre-Contact Stage 40
  - 4.3.1 Force List 40
- 4.4 Impact Stage 41
  - 4.4.1 Force List 41
  - 4.4.2 Moments Caused by Impact Stage Forces 42
- 4.5 Tailslap Stage 43
  - 4.5.1 Force List 43
  - 4.5.2 Moments Caused by Tailslap Stage Forces 44
- 4.6 Airborne Stage 45
- 4.7 Ground Contact Stage 45

5 SIMULATIONS OF THE 2270P SILVERADO INTO THE 10.8-DEGREE SINGLE-SLOPE BARRIER 47

5.1 Introduction 47
5.2 Section Objective 47
5.3 Model Development Considerations 47
5.4 Test No. 420020-3 Details 48
5.5 Mesh Size 51
5.6 Comparison to Full-Scale Test Results 55
5.7 Parameter Studies 57
5.8 Tire-to-Barrier Friction Coefficient 58
5.8.1 Vehicle Vertical Displacement 59
5.8.2 Roll Angle 61
5.8.3 Pitch Angle and Analysis 62
5.8.4 Yaw Angle 66
5.8.5 Angular Comparison Between Test and Simulation 67
5.8.6 ZOI Results for Tire Friction Simulations 68
5.8.7 Recommended Tire-to-Barrier Friction Coefficient 73
5.9 Vehicle Body-to-Barrier Friction Coefficient 73
5.9.1 Vehicle Vertical Displacements 74
5.9.2 Roll Angle 75
5.9.3 Yaw Angle 77
5.9.4 Pitch Angle 77
5.9.5 Contact Force Analysis 78
5.9.6 ZOI Results for Vehicle Friction Simulations 81
5.9.7 Recommended Vehicle-to-Barrier Friction Coefficient 82
5.10 Elastic Barrier Study 83
5.10.1 Conclusions 90

6 ZOI SIMULATION MODELS 91

7 ZONE OF INTRUSION ANALYSIS 93
7.1 Baseline Evaluation 93
7.1.1 Vehicle C.G. Height 93
7.1.2 Contact Force Analysis 94
7.1.3 Roll Angle 95
7.1.4 Yaw Angle 97
7.1.5 Pitch Angle 97
7.1.6 Suspension Damage 98
7.1.7 Zone of Intrusion Results 100
7.2 Simulation with Tire Deflation 102
7.2.1 Simulation Results 103
7.2.2 Vehicle Trajectory 104
7.2.3 Zone of Intrusion Analysis 105
7.2.4 Tire Deflation Recommendation 106
7.3 Suspension Joint Failure Models 106
7.4 Zone of Intrusion for Wisconsin 9.1-Degree Single-Slope Barriers 113
7.5 Working Width Analysis 113

8 SIMULATED OCCUPANT RESEARCH 116
8.1 Introduction 116
8.2 Simulated Occupant Model Components 117
8.2.1 Dummy Occupant Model 117
8.2.2 Seat Model 118
8.2.3 Seatbelt Model 118
8.3 Seat Stability and Acceleration 119
8.4 Occupant-In-Seat Model 121
8.4.1 Hourglassing and Element Formulation 123
8.5 Seatbelt Stability and Acceleration 124
8.6 Seatbelt and Simulated Occupant 125
8.6.1 Seatbelt Model with Beam Elements 125
8.6.2 Seatbelt Model with Shell Elements Fixed to Seat 126
8.7 Implementation into the Vehicle 128
8.7.1 Model Description 128
8.7.2 Simulation Results 129
8.7.3 Head Protrusion Out of Vehicle 132
8.7.4 Seatbelt Forces 134
8.7.5 Impact Between the Occupant and the Door 135
8.8 Comparison with the Baseline 136
8.8.1 Vehicle Vertical C.G. Displacement 136
8.8.2 Vehicle Roll Angle 138
8.9 Conclusions and Future Work 139
8.10 Disclaimer 141

9 CONCLUSIONS 142

10 FUTURE WORK 143
10.1 Concrete Barrier Research 143
10.2 Vehicle and Vehicle Model Research 144
10.3 ZOI Research 145
10.4 Dummy Occupant Research 146

11 REFERENCES 148
Appendix A. 2000P SIMULATIONS WITH THE F-SHAPE BARRIER 152
Appendix B. C2500 VEHICLE ANTI-ROLL BAR RESEARCH 159

List of Figures

Figure 1. Hazards Located Within the Zone of Intrusion 7
Figure 2. Zone of Intrusion Tests ZOI-1, ZOI-2, and ZOI-3 [11] 9
Figure 3. Head Ejection Envelope [12] 11
Figure 4. Impacting a Bridge Pier in the ZOI 13
Figure 5. Dodge Ram Hood and Fender Geometry 17
Figure 6. Chevy Silverado Hood and Fender Geometry 17
Figure 7. Inside of Wheel Damage, Test No. PCMB-1 20
Figure 8. Outside of Wheel Damage, Test No. PCMB-1 21
Figure 9. Lower Control Arm Damage, Test No. PCMB-1 22
Figure 10. Lower Control Arm Connection Slip, Test No. PCMB-1 23
Figure 11. Bump Stop and Upper Control Arm Damage, Test No. PCMB-1 24
Figure 12. Roll Bar and Connecting Pin Damage, Test No. PCMB-1 25
Figure 13. Types of Concrete Barrier Systems 32
Figure 14. Post-Impact Trajectories of F-Shape Concrete Barrier Crash Tests 36
Figure 15. Impacting Tire Ride-Up for Different Full-Scale Crash Tests 37
Figure 16. Unbalanced Forces During the Initial Impact Stage 39
Figure 17. Unbalanced Forces During the Tailslap Stage 40
Figure 18. Texas 10.8-Degree Single-Slope Bridge Rail [6] 49
Figure 19. Sequential Events from TTI Test No. 420020-3 [6] 50
Figure 20. Barrier Mesh Sizes 52
Figure 21. Tire and Vehicle Body Impacting Forces for Varying Barrier Mesh Sizes 53
Figure 22. Vehicle Climb and Roll Angle for Varying Barrier Mesh Sizes 54
Figure 23. Sequential Images for Baseline Texas Single-Slope Barrier 56
Figure 24. Maximum ZOI Positions for Low and High Tire-to-Barrier COFs 59
Figure 25. Vehicle Vertical Displacement 60
Figure 26. Vehicle Roll Angle for Varying Tire-to-Barrier Friction Coefficients 61
Figure 27. Deformed Silverado Tire 62
Figure 28. Vehicle Pitch Angle Measured from Local Coordinate Axes 63
Figure 29. Simulated Vehicle Pitch Angle 64
Figure 30. Vehicle Pitch Angle Measured from Instrument Mounting Panel 65
Figure 31. Vehicle Yaw Angle for Varying Tire-to-Barrier Friction Coefficients 67
Figure 32. Angular Data from Test No. 420020-3 [6] 68
Figure 33. Fender Protrusion Over the Barrier (Note: Fender is orange for distinction) 70
Figure 34. Fender Impact with a Rigid Pole [11] 71
Figure 35. Maximum ZOI Positions for Low and High Vehicle-to-Barrier COFs 74
Figure 36. Vehicle Vertical Displacement 75
Figure 37. Vehicle Roll Angle 76
Figure 38. Vehicle Yaw Angle 77
Figure 39. Vehicle Pitch Angle 78
Figure 40. Contact Forces Between the Vehicle Body and Barrier 79
Figure 41. Contact Forces Orientations 80
Figure 42. Elastic Barrier Deformation during Impact 85
Figure 43. Deformed Barrier Shapes for Each Elastic Barrier Simulation 86
Figure 44. Energy Absorbed by the Elastic Barrier 87

Figure 45. Vehicle Roll Angle Comparison for Elastic Barrier Impacts 88
Figure 46. Vehicle C.G. Vertical Motion Comparison for Elastic Barrier Impacts 89
Figure 47. Baseline Simulation Model Used to Determine ZOI 91
Figure 48. Simulated 9.1-degree Barrier Profiles 91
Figure 49. Baseline 9.1-degree Single-Slope Barrier Simulation C.G. Height Comparison 93
Figure 50. Contact Forces by Component 94
Figure 51. Total Vertical Force Between the Vehicle and Barrier 95
Figure 52. Vehicle Roll Toward the Barrier 96
Figure 53. Baseline 9.1-degree Single-Slope Barrier Simulation Vehicle Roll Angles ... 96
Figure 54. Baseline 9.1-degree Single-Slope Barrier Simulation Vehicle Yaw Angle 97
Figure 55. Baseline Simulation Vehicle Pitch Angles 98
Figure 56. Force Transmitted Through the Steering Link 99
Figure 57. Suspension Damage for the Model with Tire Deflation 99
Figure 58. Baseline Maximum ZOI Positions 100
Figure 59. Baseline 9.1-degree Single-Slope Barrier Simulation Tire Pressure 103
Figure 60. Maximum ZOI Positions for the Tire Deflation Model 104
Figure 61. Tire Deflation Simulation Vehicle C.G. Height 105
Figure 62. Tire Deflation Simulation Vehicle Roll Angle 105
Figure 63. Maximum ZOI Positions for the Full Suspension Failure Simulation 108
Figure 64. Maximum ZOI Positions for the Model with Lower Control Arm and Steering Link Failures 109
Figure 65. Maximum ZOI Positions for the Model with Lower Control Arm Failure ... 110
Figure 66. Suspension Damage for the Model with Full Suspension Failure 111
Figure 67. Working Width Measurements 115
Figure 68. Simulated Occupant Model 117
Figure 69. Bucket Seat Model 118
Figure 70. Seatbelt Model 119
Figure 71. Seat and Rigid Block Model 120
Figure 72. Seat, Rigid Block, and Simulated Occupant Model 122
Figure 73. Dummy Sliding Out of Seat 123
Figure 74. Seatbelt, Seat, and Rigid Block Model 124
Figure 75. Belt Deformation During Simulation 125
Figure 76. Seatbelt Stretch 126
Figure 77. Seat, Seatbelt, and Dummy Accelerated to the Left 127
Figure 78. Seat, Seatbelt, and Dummy when Accelerated to the Right 128
Figure 79. Dummy, Seat, Seatbelt, and Vehicle Simulation 130
Figure 80. Dummy Reaction in the Vehicle 131
Figure 81. Head Protrusion Out of the Vehicle 132
Figure 82. Door Deflection With and Without Dummy Occupants 133
Figure 83. Seatbelt Forces on the Dummy Occupant 135
Figure 84. Forces Between the Dummy Occupant and the Door 136
Figure 85. Vehicle Vertical Displacement 137
Figure 86. Vertical Force between the Vehicle and the Barrier 137
Figure 87. Vehicle Roll Angle 138
Figure 88. Vehicle Roll Angular Rates 139

List of Tables

Table 1. Barrier ZOI from the MwRSF Barrier Attachments Study [10] 15
Table 2. ZOI for TL-3 Concrete Barriers According to MASH [3] 16
Table 3. Suspension Damage for Full-Scale Crash Tests with 2270P Vehicles 28
Table 4. 32-in. (813-mm) Concrete Barriers Tested According to NCHRP Report No. 350 Test Designation 3-11 33
Table 5. Working Widths for Various Barrier Mesh Sizes of a 10.8-degree Single-Slope Barrier According to MASH Test Designation 3-11 52
Table 6. Computational Costs for Varying Barrier Mesh Sizes 55
Table 7. ZOI of Varying Tire Coefficients for the 10.8-degree Single-Slope Barrier 70
Table 8. Zone of Intrusion – Varied Vehicle Body-to-Barrier COF 82
Table 9. Elastic Barrier Study Summary 85
Table 10. Elastic Barrier Computation Time Comparison 90
Table 11. ZOI Comparison for the Baseline 9.1-degree Single-Slope Simulation Model 101
Table 12. ZOI Results for the Model with Tire Deflation 106
Table 13. ZOI Values for Tire Suspension Failure Models 112
Table 14. Zone of Intrusion of the Rigid Wisconsin 9.1-degree Single-Slope Barrier 113
Table 15. Working Width for the Rigid Wisconsin 9.1-degree Single-Slope Barrier 114
Table 16. ZOI and Working Width of the Rigid 9.1-degree Single-Slope Barrier 142

1 INTRODUCTION

1.1 Background

Roadside barriers are designed to prevent vehicles from impacting hazards located behind the barrier. Some roadways require the roadside barriers to be constructed immediately in front of a hazard (such as next to a bridge pier) or call for objects to be placed on top of a barrier (such as a luminaire pole mounted on a barrier). In these situations, an errant vehicle impacting the roadside barrier risks contacting the hazard located directly behind or on top of the barrier. For this reason, a measure called the zone of intrusion (ZOI) was developed. ZOI is defined as the maximum distance that the vehicle protrudes behind the top front corner of the barrier.

If a ZOI value is adequate, any hazard placed outside of the ZOI of a barrier will not pose additional risk to the occupant. Underestimating a ZOI value means that the occupant may be injured in the event of a severe impact. Overestimating a ZOI value may result in greater costs for state transportation departments in accommodating for roadside hazards.

In 2009, the *Manual for Assessing Safety Hardware* (MASH) was published by the American Association of State Highway Transportation Officials (AASHTO), and it detailed crash testing standards to be used in all full-scale crash tests [1]. MASH standards expanded on previous crash-testing requirements found in the National Cooperative Highway Research Program (NCHRP) Report No. 350 [2]. According to Test Level 3 (TL-3) conditions specified in MASH, a 5,000-lb (2,270-kg) pickup truck must be full-scale crash tested at 62 mph (100 km/h) and 25 degrees into a longitudinal barrier in order to verify that the roadside barrier is acceptable for placement along state

highways. These impact conditions represented one of the most severe impact cases observed on the roadway system. Thus, these crash testing conditions are used to determine the ZOI of a longitudinal barrier.

The Wisconsin State Department of Transportation (WDOT) wished to design and install a California 9.1-degree single-slope barrier along its roadways. To best understand the impact performance of this barrier, state transportation officials requested that the ZOI be estimated for the 9.1-degree single-slope barrier with barrier heights of 36 in. (914 mm), 42 in. (1,067 mm), and 56 in. (1,422 mm) using computer simulation.

Finite element simulations represent a cost-effective means of analyzing multiple impact scenarios compared to prohibitive full-scale crash testing. Due to the severity of concrete barrier impacts, a variety of vehicle behavior has been observed, including that (1) with no tire or suspension failure, (2) with tire deflation, (3) with suspension failure, and (4) with tire deflation and suspension failure. The maximum ZOI determined from these four impact scenarios would give an estimate of the maximum ZOI of each barrier system.

1.2 Project Objective

Zone of intrusion values were estimated for the Wisconsin 9.1-degree single-slope barrier at heights of 36, 42, and 56 in. (914, 1,067, and 1,422 mm). Impacts with tire deflation and various suspension failure scenarios were evaluated, and the maximum ZOI values were estimated from each simulation.

2 PROCEDURE

To complete this project, several steps were undertaken:

1. A literature review was conducted to review recent testing on concrete barriers.
2. The interaction between an impacting vehicle and a concrete barrier was extensively reviewed from full-scale crash testing results.
3. A simplified vehicle model was developed to establish phases of impact and understand which forces affect vehicle trajectory during each phase.
4. A series of simulations were conducted utilizing a Silverado truck model to compare impact behavior to results observed in full-scale tests. Parameter studies were performed to determine how friction and model changes affect the simulated ZOI.
5. Simulations were performed at severe conditions to evaluate the ZOI and working width for three heights of single-slope barrier using various suspension failure conditions, consisting of tire deflation and joint failures.
6. Conclusions were drawn pertaining to ZOI and working width. Future work was also recommended.

3 LITERATURE REVIEW

3.1 Introduction

Simulations are a cost-effective means of inspecting complicated dynamic events. However, improperly constrained or inaccurately defined simulations may generate unrealistic results. Because of this, researchers must make a strong effort to compare simulation results to full-scale testing and confirm that the results seen in the simulations are realistic.

Full-scale crash testing and research studies were reviewed to better understand the concrete barrier, the zone of intrusion, and the interaction between an errant vehicle and a rigid concrete barrier. Barriers were studied by shape, and comparisons were made between similar shapes.

3.2 Concrete Barrier Testing History

A literature review was conducted to review concrete barrier testing and ZOI studies [3]. Full-scale crash tests of permanent and restrained-motion concrete barriers were reviewed to determine the vehicle-to-barrier interaction during the crash sequence and to provide a basis to develop a simulation model. Different barrier types were reviewed and compared to determine the vehicle stability and protrusion for each barrier shape.

The New Jersey barrier, which was the first non-vertical concrete barrier to gain nationwide acceptance for its crashworthiness, was originally intended to be evaluated at impact angles lower than 15 degrees. However, for the past 20 years, all of the full-scale crash tests obtained during the literature review were conducted at impact angles of 20

degrees or more; furthermore, current testing utilizes 25 degree impacts for passenger vehicles.

The impact performance of shaped concrete barriers varies at different impact angles. At higher impact angles, the vehicle's front fender impacts the barrier first and begins to crush. At lower impact angles, the tire impacts the toe of the barrier first and begins climbing the barrier. Combined with frictional force effects, suspension compression characteristics, and full-body vehicle rotational motion, the behavior of low-angle impacts greatly diverges from higher-angle impacts, with significantly different effects on vehicle trajectory and vehicle damage. However, it is believed that the ZOI is greatest for higher-angle impacts. Thus, the lack of testing at different impact angles may not affect this study.

There are two types of commonly-installed single-slope barrier configurations. Texas developed a single-slope barrier with a slope of 10.8 degrees on its front face [4]. This barrier has been tested under both MASH and NCHRP Report no. 350 standards and has been determined to be acceptable in both cases [5-6]. California developed a single slope barrier with a slope of 9.1 degrees on its front face. The California State Transportation Department (Caltrans) tested this barrier extensively under NCHRP Report no. 350 standards but did not evaluate the barrier using MASH vehicles [7-9]. By comparing the test results on the 9.1-degree barrier to the 10.8-degree barrier, it was shown that, for 2000P vehicles impacting at 62 mph (100 km/h) and 25 degrees, the 9.1-degree barrier demonstrated improved stability and lower lateral accelerations, as well as lower vehicle roll angles. However, the 9.1-degree barrier showed higher filtered

longitudinal accelerations and was in contact with the barrier for longer than the 10.8-degree barrier.

3.3 ZOI Studies

In 2003, a report was published by the Midwest Roadside Safety Facility (MwRSF) discussing barrier attachments and their effect on impacting vehicles [10]. Researchers noted that breakaway and rigid attachments to barrier may penetrate into the occupant compartment or cause excessive vehicle accelerations. Both of these conditions are hazardous to the occupants, and cause the system to fail the full-scale crash criteria set forth in MASH and NCHRP Report No. 350. A few examples of hazards located within the zone of intrusion are shown in Figure 1.

Figure 1. Hazards Located Within the Zone of Intrusion

According to the barrier attachments report published by MwRSF, occupant safety depends on how much vehicle structure protrudes behind the top front corner of the barrier. Stiff, structural vehicle component impacts against vertical elements on top of or behind the barrier will cause greater risk to the occupants than impacts from weak vehicle components. It was up to the discretion of the researchers to determine which critical vehicle component was used to determine the ZOI during those tests. Often, the chosen ZOI utilized the corner of the vehicle's engine hood.

In 2008, MwRSF published a follow-up study to the barrier attachments research [11]. Three full-scale tests were conducted on a 32-in. (813-mm) tall, 10.8-degree single-slope concrete barrier, as shown in Figure 2. A luminaire pole was mounted on top of the barrier inside the ZOI. For the first test, a 17,605-lb (7,985-kg) single-unit truck (SUT) impacted the barrier system 55 ft (16.8 m) upstream of the centerline of the luminaire pole, shown in Figure 2a. The vehicle struck the pole, and the pole was dislodged. Researchers determined that the test was acceptable and that the impact with the luminaire pole did not cause significant risk to the occupants.

(a) ZOI-1

(b) ZOI-2

(c) ZOI-3

Figure 2. Zone of Intrusion Tests ZOI-1, ZOI-2, and ZOI-3 [11]

For the second test, a 4,430-lb (2,009-kg) pickup truck impacted the system 11 ft (3.4 m) upstream of the centerline of the luminaire pole. The corner of the vehicle hood briefly contacted the pole, and the vehicle was redirected away from the system. The test was determined to be acceptable, although the head ejection effects were not determined since no dummy was used in the full-scale crash test.

For the third test, a 17,637-lb (8,000-kg) SUT impacted the single-slope barrier 54 ft 6 in. (16.6 m) upstream of the centerline of the pole. The vehicle struck the pole, but it was not enough force to cause the pole to be dislodged, and no adverse effects were noted on the vehicle due to the impact with the pole.

MwRSF researchers also developed guidelines for head ejection criteria [12]. During an impact with a roadside barrier, researchers noticed that the occupant's head will occasionally protrude through the impact-side window, potentially impacting hazards outside of the vehicle. Thus, an envelope was created based on measured head protrusions of dummies during full-scale crash tests, as shown in Figure 3. For barriers to meet the head ejection criteria, no hazard may be placed inside the envelope.

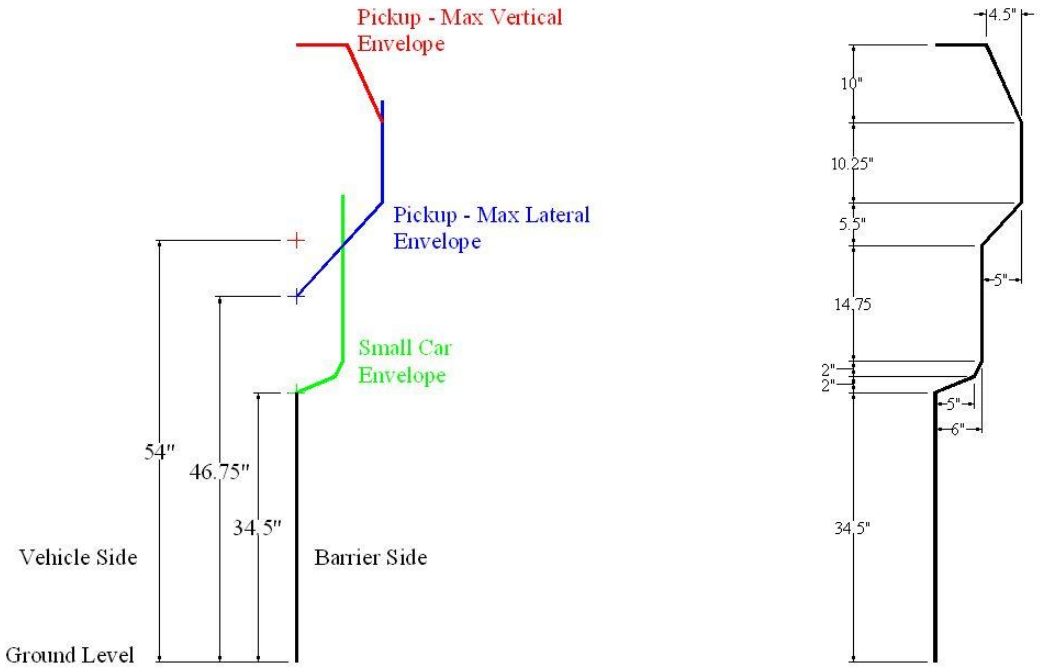

Figure 3. Head Ejection Envelope [12]

In 2011, the Texas A&M Transportation Institute (TTI) published a report detailing a study on placing objects inside the ZOI [13]. A rigid, non-breakaway sign was installed at a joint between two temporary concrete barriers. During the test, the front fender and door contacted the sign while the unrestrained temporary barriers deflected 4.3 ft (1.3 m). The maximum working width was 10.2 ft (3.1 m) with the deflection of the sign panel. During the test, the vehicle penetration behind the barrier and climb up the barrier was insignificant. It is unknown if a restrained barrier system with a similar sign configuration would have passed with similar results.

At the conclusion of the study, TTI researchers determined that it was possible to construct fixed, non-breakaway systems inside the ZOI of a barrier. However, each system must be evaluated independently with full-scale crash testing in order to be approved. No dummy was used in this full-scale crash test, and the setup may likely have

caused injury to an occupant if the occupant's head protruded out of the window during the crash.

Similar studies have had similar results. In 2007, MwRSF conducted a test on a concrete bridge pier protection system [14]. The barrier consisted of a 32-in. (813-mm) tall, vertical-faced permanent concrete barrier with bridge piers located 16¾ in. (425 mm) behind the front face of the barrier. As determined by overhead video analysis, the vehicle hood protruded 19.8 in. (503 mm) beyond the front face of the barrier and struck the bridge pier, as shown in Figure 4. This behavior did not negatively affect the test, and after some deformation of the vehicle hood, the vehicle continued to redirect downstream. The occupant safety was not compromised during the test. Once again, no dummy was used during this test, so it is unknown as to whether or not the system would have passed if a dummy was placed in the vehicle.

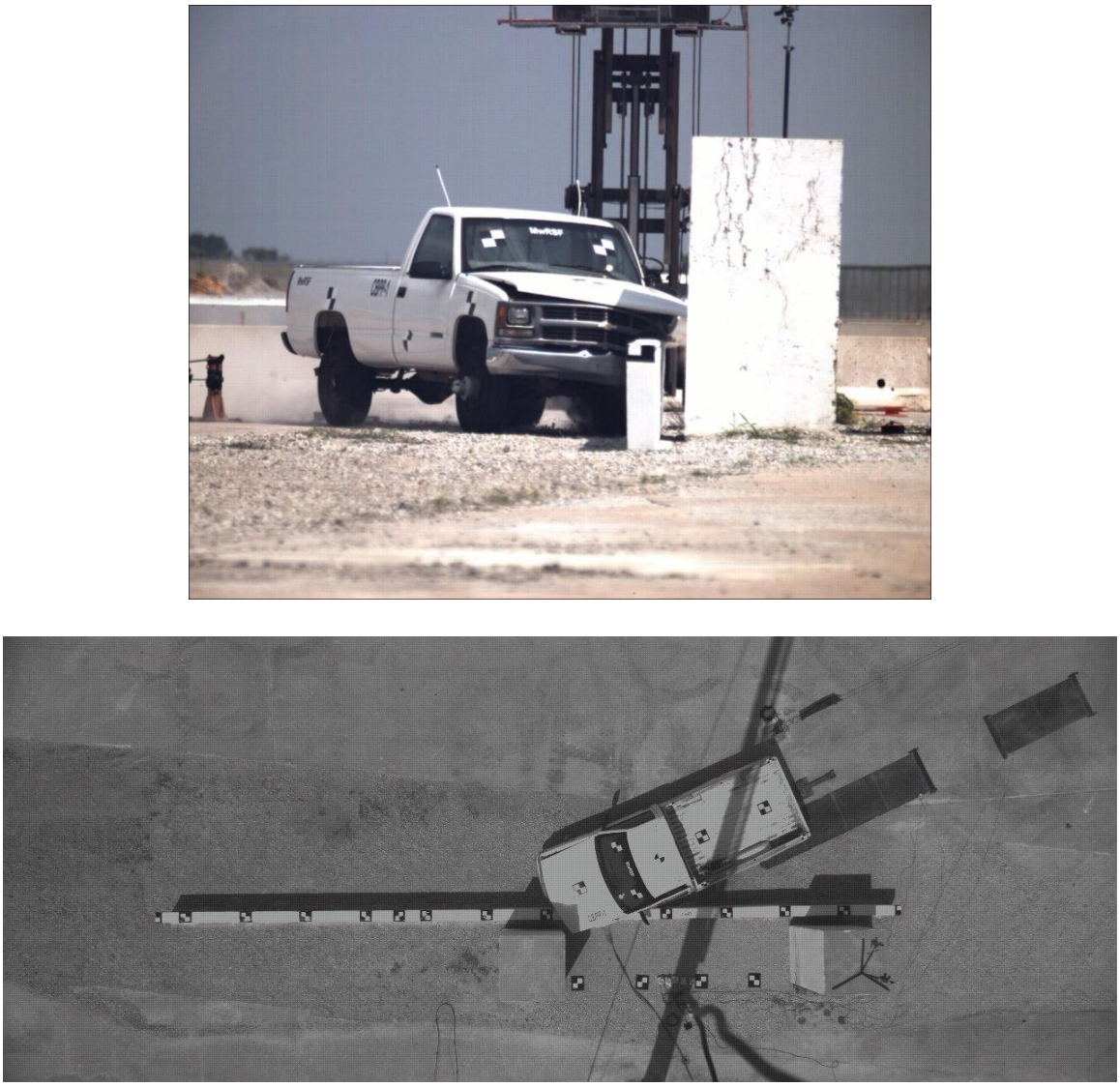

Figure 4. Impacting a Bridge Pier in the ZOI

The Florida State Department of Transportation wished to apply ZOI guidelines to its 40-in. (1,016-mm) tall, F-shape barrier according to TL-3 standards of NCHRP Report No. 350 [15]. The ZOI for the barrier impacted by a 2000P vehicle at 62 mph (100 km/h) and at an angle of 25 degrees (equivalent to the TL-3 standards of NCHRP Report No. 350) was predicted to be 5 inches. The ZOI estimate determined during this study was consistent between the various simulation conditions applied to the model. The

ZOI for the barrier impacted by a 2000P vehicle at 45 mph (72 km/h) and at an angle of 25 degrees (equivalent to the TL-2 standards of NCHRP Report No. 350) is predicted to be between 1.8 and 2.5 in. (46 and 64 mm). These numbers were the ZOI extremes determined by the different impact conditions, and the variations may be attributed to the quality of the model's mesh and to the system geometry.

During this study, it was determined that the front hood geometry will extend over the top of a 40-in. (1,016-mm) tall, F-shape concrete barrier during impact. Thus, some ZOI is inevitable at almost all speeds. However, the ZOI of the 40-in. (1,016-mm) tall barrier was restricted to overhang by the front corner of the hood and part of the fender. The limited amount of vehicle structure in the ZOI of the barrier may not cause problems during an impact event.

3.3.1 ZOI Values from NCHRP Report No. 350 Testing

MwRSF researchers presented a table of ZOI values for various TL-3, TL-4, and TL-5 rigid bridge rails at different barrier heights [10]. The ZOI values were estimated by reviewing video footage from full-scale crash tests performed according to NCHRP Report No. 350. Most concrete barrier shapes have been evaluated for TL-3 standards at a height of 32-in. (813-mm). These ZOI values are shown in Table 1. The references to the tests used to determine the ZOI were provided in Reference 10.

Table 1. Barrier ZOI from the MwRSF Barrier Attachments Study [10]

Barrier Shape	ZOI in. (mm)
10.8-degree Single-Slope	12 (305)
F-Shape	8 (203)
New Jersey	18 (457)
Vertical Face	15 (381)

3.3.2 ZOI Values from MASH Testing

ZOI values were obtained for the same barriers tested according to MASH standards [3]. Impacts with rigid barrier systems caused higher protrusions than impacts with temporary barrier systems. However, there were only two tests conducted on rigid concrete barrier systems utilizing MASH testing criteria. It was determined that the full-scale vehicle trajectory was very similar for impacts with restricted-motion temporary barrier systems and for impacts with rigid barrier systems. MASH ZOI data were collected from restrained-motion and rigid concrete barrier systems, as shown in Table 2. The references to each test used to determine the ZOI were provided in Reference 3.

Table 2. ZOI for TL-3 Concrete Barriers According to MASH [3]

Barrier Shape	ZOI in. (mm)	Additional Notes
F-Shape	9 (229)	This was a temporary barrier system that saw significant deflection, despite one end of the barrier being fixed. Actual ZOI may be larger.
New Jersey	15 (381)	
Texas 10.8-degree Single-Slope	10 (254)	This test was conducted on a 36-in. (914-mm) tall barrier
Vertical Face	9 (229)	Temporary barrier system saw mild deflection (less than 5 in. [127 mm])
California 9.1-degree Single-Slope		Not yet tested to MASH standards

The ZOI for these barriers may be misleading. ZOI data shown in Table 2 were measured from tests utilizing Dodge Ram pickup trucks, which have a front-end geometry that is very dissimilar to other pickup trucks on the roadway today. For the Dodge Ram pickup truck, the hood is rigidly attached to the grill of the vehicle, and the hood is trapezoidal in shape, as shown in Figure 5. Some vehicles, such as the Chevy Silverado, have rectangular hoods which are more likely to protrude over a barrier upon impact, as shown in Figure 6. Thus, the actual ZOI may be larger than the ones shown in Table 2.

Figure 5. Dodge Ram Hood and Fender Geometry

Figure 6. Chevy Silverado Hood and Fender Geometry

3.4 In-Depth Suspension Behavior Analysis

The behavior of the vehicle suspension during the full-scale impact affects the overall trajectory and damage to the vehicle. Unfortunately, test footage of the tire and suspension damage is difficult to analyze because the impact occurs relatively quickly, the tire is in the shadows during the impact, and the views are rarely zoomed-in to see the impact closely. To gain insight into the interaction between the vehicle tire and the barrier, the damage to a vehicle suspension was documented and compared to high-speed video.

3.4.1.1 Damage Documentation

Test No. PCMB-1 was conducted on a 32-in. (812-mm) tall,h F-shape barrier using a Dodge Ram Quad Cab 1500 vehicle [16]. Damage to the impacting wheel consisted of rim deformation, scuffing, contact marks, and tire tearing. The ball connection attaching the wheel to the lower control arm was bent forward, as shown in Figure 7. There was no fracture of any of the ball joints on the wheel assembly, and it appeared that the suspension failed when the ball joints pulled out of their respective sockets.

Scraping occurred along the rim at the bottom of the ball joint bolts for the lower control arm and steering link. The rim was dented in ¾ in. (19 mm) at the impact location of the tire with the barrier, and scuffs were found at the dent in the rim. This damage was consistent with the rim contacting the concrete barrier.

The impacting tire was deflated, and a 7¾-in. by 3¼-in. (197-mm by 83-mm) section of tire was missing from the sidewall, as shown in Figure 8. The missing tire section occurred close to the dent in the rim, signifying that the tire section and the rim damage may have occurred simultaneously.

Suspension damage was noted on the impact-side of the vehicle. The lower control arm was bent downward ¼ in. (6 mm) at the rear near the connection to the shock. The plastic ball joint socket on the lower control arm was fractured, as shown in Figure 9. Also, the metal ring around the outside of the plastic ball joint deformed. This damage was consistent with the ball being pulled out of the joint while applying a large longitudinal force on the lower control arm ball joint. No damage was noted on the lower control arm at the connection between the lower control arm and the vehicle frame.

Cylindrical metal sleeves connecting the lower control arm to the vehicle frame were not damaged, but the lower control arm shifted to the rear on these sleeves shown in Figure 10. Also, the bolt holding the rear metal sleeve in place was bent. The connection slip and the damage to the lower control arm and joint are consistent with large longitudinal forces acting on the component as the wheel impacted the barrier. The forces would have caused the connections to slide out of place and would have bent the rear arm of the lower control arm.

The rubber bump stop did not experience any permanent deformation, although the rubber showed signs of contact at the tip of the cone, as shown in Figure 11. After closely inspecting the bump stop, the extent of the deflection of the bump stop was indeterminable. However, bending and deformation of the steel ring around the bump stop were found. This damage was consistent with the bump stop being fully compressed and the metal ring around the bump stop contacting the lower control arm.

The upper control arm was bent toward the rear of the vehicle, as shown in Figure 11. Damage to the upper control arm was consistent with a large lateral and longitudinal load being applied to the component. Also, the rear connecting bolt for the upper control arm was bent slightly. However, no other damage was noted on the upper control arm.

The link connecting the roll bar to the lower control arm was bent, as shown in Figure 12. Also, the impact side of the roll bar was twisted and bent downward. The roll bar shifted ⅛ in. (3 mm) toward the impacting side, as determined from the scrape marks seen around the link connecting the roll bar to the frame of the vehicle, shown at the bottom of Figure 12.

Figure 7. Inside of Wheel Damage, Test No. PCMB-1

Figure 8. Outside of Wheel Damage, Test No. PCMB-1

Figure 9. Lower Control Arm Damage, Test No. PCMB-1

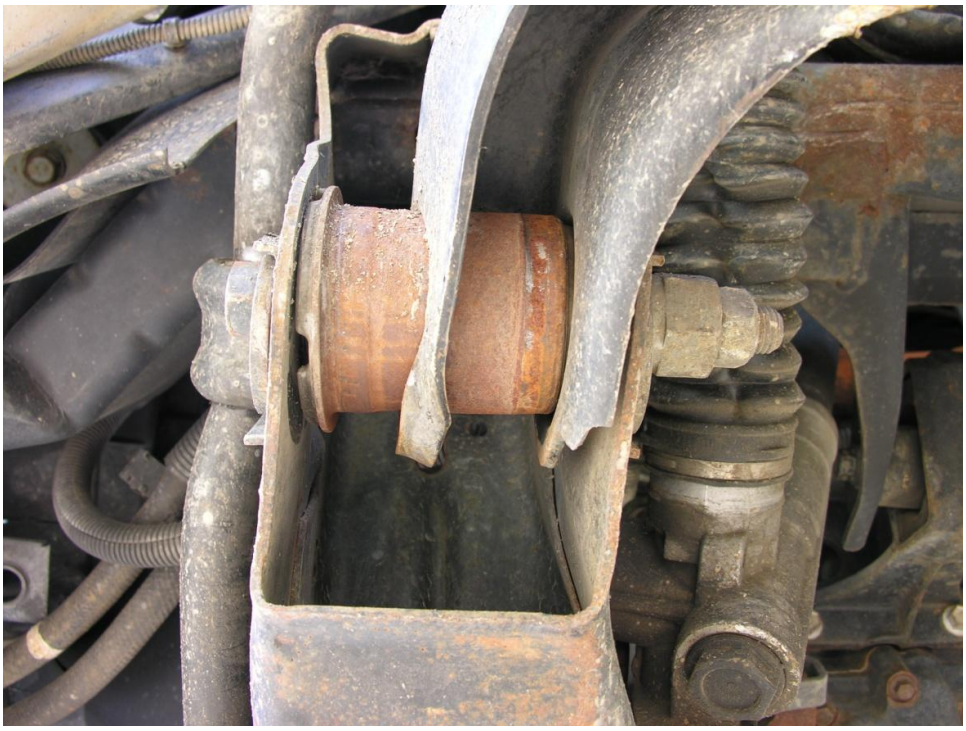

Front Connection Slip (View looking toward longitudinal centerline of vehicle)

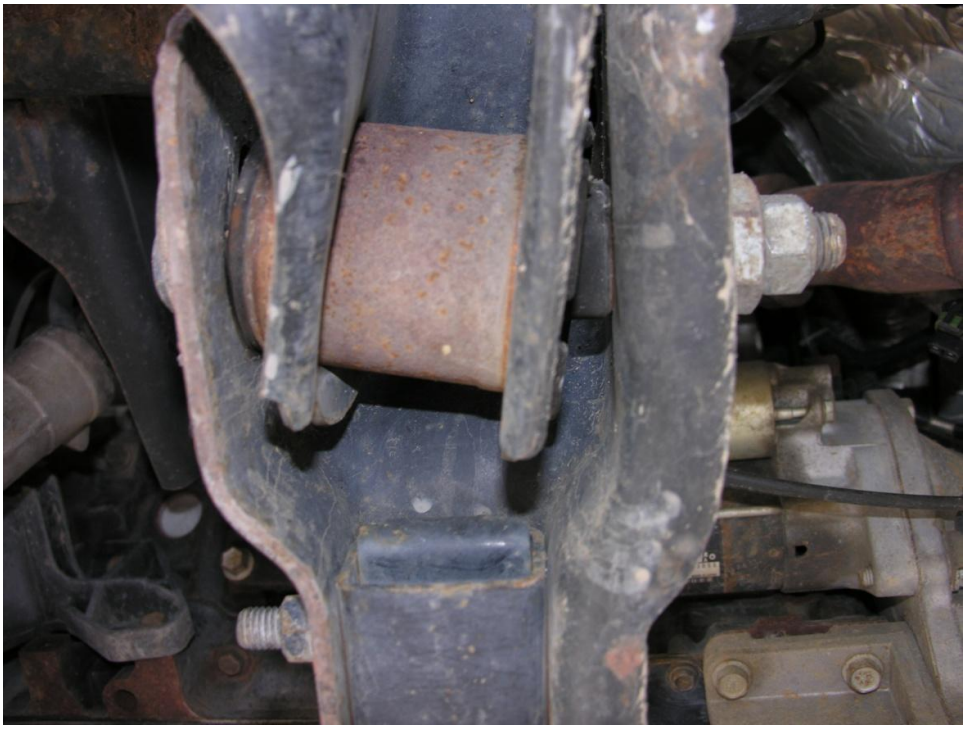

Rear Connection Slip (View looking toward longitudinal centerline of vehicle)

Figure 10. Lower Control Arm Connection Slip, Test No. PCMB-1

Figure 11. Bump Stop and Upper Control Arm Damage, Test No. PCMB-1

Figure 12. Roll Bar and Connecting Pin Damage, Test No. PCMB-1

3.4.1.2 Damage Interpretation

The impact damage to the wheel was reviewed in conjunction with the full-scale crash test footage to determine how the damage occurred. At impact, the tire tread contacted and mounted the barrier toe, climbing up the lower sloped face of the barrier. As the tire climbed, the base of the tire compressed and the wheel vertical deflection was insignificant compared to the tire deformation. Based on the vertical deflection of the center of the rim, the suspension did not significantly deflect. As the tire compressed, the sidewalls bulged out around the impact location. The tire sidewall was pinched between the wheel rim and the concrete barrier, causing the rubber to rupture, the tire to deflate, and a piece of the sidewall to disengage. Contact occurred between the rim and the concrete barrier, which dented and scraped the edge of the rim.

The wheel continued to climb up the barrier, reaching the top of the lower slope and impacting the upper slope. The vehicle suspension compressed significantly as the wheel began to climb up the upper slope of the F-shape barrier. Also, the bottom of the wheel was pushed inward, showing that the lower control arm was deforming. When the top of the tire impacted the upper slope, the top of the wheel deflected toward the center of the vehicle, showing that the upper control arm was deforming. Very soon after this, the steering link was seen removed from the vehicle. The non-impact tire was noted to be traveling straight forward, while the impact tire turned away from the barrier sharply. Based on the reaction of the other tire, it appears that the steering link did not transmit significant force, and likely disengaged from the vehicle quickly after impact. As the vehicle deflected upward, the tire was squeezed between the vehicle and the upper slope.

Friction between the tire and the barrier pulled the tire downward, and disengaged the wheel from the three ball joints holding it to the suspension.

3.4.1.3 Damage Summary

Tire and suspension damage incurred in test no. PCMB-1 is not indicative of the damage noted in other concrete barrier tests with the 2270P vehicle, and may not be reproducible with a similar system, impact conditions, and vehicle. While the events of test no. PCMB-1 differed from other tests, there were many similarities between the tire and suspension damage noted in this test and the damage documented in other full-scale crash tests with concrete barriers. First of all, large rearward forces are transmitted by the wheel through the joints and into the vehicle. This force may cause damage in both the upper and lower control arms. Second, the rubber bump stop fully compressed. Third, the roll bar did not act as a rigid object, but rather proved itself to be dynamic and plastic in concrete barrier impacts. Lastly, the tire deformed greatly as it impacted the barrier, and the tire sidewall bulged out at the impact location. The rim contacted the barrier and pinched the tire, causing the tire to rupture at the impact point between the wheel and the sloped barrier.

3.5 Suspension Damage for 2270P Pickup Trucks

In order to understand the tire-barrier interaction during a full-scale test, suspension damage was documented from many full-scale concrete barrier crash tests utilizing 2270P pickup trucks. Unfortunately, due to the limited amount of testing that has been conducted with 2270P vehicles on concrete barrier systems, only testing results utilizing a Dodge Ram 1500 Quad Cab pickup truck were available. Pictures and documentation from each test were reviewed. Damage to each vehicle suspension is

noted in Table 3. Since suspension damage documentation was not available from other sources, only suspension damage from MwRSF tests were reviewed.

Table 3. Suspension Damage for Full-Scale Crash Tests with 2270P Vehicles

Ref. No.	Test Name	Barrier Profile	Configuration	Suspension Damage
17	NYTCB-1	New Jersey	Stiffened	Lower control arm knuckle fractured off Tire deflated
17	NYTCB-2	New Jersey	Unrestrained	Lower control arm knuckle fractured Tire deflated
17	NYTCB-3	New Jersey	Stiffened	Upper control arm ball joint separated from the socket Lower control arm knuckle fractured Tire deflated
18	KSFRP-1	Vertical	Pinned	Upper control arm knuckle fractured Tire deflated
19	TCBT-1	F-Shape	Unrestrained	Lower control arm knuckle fractured Upper control arm ball joint separated from the socket Tire deflated
19	TCBT-2	F-Shape	Unrestrained	Lower control arm knuckle fractured Upper control arm ball joint separated from the socket Tire deflated
20	NYTCB-4	New Jersey	Pinned	Lower control arm knuckle fractured Upper control arm ball joint separated from the socket Tire deflated
21	NYTCB-5	New Jersey	Pinned	Lower control arm knuckle fractured Upper control arm ball joint separated from the socket Tire deflated
22	TTCB-1	F-Shape	Unrestrained	Lower control arm knuckle fractured Upper control arm ball joint separated from the socket Tire deflated

Three different barrier configurations were reviewed: stiffened, pinned, and unrestrained. Stiffened systems utilized an attachment between joints that reduced joint deflection. Pinned systems were connected to the pavement using rods or bolts,

preventing lateral movement of the barrier. Unrestrained barrier systems had pinned end barriers, but were not pinned or stiffened in the middle barriers.

Suspension damage was similar for every observed impact between 2270P vehicles and F-shape and New Jersey barriers. In each of these tests, three behaviors occurred. First, the steering link disengaged from the vehicle. Second, the impacting tire deflated. Third, the lower control arm fractured. The initial impact between the bottom of the tire and the toe of the barrier is believed to have caused these three behaviors.

Soon after impact between the bottom of the tire and the toe of the barrier, the steering link would separate from the vehicle, sometimes even becoming a projectile. In several tests, the steering link was not damaged despite disengaging from the vehicle. From this, it was evident that the steering link joint was not constructed to transmit large forces. Instead, the steering link joints are created such that they separate before the component experiences large-scale plastic deformation.

Tire deflation was observed during each concrete barrier test as well. In strong-post guardrail tests, tires may snag on posts, and the flange of the post may puncture the tire. However, in concrete barrier systems, there are no sharp edges or objects to deflate the tire. Thus, a more careful analysis of the tire failure is necessary to better understand what actions cause the tire to deflate.

Lower control arm failure occurred in each observed impact with F-shape and New Jersey concrete barriers. For sloped concrete barriers, the force is transmitted to the tire through the bottom part of the tire, which places excessive loads on the rim at the bottom. This load exceeds the strength of the lower control arm at the joint, causing shear fracture at that location.

One vertical barrier test (test no. KSFRP-1) encountered severe upper control arm damage. For vertical barriers, the top of the tire is pinned between the vehicle and the barrier, and as the vehicle rolls toward the barrier, the tire is pressed into the vehicle, thus increasing the load on the upper control arm. Consequently, there was little damage to the lower control arm or steering link.

Only one test was conducted utilizing a 2270P vehicle on a single-slope concrete barrier [6]. Documentation on this test did not provide information on the damage to the vehicle suspension. Thus, to determine the suspension damage to a vehicle impacting a single-slope barrier, the geometry of the barrier was taken into account. Similar to F-shape and New Jersey concrete barriers, impacting tires would first contact a single-slope barrier at the bottom, and the initial force would be transmitted through the lower control arm. Thus, it is expected that 2270P vehicle suspension damage would be similar to the suspension damage seen in the F-shape and New Jersey concrete barrier tests.

3.5.1 Free-Standing, Restricted-Motion, and Permanent Barrier Systems

During an impact sequence, an errant vehicle is successfully redirected after all of the vehicle's lateral energy has been absorbed or transferred to other sources. With metal-beam guardrail systems, a lot of energy is absorbed through fracture, elastic deformation, and plastic deformation of the guardrail and posts. Concrete barriers do not have these methods of absorbing energy.

For segmented, free-standing, unstiffened concrete barrier systems, the lateral impact energy of the vehicle is absorbed through several processes. Some energy is transferred to the concrete barrier system in the form of kinetic energy as the barriers deflect backward, and energy is dissipated through friction as the barrier slides on the

ground. Some energy is transmitted into the vehicle roll, pitch, and yaw motions. Some energy is transferred into vertical potential energy of the vehicle as it climbs up the barrier. Some energy is transferred into the elastic and plastic deformation of the vehicle suspension and fender. An unrestrained temporary concrete barrier system is shown in Figure 13a.

Compared to segmented, free-standing concrete barriers, permanent concrete barrier systems (such as continuous barriers or systems with the base of the barrier buried into the ground) absorb a small amount of the lateral energy during the impact sequence. Energy absorbed by the concrete barrier occurs in the form of compression and deformation of the concrete. Elastic and plastic deformation of the vehicle sheet metal and suspension components absorb part of the lateral energy. Some energy is transmitted into vehicle climb up the barrier and roll, pitch, and yaw motions. A permanent concrete barrier is shown in Figure 13b.

Some temporary concrete barrier systems are restrained from having excessive deflections, allowing temporary barriers to be used in places where permanent barriers are necessary. These barriers absorb energy in methods similar to a permanent concrete barrier system, as well as deformation of pins and loops as well as fracture of the barrier near the joints. A restrained-motion temporary barrier is shown in Figure 13c.

a) Free-Standing Temporary Concrete Barriers

b) Permanent Concrete Barrier

c) Temporary Concrete Barriers with Restrained Movement

Figure 13. Types of Concrete Barrier Systems

Because of the energy dissipated by friction and the motion of the barriers, analysis of a moving free-standing barrier system would be more complicated than the analysis of a rigid, fixed barrier system and the restrained-movement barrier system. The barrier motion associated with free-standing barriers is difficult to reproduce between tests, complicating test comparisons. However, many more tests have been performed on free-standing temporary barrier systems than permanent, fixed barrier systems. Some of the tests conducted using temporary barriers utilized some form of barrier restraints. A summary of NCHRP Report No. 350 test designation 3-11 full-scale crash tests into 32-in. (813-mm) tall fixed-barrier and limited-deflection temporary barriers are shown in Table 4. It should be noted that several tests were not taken into consideration because they were geometrically dissimilar to any barrier shape. MASH tests were not included in this count because of the low test count.

Table 4. 32-in. (813-mm) Concrete Barriers Tested According to NCHRP Report No. 350 Test Designation 3-11

	New Jersey	**F-Shape**	**California Single-Slope**	**Vertical**	**Texas Single-Slope**
Number of fixed-barrier tests	2	1	1	1	2
Number of restrained-barrier tests	10	6	2*	1	3

* One of these tests was conducted using a steel barrier attached to a concrete base using threaded rods.

From the tests in the database, there were 12 full-scale crash tests conducted on a 32-in. (813-mm) tall fixed concrete barrier using a 2000P pickup truck, but only six

permanent concrete barrier impacts had normal, non-textured front faces. Also, all of the tests conducted on the 32-in. (813-mm) tall, 9.1-degree single-slope barrier were either aesthetic, textured barriers or a metal barrier. Thus, these tests may not correlate well with each other, let alone with standard non-textured barriers, because the higher friction between that surface and the vehicle may produce drastically different results.

Most full-scale crash tests on concrete barriers utilizing the 2000P vehicle have been run on the New Jersey barrier system. However, the New Jersey barrier tended to show instability when impacted at 25 degrees and 62.1 mph (100 km/h), and the test results from the New Jersey barrier were inconsistent. The New Jersey barrier has been shown to have a higher rollover rate compared to the F-shape, single-slope barrier, and vertical barrier due to the fact that the vehicle fleet and testing methods shifted since the barrier was first instituted.

The F-shape barrier showed fairly consistent impact results, and was chosen to model for that reason. As stated earlier, F-shape restricted-motion concrete barrier systems were reviewed to ensure a broad sample of tests were used to verify the simulation model. Barriers were restricted using drop pins, tie-down straps, or by burying the base in the ground.

3.5.2 Vehicle Climb Up the Barrier

The post-impact vehicle trajectory was compared for different F-shape barrier tests, as shown in Figure 14. The sequential images from the fixed barrier full-scale crash test were not included here because of their poor quality [**Error! Reference source not ound.**]. Also, one test was not included in this analysis because the barrier joints failed

during the test (which is unrepresentative of the barrier motion during a fixed, permanent barrier test).

a. Test no. FTB-1 at Parallel [A-4]

b. Test no. FTB-1 at Ground Impact [A-4]

c. Test no. KTB-1 at Parallel [23]

d. Test no. KTB-1 at Ground Impact [23]

e. Test no FTB-2 at Parallel [A-4]

f. Test no. FTB-2 at Ground Impact [A-4]

g. Test no. 405160-3-2a at Parallel [24]

h. Test no. 405160-3-2a at Ground Impact [24]

Figure 14. Post-Impact Trajectories of F-Shape Concrete Barrier Crash Tests

a. Contact Marks from Test No. FTB-1

b. Contact Marks from Test No. FTB-2

c. Contact Marks from Test No. KTB-1

Figure 15. Impacting Tire Ride-Up for Different Full-Scale Crash Tests

In all of the reviewed tests, the vehicle trajectory was very similar. The impacting tire of the vehicle contacted the barrier and proceeded to climb up the barrier. The vehicle rolled away from the barrier and pitched upward. Vehicle redirection occurred very soon after impact. The rear tires impacted the toe of the barrier and began to climb up the barrier as well. The rear tires became airborne and the vehicle pitched downward while still rolling away from the barrier. As the vehicle came in contact with the ground again, it rolled toward the barrier and pitched upward to reach equilibrium. The similarity of vehicle motion between these tests was significant, and showed that test results for the 32-in. (803-mm) barrier are fairly repeatable.

All of the full-scale tests showed significant tire climb on the upper sloped face of the barrier, with several of the tires climbing the entire barrier face. The impacting tire ride-up on the barrier for several tests is shown in Figure 15. As the tire climbed the barrier, tire scrubbing occurred, and the rim scraped along the barrier as well. This caused gouging and contact marks to be present along the front face of the barrier for much of the length of contact.

Comparing the fixed, permanent barrier test to the limited-deflection temporary barrier tests provided some interesting insight. Compared to the permanent concrete barrier system, the four limited-deflection temporary barrier tests experienced much higher roll and pitch angular deflections during the impact, and showed much lower roll and pitch angular deflections. In the limited-deflection temporary barrier system, the impacting tire climbed higher on the barrier, and the vertical deflection of the center of gravity of the vehicle was larger.

4 SIMPLIFIED VEHICLE MODEL

After reviewing several crash tests, it was noticed that there were many similarities in vehicle trajectories between tests conducted on similar barrier shapes. Analysis on the forces and moments acting on the vehicle allows for comparison between simulation results and full-scale results, as well as qualitatively assess forces.

4.1 Simplified Model Setup

For most permanent or restrained-motion barrier systems, the forces acting on the side of the vehicle largely occur at six locations – the front impacting corner, the rear impacting corner, and through the four tires. In hopes of better analyzing the system and making recommendations to improve the vehicle impact performance, a simplified model of the vehicle was developed, as shown in Figures 16 and 17. The simplified model uses gross motion analysis of the vehicle, which is represented as a rectangular prism acting in three dimensions. Forces act at the corners of the prism, representing the unbalanced forces acting on the vehicle fender and bumper and the tire. The model was developed based on an impact with a sloped barrier (F-shape, New Jersey, or single-slope barrier).

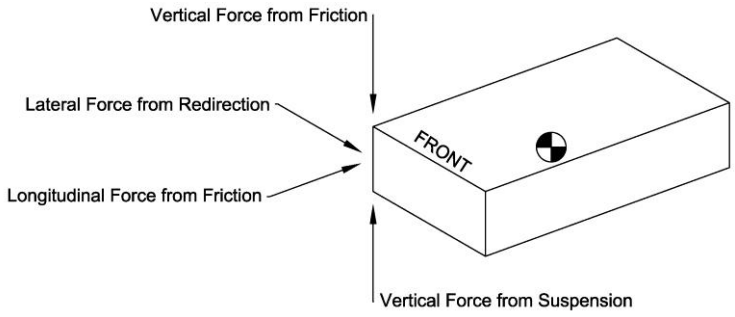

Figure 16. Unbalanced Forces During the Initial Impact Stage

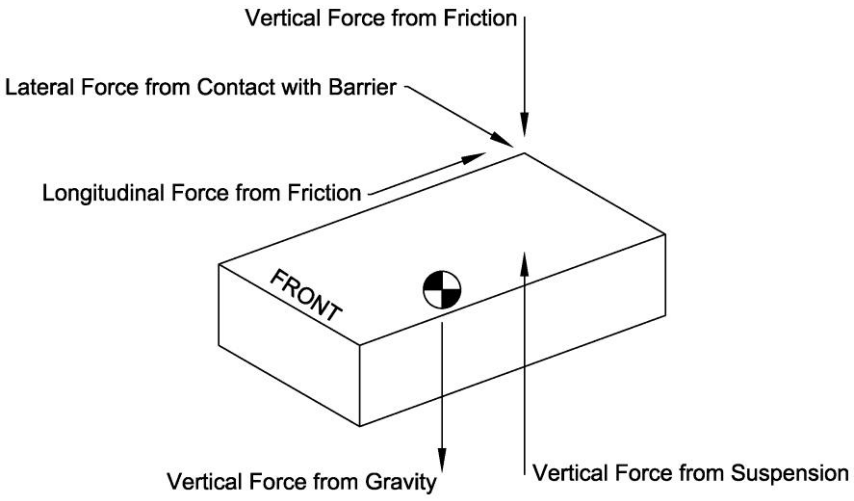

Figure 17. Unbalanced Forces During the Tailslap Stage

4.2 Simplified Model Stages

The interaction between the vehicle and the barrier occurs in many different stages, with different forces being applied and removed. For this analysis, a sloped concrete barrier was analyzed, and it was assumed that the vehicle tire rides up the barrier, such as what was seen in impacts with the F-shape, New Jersey, Texas 10.8-degree single-slope, and the California 9.1-degree single-slope barriers.

4.3 Pre-Contact Stage

4.3.1 Force List

Initially, prior to contact, the vehicle is assumed to be traveling straight forward without any vehicle rotation. This is the impact condition presented in all current MASH testing. A vertical force on the vehicle is applied at each tire location. Because the vehicle is tracking and not turning, the frictional force between the vehicle tires and the ground was considered to be negligible. In this pre-impact stage, there are no unbalanced forces.

Full-scale crash testing with roadside appurtenances has only utilized tracking, straight-forward impacts with concrete barriers. While non-tracking impacts have been determined to be more severe than tracking impacts [25], there are no MASH or NCHRP Report No. 350 full-scale crash test results to review.

4.4 Impact Stage

4.4.1 Force List

The impact forces initiate in different orders depending on the impact angle, which has a large effect on the vehicle post-impact trajectory. In this stage, both front tires become airborne. An unbalanced vertical force is applied through the impacting tire into the sprung mass of the vehicle. As the vehicle strikes the sloped concrete barrier, the vehicle body is in direct contact with the barrier, causing a lateral redirecting force normal to the barrier face and a longitudinal frictional force acting parallel to the barrier surface. As the vehicle climbs the barrier, the contact between the fender and the barrier produces a downward force on the front of the vehicle, counteracting the vehicle pitching motion. The unbalanced forces acting on the vehicle during the impact stage are shown in Figure 16.

Vertical acceleration of the vehicle was directly related to the unbalanced vertical force from the suspension on the vehicle. Excessive vertical accelerations showed large vehicle climb up the barrier combined with stiff suspension. The frictional force between the barrier and the vehicle tire and fender minimize the vertical suspension force on the sprung mass. Lateral acceleration of the vehicle was related to both lateral force on the tire and lateral force from redirection. However, a review of full-scale crash testing on low-angle impacts showed that the lateral component of the force on the tire does not

provide significant lateral force on the vehicle sprung mass. Longitudinal acceleration was a combination of the longitudinal frictional force on the vehicle body and on the impacting tire.

Various factors affect each force. Tire-to-barrier friction, barrier material, and shock stiffness are each independent factors affecting the suspension force on the vehicle sprung mass. Similarly, the frictional force between the vehicle and the barrier is dependent on the fender material, barrier material, shape, and surface treatments. To theoretically develop these forces would take a significant effort, and the constitutive model developed for each force would vary based on the vehicle.

4.4.2 Moments Caused by Impact Stage Forces

During the impact stage, the vehicle encounters roll, pitch, and yaw angular accelerations. Every reviewed test utilizing 2000P or 2270P trucks showed that the front end of the vehicle pitched upward and yawed away from the barrier during this stage. Most of the truck impacts caused the vehicle to roll away from the barrier, especially in New Jersey barriers.

Three of the unbalanced forces contribute to the vehicle roll motion. The vehicle roll motion is heavily influenced by the vertical force on the vehicle from the suspension, which acts about the longitudinal axis and causes the vehicle to roll away from the barrier. The higher the tire climbs on the barrier, the larger the vertical force on the vehicle body as the suspension compresses more. The lateral redirecting force acting on the tire acts about the longitudinal axis of the vehicle to oppose the vehicle roll away from the barrier. The downward force due to friction from the vehicle sheet metal and tire scrubbing against the barrier causes the vehicle to roll toward the barrier. Depending on

the structural design of the front fender of the vehicle, the lateral force on the fender from the impact with the barrier may impart a moment towards or away from the barrier.

Yaw rate is affected by the lateral redirective force applied to the front fender of the vehicle. The lateral force applies a moment to the vehicle about the vertical axis to cause the vehicle to yaw away from the barrier. Longitudinal frictional forces apply a moment about the vertical axis. This moment opposes the vehicle yaw away from the barrier. Yaw motion is also resisted by the contact between the non-impacting tires and the ground.

Pitch rate is affected by the vertical suspension force. The moment arm between the vehicle center of gravity and the point of application of the suspension force is significantly larger than the moment arms to any of the other forces. The suspension force acts about the lateral axis of the vehicle to cause the vehicle to pitch upward. Longitudinal friction forces between the barrier and the impacting tire and fender do cause a moment affecting the vehicle pitch. Friction forces from the tire imparts a moment opposing the upward pitch, while the friction forces from the fender may impart a moment supporting or opposing the upward pitch, depending on the structural layout of the fender. The rear tires apply vertical forces to the vehicle which act about the lateral axis of the vehicle to oppose the upward pitch motion.

4.5 Tailslap Stage

4.5.1 Force List

The vertical force transmitted through the impacting tire gradually decreases to zero, and the front of the vehicle loses contact with the face of the barrier. At this time, the vehicle yaw rate away from the barrier is significant, which causes the rear of the

vehicle to impact into the barrier face, which is referred to as the tailslap. During the tailslap, the rear tire mounts the sloped barrier surface, compressing the suspension and applying a vertical force to the sprung mass. A large lateral force is transmitted through the rear fender of the vehicle, and both of the rear tires leave the ground. The vehicle exits the barrier airborne. The diagram of the unbalanced forces during the Tailslap stage is shown in Figure 17.

The lateral force in this stage is due to the force normal to the barrier from the tailslap of the rear of the vehicle. In tests conducted on an aesthetic version of the California 9.1-degree single-slope barrier, the tailslap was very small, and the side of the vehicle was in contact with the barrier at the same time as the rear of the vehicle [26]. However, during these tests, the barrier face was a high-friction stone surface. The high-friction surface reduced the vehicle yaw rate, which minimized the tailslap. Thus, for most barriers, the tailslap would be expected to be much higher.

The unbalanced vertical force on the vehicle during the tailslap stage is caused by the rear vehicle suspension as the rear tire climbs the barrier. Frictional force between the barrier and the rear fender and tire opposed the suspension force. Unbalanced longitudinal force was the result of friction between the barrier and the rear tire and fender.

4.5.2 Moments Caused by Tailslap Stage Forces

The vertical force from the suspension on the vehicle sprung mass acts about the longitudinal axis of the vehicle to cause the vehicle to roll away from the barrier. The lateral force on the rear fender may cause the vehicle to roll away from the barrier if the

fender is located above the center of gravity. Vertical frictional forces between the vehicle and the barrier opposed the roll away from the barrier.

Yaw motion is affected by the lateral tailslap force on the rear fender of the vehicle, which acts about the vertical axis to cause the vehicle yaw rate away from the barrier to decrease. While uncommon, this force may be enough to cause the front of the vehicle to yaw towards the barrier. Often, this force causes the vehicle to exit the barrier with little to no yaw rate. Longitudinal frictional forces between the vehicle and the barrier also assist in decreasing the yaw rate.

Pitch motion is affected by the vertical force acting through the suspension about the lateral axis of the vehicle. This causes the front of the vehicle to pitch downward. The vertical friction forces between the vehicle and the barrier oppose the downward pitch. Longitudinal frictional forces may oppose or support the pitch motion, but the effect of these forces on the pitch motion is very small.

4.6 Airborne Stage

The vehicle exits the barrier airborne, and with only gravity acting on the vehicle, and the rotational and translation motion of the vehicle continue as it falls back to the ground.

4.7 Ground Contact Stage

Depending on the orientation of the vehicle c.g. in relation to the vehicle contact point, the vehicle will either roll over or will recover to a stable position. The reaction at this stage is dependent on the vehicle motion through the airborne trajectory stage. During this stage, only the ground imparts a force on the vehicle through either the

vehicle tires or through the side of the vehicle, if rollover has occurred, and the vehicle comes to rest.

5 SIMULATIONS OF THE 2270P SILVERADO INTO THE 10.8-DEGREE SINGLE-SLOPE BARRIER

5.1 Introduction

When developing simulations, it is best to verify simulation data by comparing it to full-scale crash testing results because it allows for model improvements to be implemented in order to create a more realistic, more accurate model. This includes parameter analysis to determine whether varying parameters increases the accuracy of the model. Full-scale crash testing has not been conducted on the 9.1-degree single-slope barrier, but full-scale crash tests have been conducted on the 10.8-degree single-slope barrier.

5.2 Section Objective

A 2270P Silverado was modeled impacting a Texas 10.8-degree concrete barrier system according to existing full-scale crash test details. Parameter studies on the friction, suspension stiffness, barrier mesh size, and barrier material were conducted to develop a baseline model for the ZOI study.

5.3 Model Development Considerations

Three considerations needed to be accounted when attempting to develop a model of a 2270P vehicle impacting a single-slope concrete barrier system:

1. At the time of this research, there was no readily-available model of the Silverado impacting a concrete barrier system. Thus, the contact definitions, barrier material model, barrier mesh density, and the timestep had to be optimized to improve the simulation.

2. No tests had been conducted on the California single-slope barrier according to MASH, and only one test was conducted on the Texas 10.8-degree single-slope barrier [6]. In test no. 420020-3, a 2005 Dodge Ram Quad Cab pickup truck impacted a 36-in. (914-mm) tall permanent Texas 9.1-degree single-slope concrete barrier on a pan-formed deck. Without having been tested with a Silverado, there is no guarantee that the model would compare to the results of this test.
3. Only one test has been performed utilizing the Silverado. Test no. 476460-1-4 utilized a 2007 Silverado impacting a 32-in. (813-mm) tall New Jersey concrete barrier system [27]. Without having been tested against a single-slope barrier, there is no comparison for how the Silverado behaves during impact with the barrier.

With limited data available for the full-scale Silverado impact, it was decided that the simulation would be conducted using the barrier and impact conditions according to test no. 420020-3, which was conducted on a Texas 10.8-degree single-slope barrier. The simulation results for the 10.8-degree single-slope barrier would not be identical to impact results for the 9.1-degree single-slope barrier, although the vehicle-barrier interaction would be similar.

5.4 Test No. 420020-3 Details

The concrete barrier constructed for test no. 420020-3 consisted of a 36-in. (914-mm) tall, permanent, single-slope half-section bridge rail, as shown in Figure 18. In the full-scale test, the barrier was impacted by a 5,036-lb (2,284-kg) 2005 Dodge Ram 1500 pickup truck [6]. The impacting tire climbed the barrier immediately, and the vehicle

began to pitch upward. Despite the tire climb on the barrier, the vehicle rolled toward the barrier as the vehicle became airborne. The vehicle continued to roll toward the barrier until it contacted the ground. Sequential photographs from the full-scale crash test are shown in Figure 19.

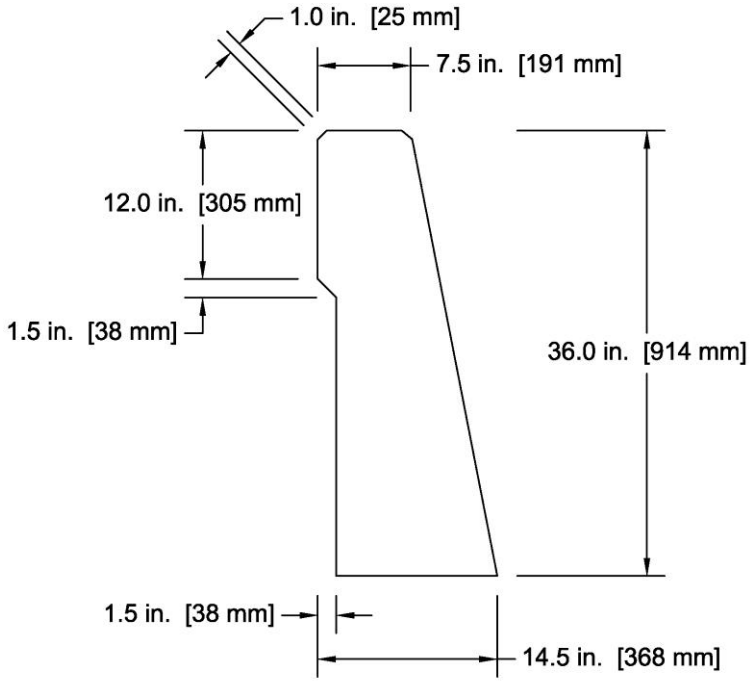

Figure 18. Texas 10.8-Degree Single-Slope Bridge Rail [6]


0.000 sec


0.089 sec


0.175 sec


0.263 sec


0.352 sec


0.440 sec


0.526 sec


0.615 sec

Figure 19. Sequential Events from TTI Test No. 420020-3 [6]

Following the full-scale crash test, some minor damage was noted on the barrier, including scraping and gouging. As for the vehicle, the front and rear impacting wheels were disengaged from the vehicle. Damage occurred to both the upper and lower ball joints. The windshield sustained minor cracking, and there was damage to the fender, bumper, and vehicle side panels.

5.5 Mesh Size

The barrier model was developed based on material, section, and mass characteristics of previous concrete barrier simulations [15]. The barrier dimensions were taken from the full-scale test barrier.

In finite-element simulations, the mesh size often affects the forces between objects, which can be shown by simple simulations of differently-meshed objects. Smaller meshes tend to produce softer impacts with lower peak forces. Because of the mesh density's effect on the transmitted forces, the mesh density needed to be determined through testing. Three things were considered during these tests – the maximum ZOI, the amount of time required to run the simulation, and the comparison of the test data to the actual test.

The barrier was meshed using 1.57-in. (40-mm), 0.79-in. (20-mm), and 0.39-in. (10-mm) mesh squares. The barrier was modeled using rigid shell elements. The barrier meshes are shown in Figure 20. The simulations were each run for at least 200 ms, capturing the maximum protrusions.

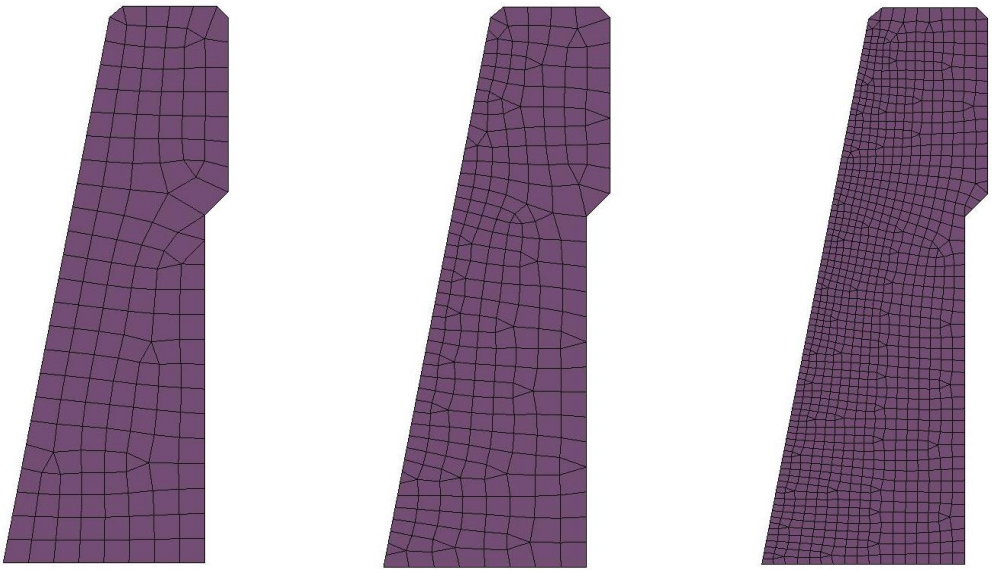

Figure 20. Barrier Mesh Sizes

Working width values for the various barrier mesh sizes are shown in Table 5. The working width point for all three simulations was the front corner of the left-front fender located above the headlight assembly. In each simulation, this corner detached from the vehicle and extended behind the barrier. The effect was not as significant with the 0.39-in. (10-mm) barrier mesh size, which had the lowest working width value because the fender corner did not extend as far behind the barrier.

Table 5. Working Widths for Various Barrier Mesh Sizes of a 10.8-degree Single-Slope Barrier According to MASH Test Designation 3-11

Mesh Size in. [mm]	**Working Width in. [mm]**	**Zone of Intrusion in. [mm]**
1.57 [40]	13.5 [343]	6.5 [165]
0.79 [20]	14.7 [374]	7.7 [196]
0.39 [10]	12.8 [325]	5.8 [147]

Tire and vehicle body impact forces were measured and plotted for the simulation runs, as shown in Figure 21. The smallest mesh produced the softest impact with the lowest peak force values. The largest mesh showed the highest peak lateral forces as the vehicle impacted the barrier. There was a significant difference in the impact forces exerted by the 0.79-in. (20-mm) and 1.57-in. (40-mm) mesh sizes, while the medium and small mesh sizes had similar force values

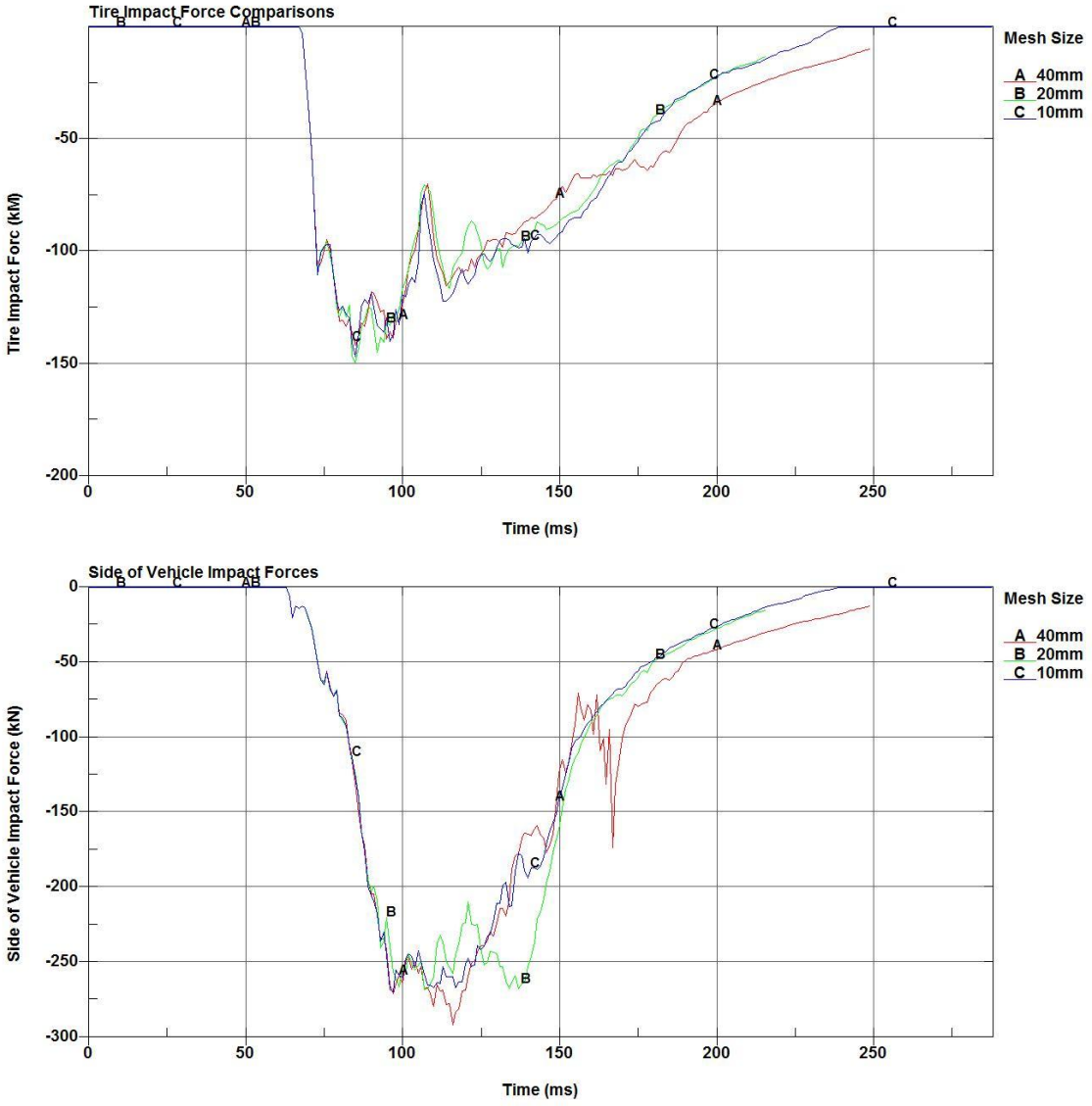

Figure 21. Tire and Vehicle Body Impacting Forces for Varying Barrier Mesh Sizes

Vehicle vertical climb and roll angles for each barrier mesh size are shown in Figure 22. The larger barrier mesh produced the lowest vehicle climb. However, the larger barrier mesh produced the largest peak roll angle values, although the roll angle decreased to zero after these initial peaks, and the vehicle began to roll away from impact. All of these factors are results of the stiffer impact resulting from the larger mesh. The 0.79-in. (20-mm) and 0.39-in. (10-mm) mesh sizes produced similar results, although the smaller mesh showed higher vehicle roll at the end of the simulation.

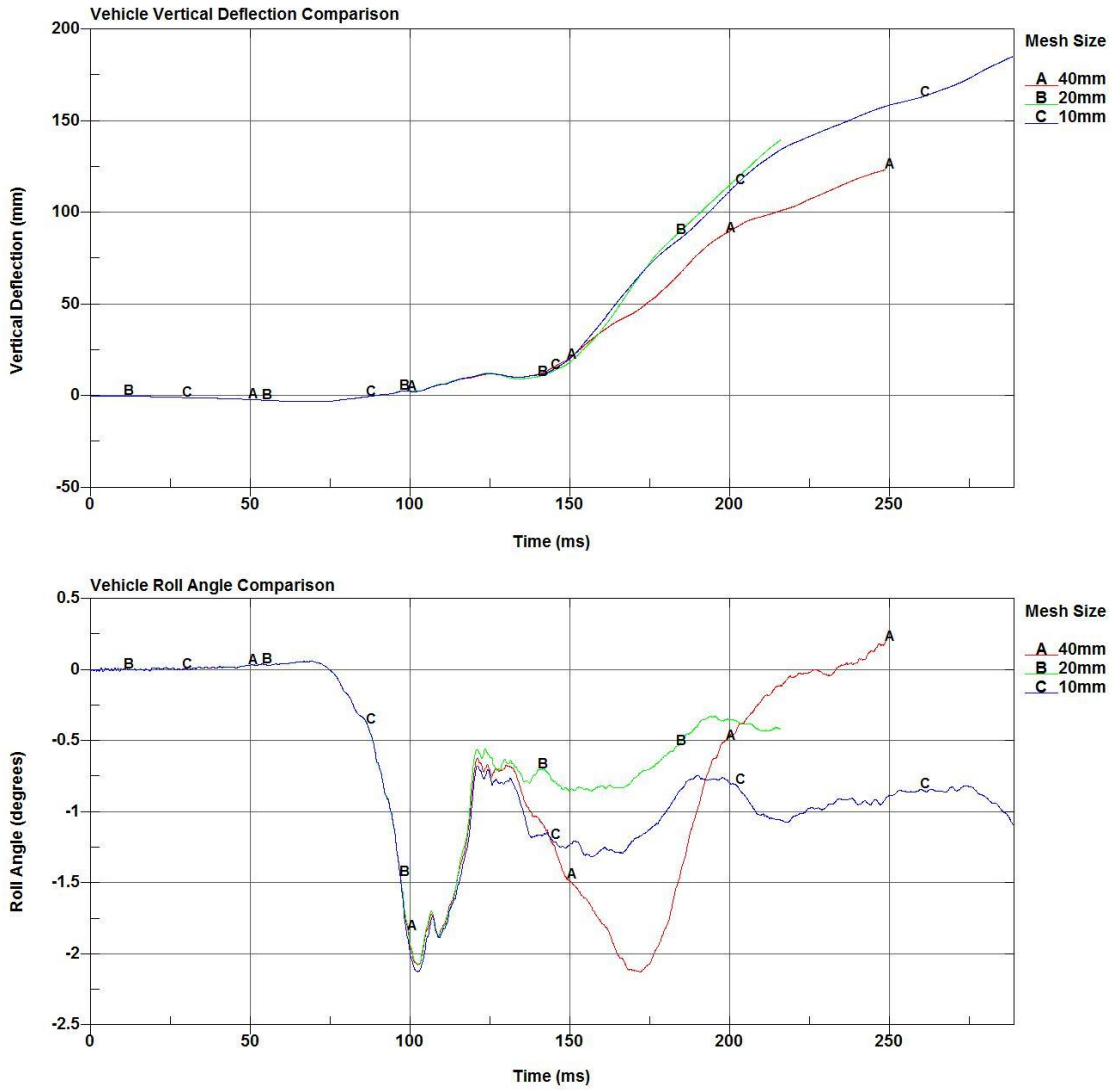

Figure 22. Vehicle Climb and Roll Angle for Varying Barrier Mesh Sizes

The difference between the 0.79-in. (20-mm) and 0.39-in. (10-mm) mesh size simulation results was relatively small. However, the smaller mesh size came at a computing cost. To compare computational costs, 200 ms of simulation were run using 16 processors, and the results are shown in Table 6. The 1.57-in. (40-mm) and 0.79-in. (20-mm) barrier meshes showed nearly identical simulation times, while the 0.39-in. (10-mm) barrier mesh showed a 23.5% increase in computation time. Based on the computation cost and the ZOI values, the 0.79-in. (20-mm) barrier mesh size was used for all further simulation models.

Table 6. Computational Costs for Varying Barrier Mesh Sizes

Barrier Mesh Size in. (mm)	Time to Simulate 200 ms (hours minutes seconds)
1.57 [40]	11h 28m 57s
0.79 [20]	11h 6m 10s
0.39 [10]	14h 30m 23s

5.6 Comparison to Full-Scale Test Results

Sequential images from the small-mesh baseline simulation with the 2270P pickup truck impacting the Texas single-slope concrete median barrier are shown in Figure 23. The overall vehicle crush, impacting tire motion, and vehicle trajectory were very consistent with the full-scale test results, shown in Figure 19.

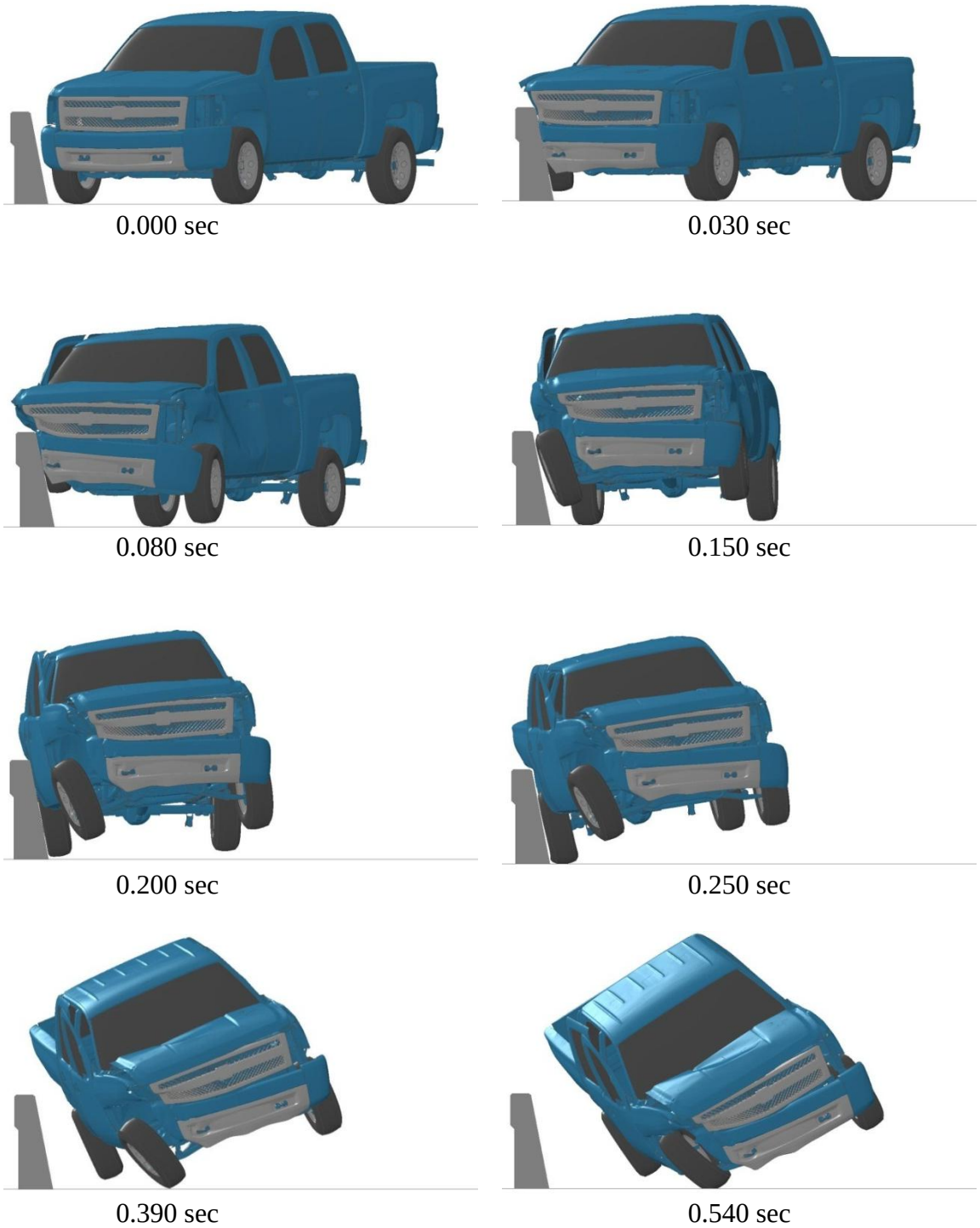

Figure 23. Sequential Images for Baseline Texas Single-Slope Barrier

Several differences were noted between the full-scale test and the simulation. The biggest difference was the height of the tire climb on the barrier. Using the photographs from the report, it was estimated that the height of the tire climb in the full-scale crash test was 9 in. (229 mm), while the height of the tire climb in the simulation was 13 in. (331 mm). Similar to what was discovered with the C2500 model, the disparity between the two values could be caused by the suspension stiffness. As the vehicle rolls toward the barrier after impact, the impacting tire climbs the barrier and rolls up the front face. The tire vertical motion is restricted by two forces: (1) the friction force between the tire and the barrier as the tire is scrubbed against the barrier, and (2) the suspension force transmitted to the vehicle.

From the full-scale test, the zone of intrusion was measured as 10 in. (254 mm), while in the simulation the zone of intrusion was measured to be 9.5 in. (241.3 mm).

5.7 Parameter Studies

Several parameter studies were conducted using a 2270P vehicle model. For these parameter studies, the interaction between the vehicle and the barrier was analyzed. Several parameters are pertinent to the impact performance: (1) the friction between the vehicle sheet metal and the barrier; (2) the friction between the vehicle tire and the barrier; (3) the stiffness of the suspension; (4) quarter panel crush stiffness; (5) the joint strengths and failure times; and (6) the vehicle dimensions, mass properties, and inertias. Many of these parameters were determined from physical testing and material specifications given for the modeled vehicle parts.

The vehicle mass and inertial properties of the 2270P Silverado model matched an actual Silverado pickup truck fairly well [28]. The quarter panel crush stiffness is the

product of several components and constraints, and is very complicated to review as a whole, and thus was not investigated as a part of this project.

It was decided that the suspension stiffness, the joint failure strengths and times, the tire-to-barrier friction coefficient, and the sheetmetal-to-barrier friction coefficient would be investigated. Also, several parameters specific to finite-element analysis were investigated, including the material definition type and the joint failure methods.

5.8 Tire-to-Barrier Friction Coefficient

From previous simulations using the C2500 vehicle model, the coefficient of friction between the barrier and the vehicle sheet metal, tire sidewalls, and tire tread was varied between 0.05, 0.3, and 0.6. Results from real-world friction studies have shown that the coefficient of friction between the vehicle tire and the barrier was significantly higher. However, in finite element modeling, accurate friction values are extremely mesh dependent and almost always lower than actual values in order to achieve desired results [29]. Thus, the friction coefficient had to be evaluated for its effect on the vehicle impact performance to better understand the interaction between the vehicle and the barrier.

The tire-to-barrier coefficient of friction is affected by many factors. Formation factors such as concrete composition and concrete casting method may greatly affect the coefficient of friction. Also, environmental factors such as ice and rain may affect the friction as well.

The small-mesh barrier was used to construct the next set of simulations. The coefficient of friction between the tire and the barrier was varied between 0.15 and 0.45. Vehicle positions at the maximum ZOI during the impact and tailslap phases were

reviewed, and the vehicle positions from the models using coefficients of friction (COFs) of 0.15 and 0.45 are shown in Figure 24.

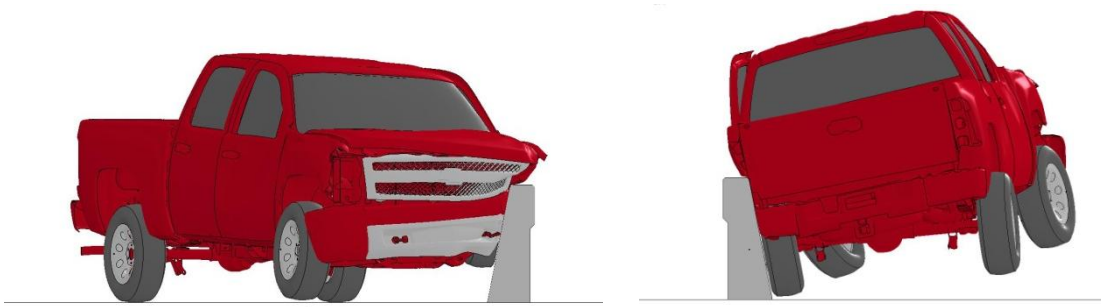

COF = 0.15

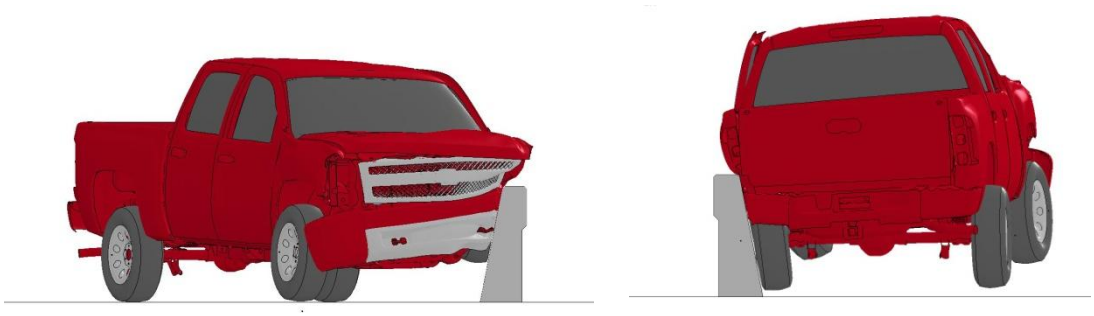

COF = 0.45

Figure 24. Maximum ZOI Positions for Low and High Tire-to-Barrier COFs

For these simulations, impact with the barrier occurred at approximately 60 ms, the rear of the vehicle impacted the barrier at approximately 240 ms, and the vehicle exited the barrier at approximately 330 ms. The impacting tire contacted the ground again at 450 ms.

5.8.1 Vehicle Vertical Displacement

The vehicle vertical displacement is shown in Figure 25. The vertical displacement here is due to the tire climbing up the barrier. Two factors affect how high the vehicle is vertically displaced: (1) the suspension stiffness, and (2) the height of the tire climb. Since the suspension stiffness is independent of the friction between the tire

and the barrier, the tire climb is the major factor contributing to the disparity in the vertical displacement of the vehicle.

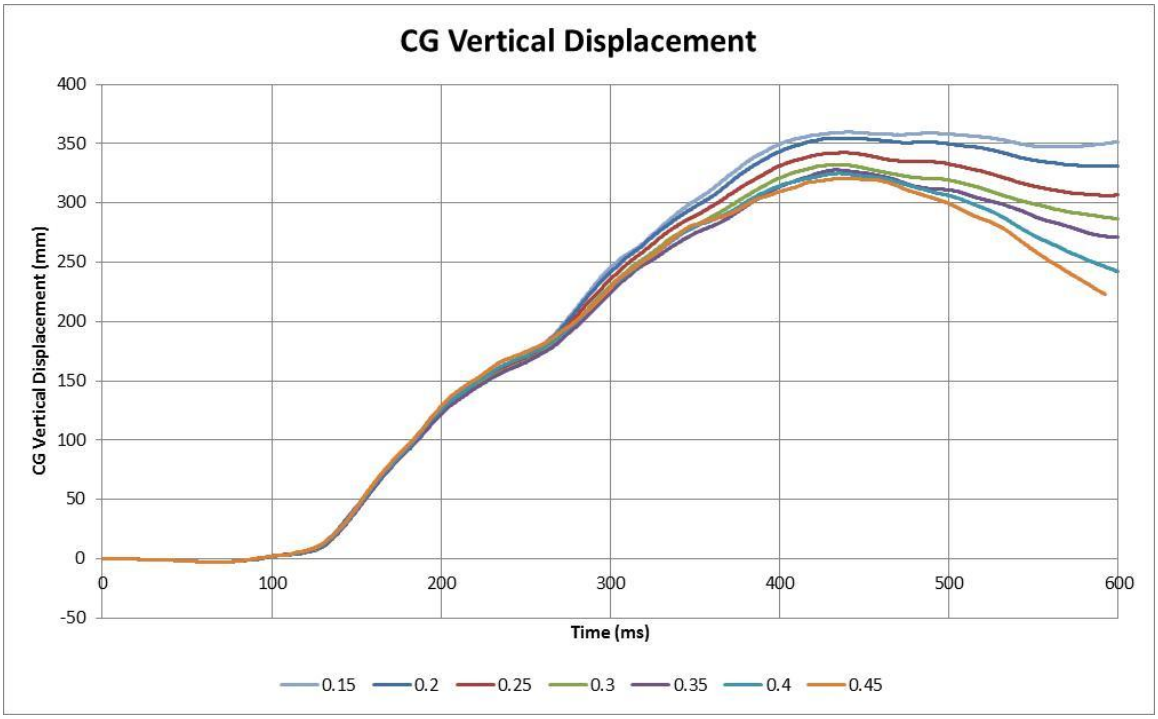

Figure 25. Vehicle Vertical Displacement

From Figure 25, the test run that had the highest vehicle vertical displacement was the run that had the lowest coefficient of friction. The highest coefficient of friction resulted in the lowest vehicle vertical climb. This indicates that the friction between the tire and the barrier resists vertical motion; likely, the vertical force occurred because the vehicle crushes the tire between the lower control arm and the barrier, then the tire is slid up the barrier. This produces the black tire marks that are commonly seen on the front faces of barriers. This also implies that the natural ride-up of the tire rolling up onto the barrier is not as significant as the tire being crushed against the barrier.

5.8.2 Roll Angle

The roll angles for the different runs were measured and are shown in Figure 26. The roll angle is initially affected by two different factors: (1) the lateral redirecting force exerted on the tire by the barrier and (2) the vertical force exerted by the suspension. The deformed tire from the Silverado impact is shown in Figure 27. Assuming that these results are realistic, the simulations imply that decreased barrier friction causes an increased roll risk.

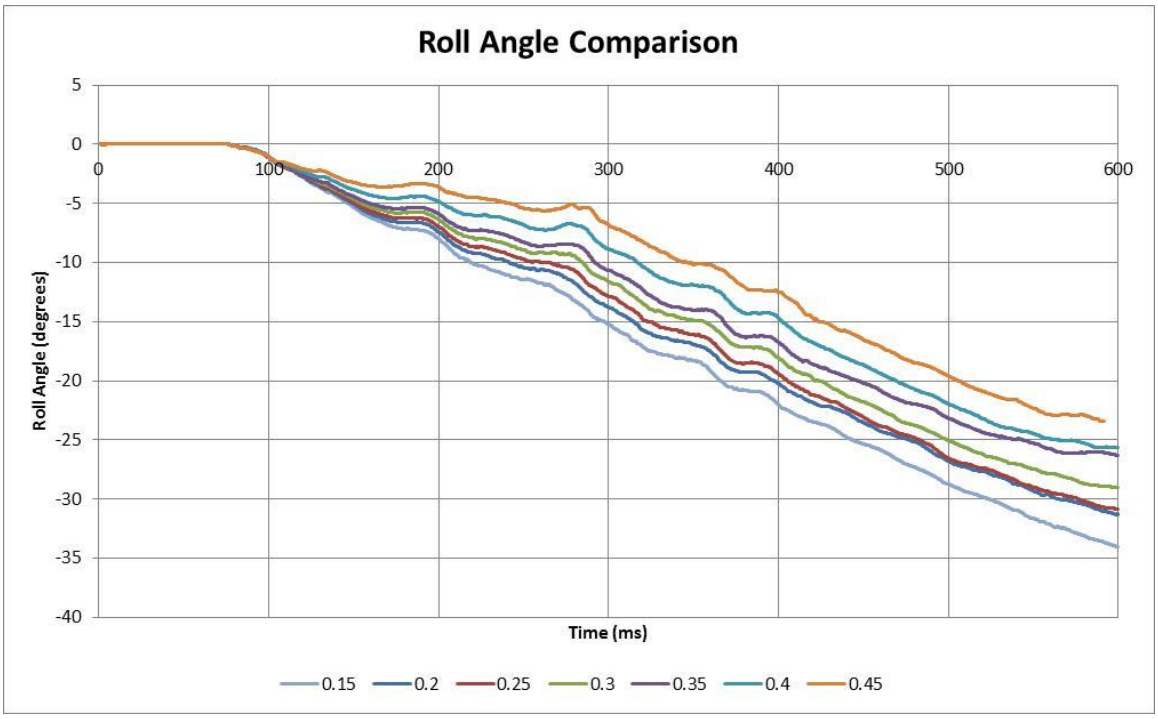

Figure 26. Vehicle Roll Angle for Varying Tire-to-Barrier Friction Coefficients

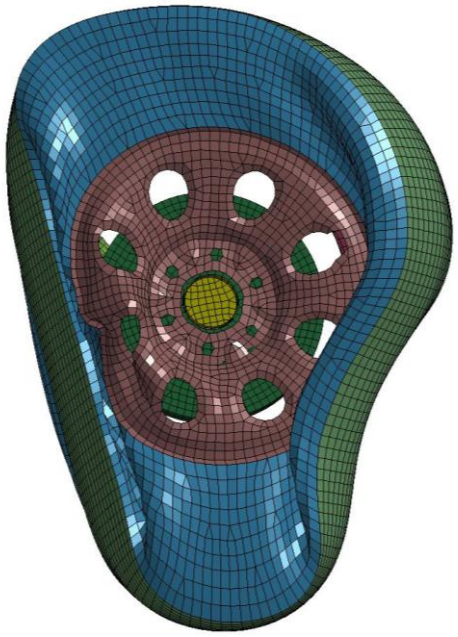

Figure 27. Deformed Silverado Tire

5.8.3 Pitch Angle and Analysis

The forces contributing to the pitch angle of the vehicle immediately after impact are the vertical forces acting upward on the suspension and the vertical friction forces acting downward on the tire as the vehicle climbs the barrier and the tire is scrubbed against the barrier. The roll, pitch, and yaw angles were measured using the local coordinate axes set established in the Silverado model at the vehicle c.g. The pitch angles as measured from the local coordinate axes are compared in Figure 28.

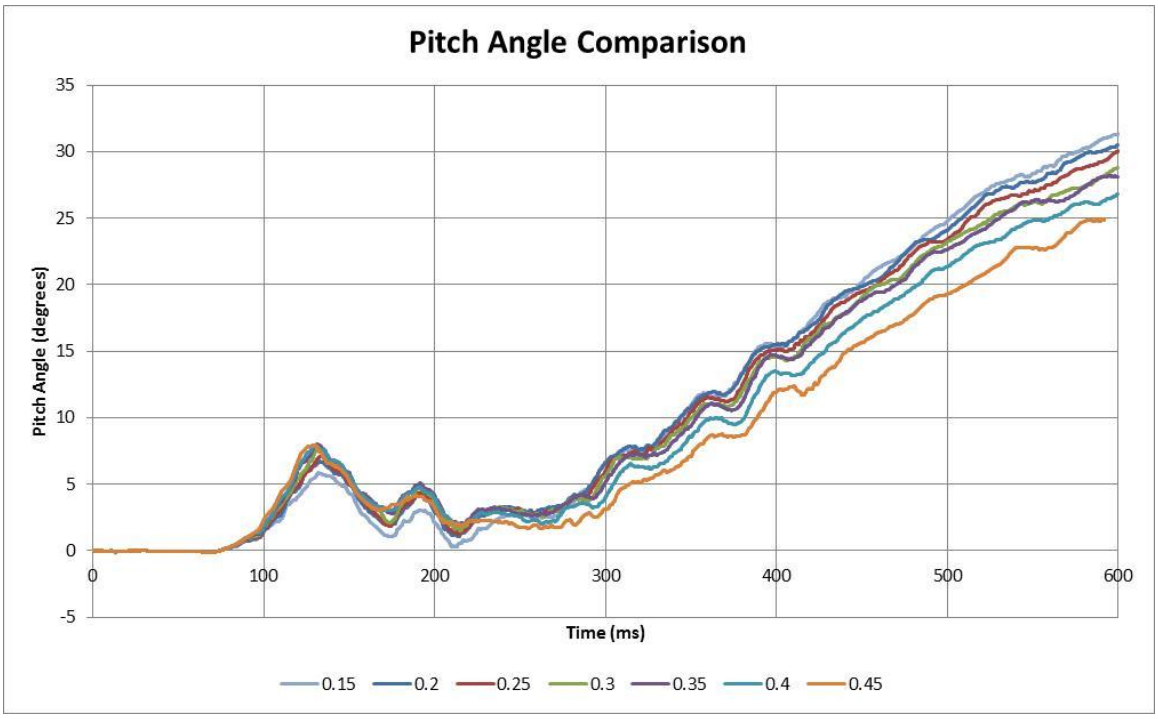

Figure 28. Vehicle Pitch Angle Measured from Local Coordinate Axes

The pitch angle data misrepresents what occurs during the simulation. If the pitch angles in Figure 28 were correct, the vehicle would have pitched upward on impact with the barrier and continued to pitch upward after impact. The simulation data, however, did not show this to be true. For example, at 350 ms, the vehicle pitch angle was approximately zero, and the vehicle was pitching downward, as shown in Figure 29. Similarly, at 540 ms, the vehicle was pitched downward. Thus, the pitch angular data from the local coordinate system at the center of gravity of the vehicle was deemed unusable.

Pitch Angle at 350 ms

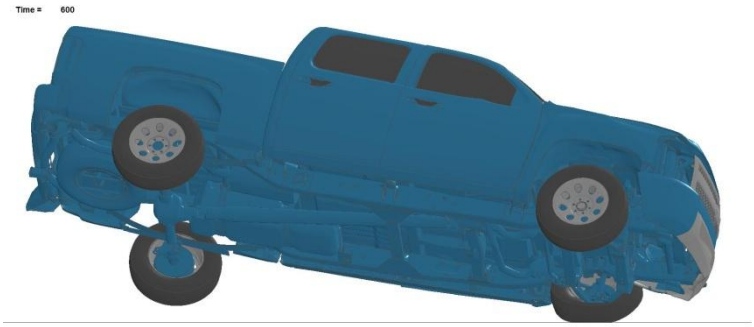

Pitch Angle at 540 ms

Figure 29. Simulated Vehicle Pitch Angle

In order to obtain a more meaningful pitch angle, two points were measured on the vehicle. The longitudinal separation and vertical height differences were used to calculate the pitch angle of the vehicle. In order to obtain an accurate pitch-only measurement, the two points were at roughly the same height (or else pure roll motion slightly changes the difference in height), the points were not taken from parts that deform or move relative to each other. Both points were positioned on the longitudinal centerline of the vehicle. Several different points along the vehicle's length were chosen and reviewed as potential pitch measurement points, but it was very difficult to locate a point that matched the three requirements.

In the center of the bed of the pickup truck, a large square panel was positioned for mounting instruments. This was modeled in the simulated vehicle. The panel

dimensions were 23.6 in. by 23.6 in. (600 mm by 600 mm). The pitch motion was measured using two nodes from this panel along the longitudinal axis of the vehicle, and the result was plotted in Figure 30. It was noted that this pitch angle closely resembled the actual pitch angle from visual inspection of the vehicle during the simulation.

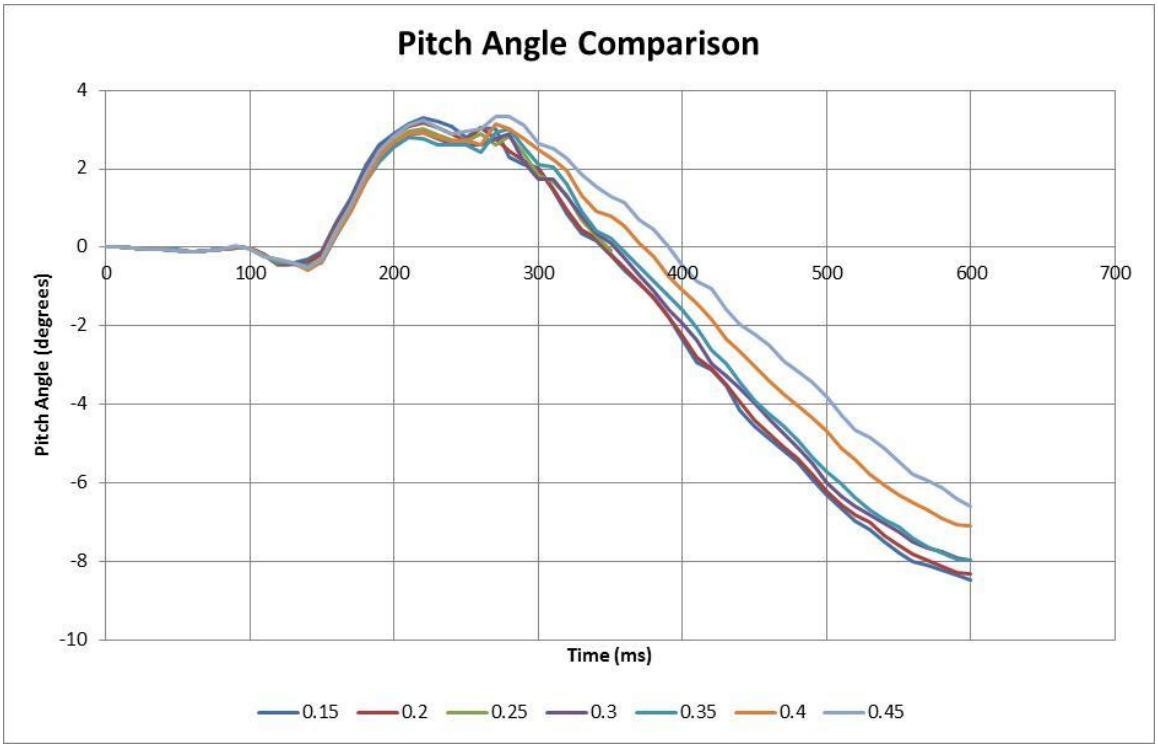

Figure 30. Vehicle Pitch Angle Measured from Instrument Mounting Panel

There was some disparity between the pitch motion of the instrument panel and the pitch motion of the center of gravity of the vehicle. However, for this analysis, the difference between the actual and measured pitch angles was small, and the motion of the plate would be similar to the motion of the actual center of gravity.

Based on the simplified vehicle model in Chapter 4, the vehicle was expected to pitch upward as the front wheel impacted the barrier and began to ride up it. As the vehicle mounted the barrier and as the lateral redirecting force on the vehicle front end

reduced to zero, the vehicle would pitch downward as the rear tires apply a negative moment about the pitch axis. The rear tires contact the barrier and ride up it, further increasing the negative moment about the pitch axis. As the vehicle leaves the barrier, it becomes airborne, and the pitch angle rate became constant. While the vehicle is airborne, it continues to pitch downward. Finally, the vehicle contacted the ground, and the vehicle pitch angle returned to zero. This behavior was imitated by the pitch angles shown in Figure 30.

The simulations incorporating the lowest coefficients of friction between the tire and the barrier had the highest initial and final peak pitch angles. However, the simulations with the higher pitch angles had a higher secondary peak angle. The initial peak pitch angle occurred as the vehicle climbed the barrier. During the tailslap phase, the vehicle pitched downward, and during the airborne stage, the pitch rate remained constant.

5.8.4 Yaw Angle

Yaw angle is initially affected by two forces: (1) the lateral redirecting force on the vehicle and tire from the barrier, and (2) the longitudinal friction force exerted on the tire and vehicle from the barrier. The longitudinal friction force is directly correlated to the lateral redirecting force, although the friction force is smaller than the lateral force (because the coefficient of friction is less than unity). Also, the geometry of the vehicle gives the lateral redirecting force a much larger moment arm than the longitudinal friction force. Thus, the yaw moment caused by the lateral redirecting force is significantly larger than the yaw moment caused by the longitudinal friction force.

The yaw angles are compared in Figure 31 for the varying tire-to-barrier coefficients of friction. The results for each of these runs were very similar, with a near-identical final resting value. However, the yaw rate was slightly less for the simulations with the higher coefficient of friction.

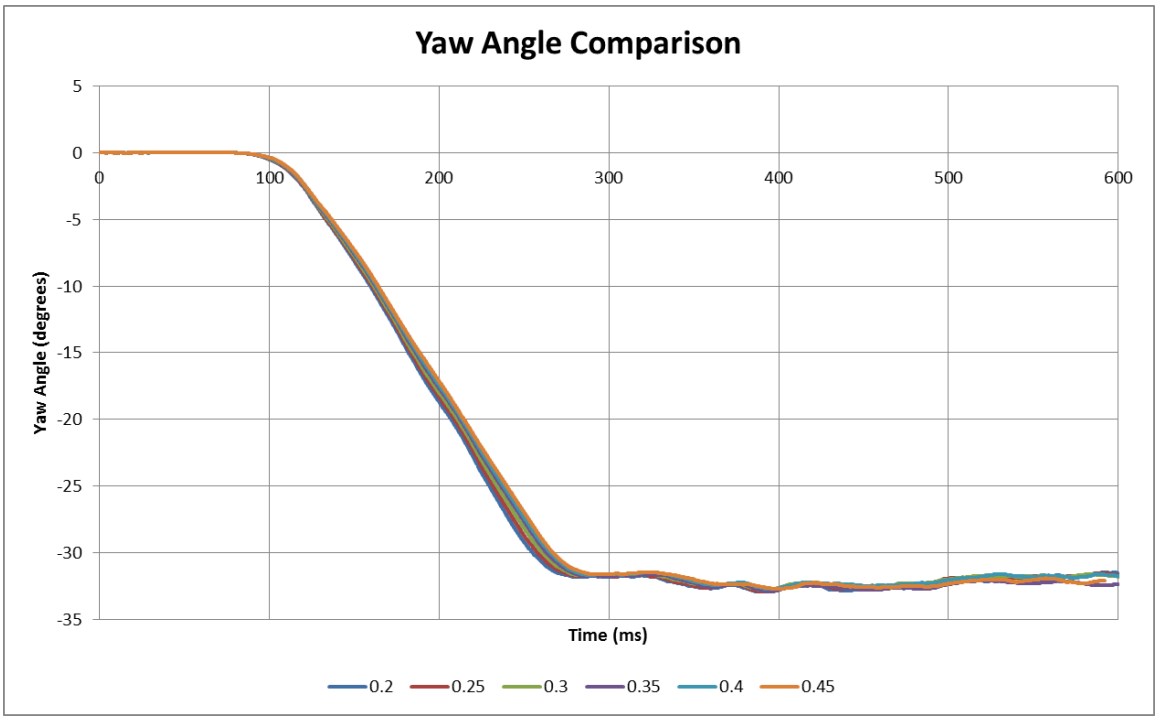

Figure 31. Vehicle Yaw Angle for Varying Tire-to-Barrier Friction Coefficients

5.8.5 Angular Comparison Between Test and Simulation

Angular data from the full-scale crash test are shown in Figure 32. It should be noted that the vehicle roll angle in the full-scale test was opposite the roll angle for the simulations because the full-scale vehicle impacted the barrier with its right side, and the simulated vehicle impacted the barrier with its left side. In the full-scale test, the vehicle initially rolled away from the barrier, whereas in the simulation, the vehicle did not roll away from the barrier at all. Reviewing the forces that affect the vehicle roll motion,

either the lateral force transmitted through the wheel assembly was too large or the upward suspension force was too small.

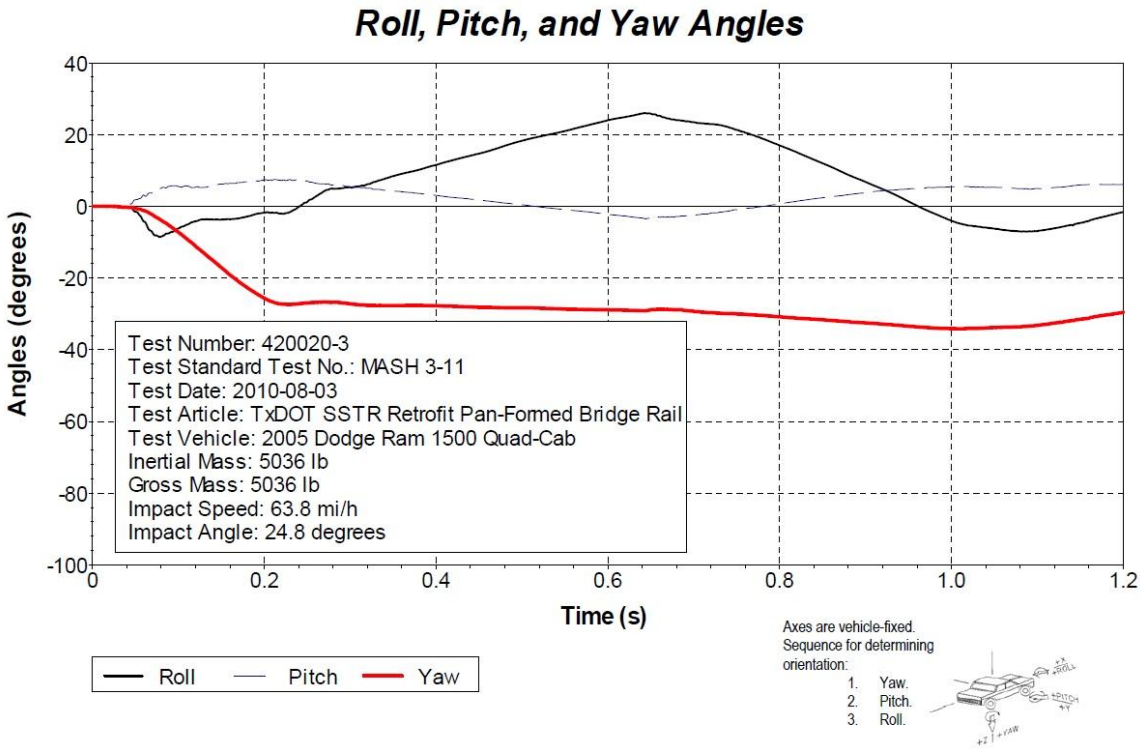

Figure 32. Angular Data from Test No. 420020-3 [6]

Vehicle pitch angle was not as large in the simulation as it was in the full-scale test. Some of this error may be due to how the pitch angle was measured in the simulation. However, based on the results of the roll angle and the tire climb comparisons, the suspension stiffness appeared to be too weak. Thus, some of the difference in the pitch angle could also be attributed to the weak suspension stiffness.

5.8.6 ZOI Results for Tire Friction Simulations

Zone of intrusion is defined as the distance behind the top front corner of the barrier that the vehicle protrudes. The ZOI was defined to prevent harm to the occupants if the vehicle were to contact objects or hazards behind the front face of the barrier. The

ZOI is measured from a point on the vehicle to the top front corner of the barrier as the vehicle protrudes over the barrier. The overall ZOI is assumed to be the point with the farthest protrusion. This excludes vehicle components that are detached from the vehicle.

However, not all vehicle components protruding beyond the barrier may cause harm to the occupant. Unfortunately, little research has been performed to determine which components are critical and which are not. Thus, several important ZOI values were determined and are shown in Table 7. The ZOI was calculated from four points: the front corner of the front fender (which always protruded the farthest), the front corner of the hood, the rear corner of the vehicle, and the edge of the rear door. These points protruded the farthest behind the barrier after impact.

Table 7. ZOI of Varying Tire Coefficients for the 10.8-degree Single-Slope Barrier

Tire-To-Barrier COF	Zone of Intrusion – in. [mm]			
	Front Fender	Corner of Hood	Rear Corner of Box	Edge of Door
0.15	11.4 [289]	8.4 [214]	7.7 [195]	5.5 [141]
0.2	9.9 [251]	8.5 [217]	7.9 [199]	4.9 [124]
0.25	9.9 [252]	8.5 [215]	7.8 [199]	4.1 [103]
0.3	10.1 [258]	8.4 [214]	7.7 [196]	3.4 [87]
0.35	9.8 [248]	8.5 [217]	7.5 [190]	3.0 [75]
0.40	9.5 [242]	8.4 [213]	6.7 [171]	2.8 [70]
0.45	9.7 [247]	8.4 [214]	6.7 [170]	2.5 [63]

The left fender point protruded the farthest behind the barrier in each simulation. After impact, the front corner of the left fender pulled away from the vehicle, as shown in Figure 33. The hood protruded beyond the barrier as well, but it was on average 1.6 in. (40 mm) less than the fender.

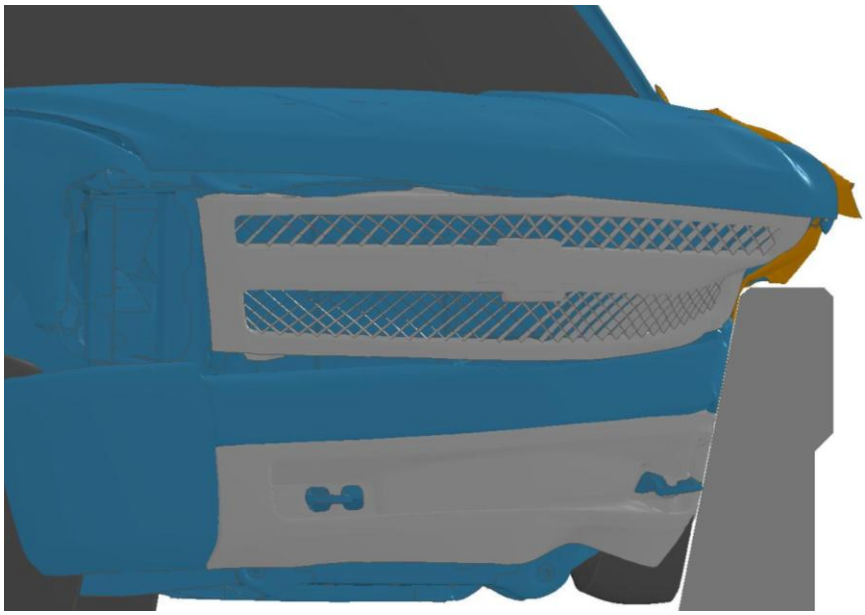

Figure 33. Fender Protrusion Over the Barrier (Note: Fender is orange for distinction)

An impact between the front fender and a hazard behind the barrier may not pose a risk to the occupant. During the initial ZOI study, the fender impacted the rigid pole during the test, which did not pose a significant risk to the occupants, as shown in Figure 34. Longitudinal loads on the fender caused the fender to crush without imparting significant accelerations to the occupant compartment [11]. Thus, if a point on the fender was used to determine the maximum ZOI, it may be too conservative of an estimate of the actual ZOI. The ZOI of the front fender was included in Table 7 for reference. Note that this test did not utilize a dummy occupant and did not take head ejection criteria into consideration.

Figure 34. Fender Impact with a Rigid Pole [11]

The hood of the 2000P vehicle has shown some propensity to be propelled into the windshield of the vehicle, posing a risk to the occupants [10]. Thus, a point on the hood should be considered when evaluating the ZOI. The corner of the hood may not pose a risk to the vehicle occupants, and using the corner as the maximum ZOI point will provide a conservative estimate of the true ZOI of the vehicle impacting the barrier. As of

this study, there is no research available defining the location of the critical ZOI points on the vehicle.

Door protrusion poses a risk to the occupant for several reasons. First of all, an impact between the top of the door and a rigid object behind the barrier could cause protrusion into the occupant compartment. Also, depending on the connection between the door and the vehicle, an impact with the door could cause excessive accelerations of the occupant compartment. Finally, during an impact event, the occupant contacts the door and the head of the dummy impacts the window, potentially fracturing the glass and extending out of the cab.

While the head ejection criteria has been developed for 2000P pickups, the head ejection has not been studied with the 2270P vehicle, and there may be potential for the occupant to contact hazards outside of the vehicle. It should be noted that prior crash tests utilizing a test dummy in the Dodge Ram 1500 Quad Cab pickup truck have not shown a significant difference in the deflection of the top of the door with and without a dummy in the impact-side seat [17,20]. Thus, it is believed that the door protrusion without the dummy is an accurate representation of the actual ZOI of the door during an impact. However, this does not represent the protrusion of a dummy head out of the window.

While impacts with the rear of the vehicle would not cause direct penetration into the occupant compartment, large forces exerted on the rear of the vehicle could cause excessive occupant compartment accelerations or adversely affect the trajectory of the vehicle.

5.8.7 Recommended Tire-to-Barrier Friction Coefficient

Low coefficients of friction tend to increase the zone of intrusion of the barrier system while still showing fairly accurate gross vehicle motion during and after the impact sequence. The rear corner of the vehicle and the impact-side door showed the largest decrease in ZOI as the tire friction increased because it reduced the yaw rate, which decreased the magnitude of the tailslap impact. However, the tire-to-barrier coefficient of friction did not greatly affect the maximum zone of intrusion.

Larger coefficients of friction incur larger frictional forces, which tend to cause increased propensity for tearing and deformation of the components, increasing the computation cost and making the simulation less stable. Thus, it was recommended that the tire-to-barrier coefficient of friction be reduced to 0.15.

5.9 Vehicle Body-to-Barrier Friction Coefficient

Simulations were performed while varying the coefficient of friction between 0.05 and 0.40 between the vehicle body and the barrier. This effort was completed while maintaining the coefficient of friction at 0.15 between the tire and the barrier. Vehicle positions at the maximum ZOI during the impact and tailslap phases were reviewed, and the vehicle positions from the models using COF's of 0.05 and 0.40 are shown in Figure 24.

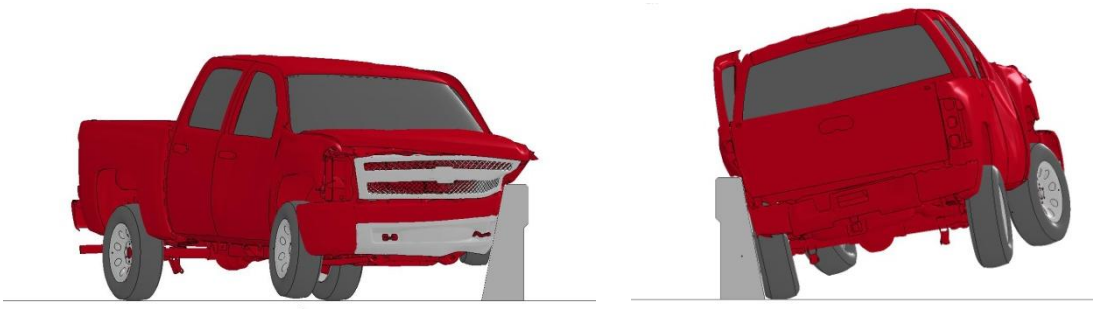

COF = 0.05

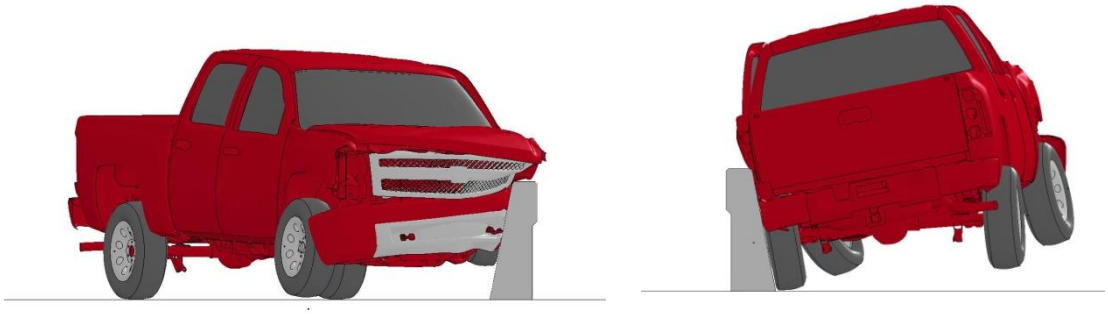

COF = 0.40

Figure 35. Maximum ZOI Positions for Low and High Vehicle-to-Barrier COFs

5.9.1 Vehicle Vertical Displacements

A comparison of the vertical vehicle displacements during the simulations is shown in Figure 36. Similar to the tire-to-barrier coefficient of friction, the vehicle body-to-barrier friction coefficient increased the resistance to vertical motion by the vehicle. Thus, higher coefficients of friction will reduce the vertical displacement of the vehicle.

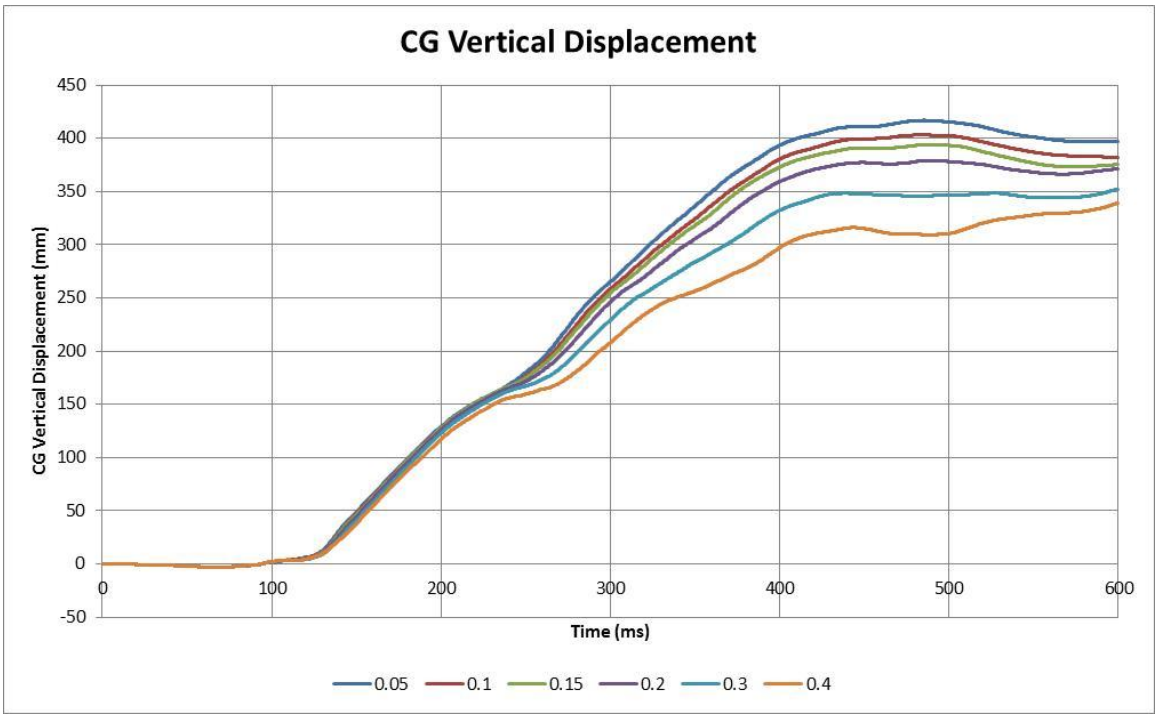

Figure 36. Vehicle Vertical Displacement

5.9.2 Roll Angle

The vehicle roll angles from the simulations are shown in Figure 37. The simplified vehicle model predicted that the vertical friction force between the vehicle and the barrier would induce a roll angle toward the barrier. This would suggest that higher friction coefficients have higher initial roll angles as the vehicle climbs the barrier. However, as the vehicle continues to climb the barrier, the roll motion would be resisted by the vertical friction force, and the roll angle should then decrease for larger coefficients of friction. This behavior was seen in the roll angles, as shown in Figure 37a. The simplified vehicle model predicts that the end roll angle should be lowest for higher coefficients of friction, which was also witnessed in the simulation results, as shown in Figure 37b.

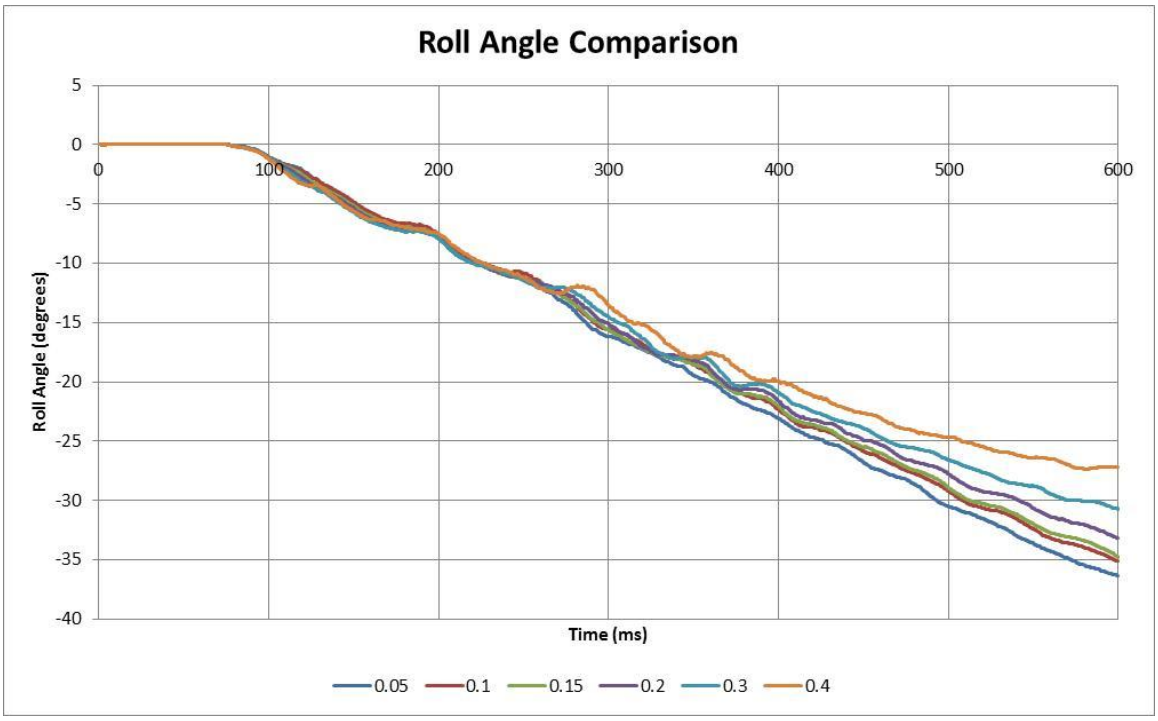

a. Overall Vehicle Roll Motion

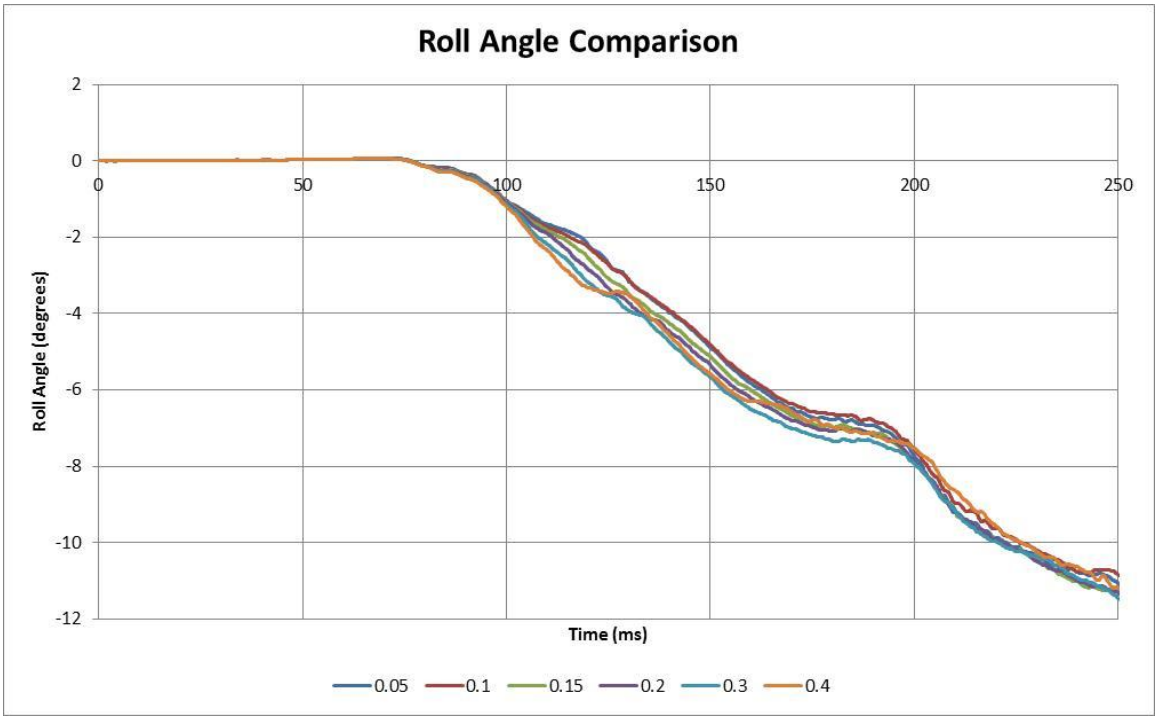

b. Vehicle Roll Motion Prior to Rear Wheel Impact with Barrier

Figure 37. Vehicle Roll Angle

5.9.3 Yaw Angle

The yaw angles for the simulations are shown in Figure 39. The friction force on the vehicle from the barrier creates an unbalanced moment about the center of gravity, which resists the natural redirection of the vehicle due to the moment created by the lateral redirecting force. Thus, higher coefficients of friction should cause the vehicle to have lower redirection rates, and the tailslap of the vehicle should occur later in the impact sequence.

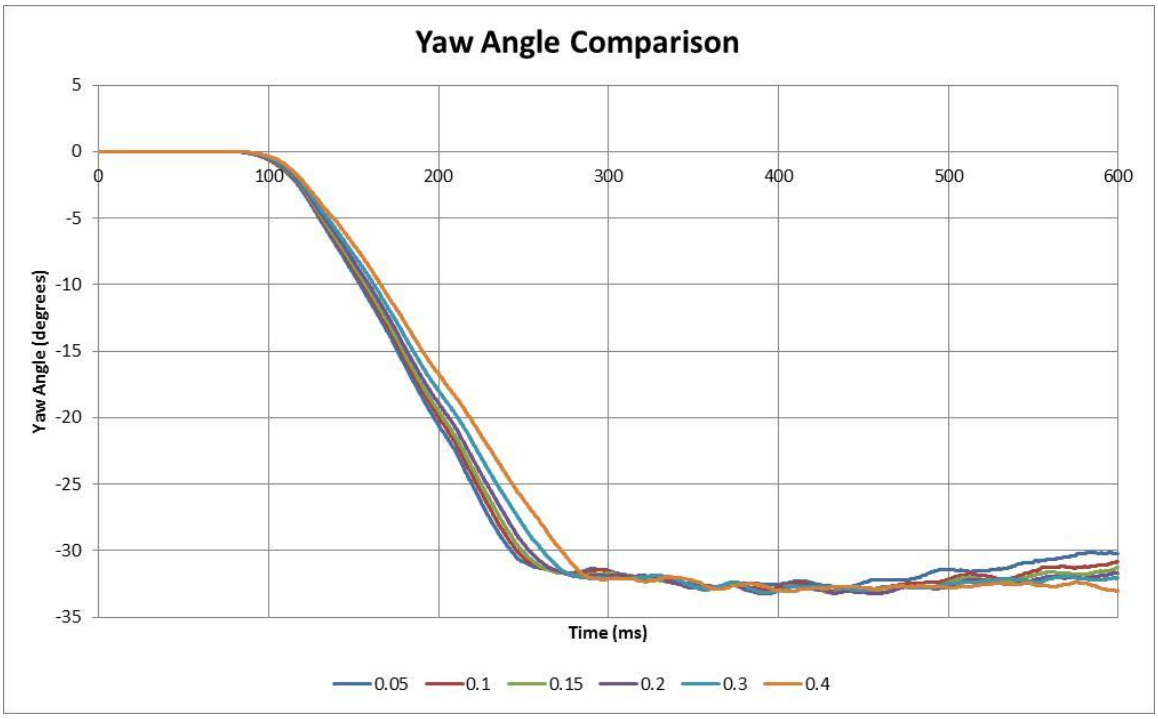

Figure 38. Vehicle Yaw Angle

5.9.4 Pitch Angle

Vehicle pitch angles, as measured from the instrument mounting panel in the bed of the pickup truck, are shown in Figure 39. The simplified vehicle model predicted that for higher vehicle body-to-barrier coefficients of friction, the pitch motion should be damped, just like what was seen in the parameter study involving the tire coefficient of

friction. However, this was not seen in the simulation results. Instead, the simulation results show that higher coefficients of friction initially reduce the pitch angle of the vehicle. As the rear of the vehicle impacted the barrier, the vehicle pitched downward. However, the increased coefficient of friction between the vehicle body and the barrier did not resist the negative pitch motion, and the higher friction values caused the vehicle to have a larger negative pitch than the lower friction values.

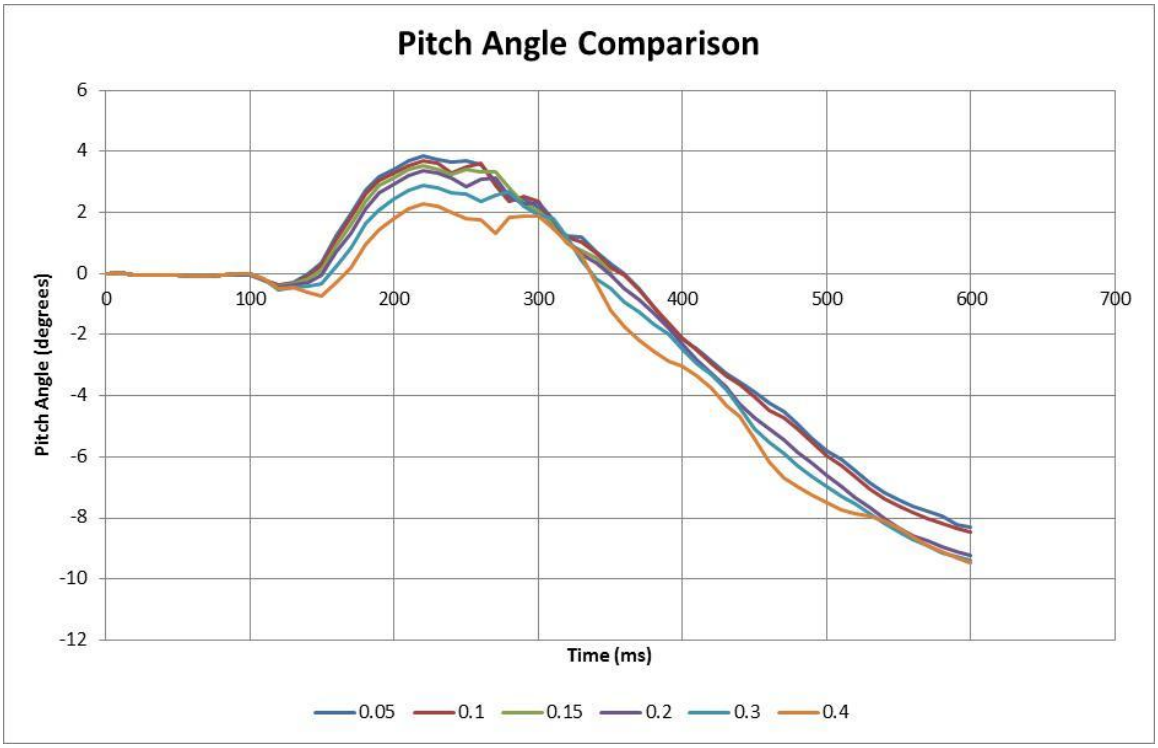

Figure 39. Vehicle Pitch Angle

5.9.5 Contact Force Analysis

The SAE 60 filter was applied to the contact forces between the vehicle body and the barrier, and the results were plotted, as shown in Figure 40. The orientations of the contact forces is shown in Figure 41. The contact forces showed two distinct peaks occurring in the impact and tailslap phases.

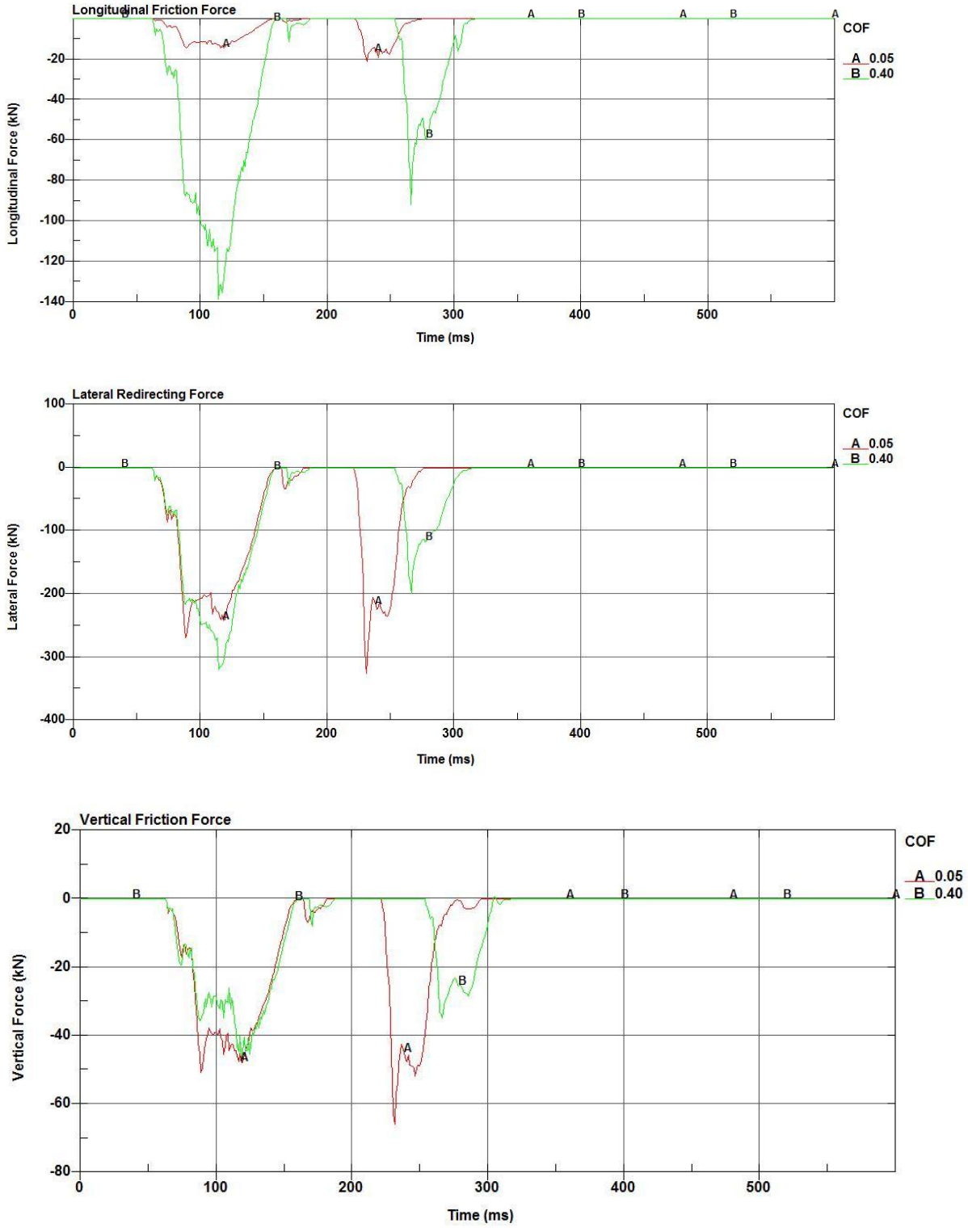

Figure 40. Contact Forces Between the Vehicle Body and Barrier

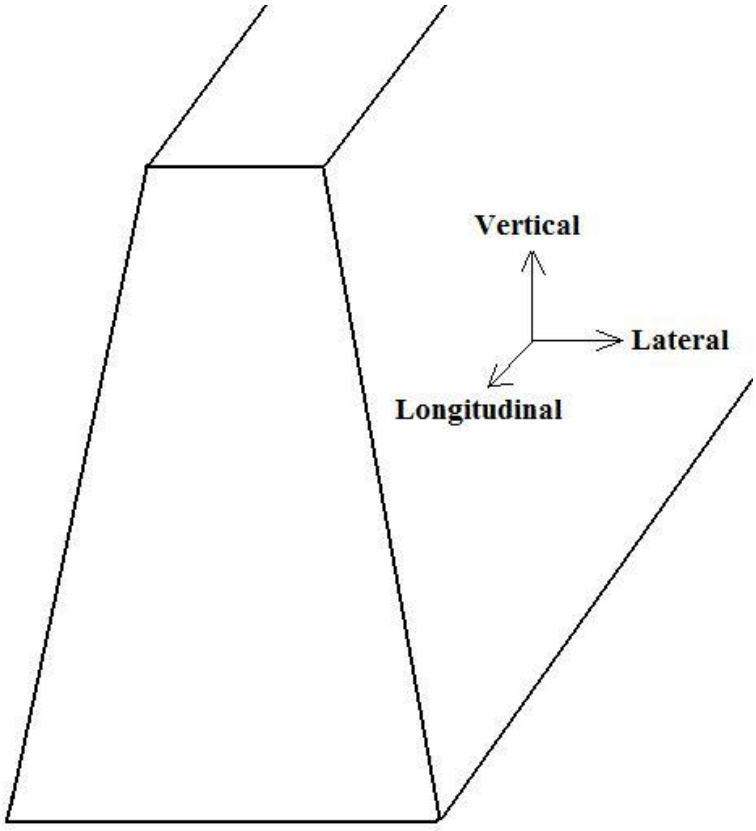

Figure 41. Contact Forces Orientations

Tailslap into the barrier occurred later for the simulation with a higher coefficient of friction. However, the vertical forces acting on the vehicle were significantly lower for the higher coefficient of friction. During the impact phase, the vehicle vertical motion was relatively small, so the vertical resisting force was also small. Also, the highest coefficient of friction experienced the lowest pitch angle, which contributed to the lower vertical force. For the rear impact into the barrier, the lateral redirecting force was lower for the higher coefficient of friction. As the vehicle redirected, the vehicle with the lower coefficient of friction redirected at a more rapid pace. The sharp rear impact into the barrier counteracted this rapid redirection and caused the vehicle to exit the barrier. For the higher coefficient of friction, the lower redirection rate did not require as large of a

lateral force on the rear of the vehicle to cease the vehicle yaw motion, which consequently caused lower friction forces.

5.9.6 ZOI Results for Vehicle Friction Simulations

The working width was determined for each simulation and is shown in Table 8. The working width peaked at a coefficient of friction of 0.10. The working width decreased at very low coefficients of friction. This occurred because the vertical frictional force acting on the front fender prevented the fender from sliding up the barrier at the time of maximum zone of intrusion. For lower friction coefficients, the vehicle would merely climb up the barrier and not have as much vehicle crush at that location. For higher friction coefficients, the vehicle's front end experienced significant lateral drag as it slid along the barrier. This caused deformation of the front fender, which was the point where the ZOI was measured.

Table 8. Zone of Intrusion – Varied Vehicle Body-to-Barrier COF

Vehicle-to-Barrier COF	Zone of Intrusion – in. [mm]			
	Front Fender	Corner of Hood	Rear Corner of Box	Edge of Door
0.05	10.7 [271]	7.8 [199]	8.4 [212]	8.1 [207]
0.10	11.2 [285]	8.2 [207]	7.9 [199]	6.9 [175]
0.15	10.9 [277]	8.3 [212]	7.8 [198]	6.5 [164]
0.20	10.3 [261]	8.6 [219]	7.7 [195]	5.6 [142]
0.30	10.9 [277]	8.7 [221]	7.5 [191]	4.6 [116]
0.40	10.5 [267]	8.9 [226]	8.2 [209]	3.1 [80]

5.9.7 Recommended Vehicle-to-Barrier Friction Coefficient

With the exception of the pitch angle, vehicle behavior was most severe at lower vehicle-to-barrier coefficients of friction. Higher coefficients of friction softened the tailslap phase impact between the vehicle and the barrier, and the net yawing moment about the center of gravity was less due to the longitudinal friction force on the front fender.

The largest protrusion over the barrier from the front fender occurred at a friction coefficient of 0.10, but, as stated in Section 5.8.7, a longitudinal impact between the fender and a rigid hazard may not pose a risk to the vehicle's occupants. Hence, the critical vehicle-to-barrier friction coefficient was chosen based on the other three ZOI points.

As the friction coefficient increased, the hood protrusion behind the barrier increased. This occurred because the increased friction created a yaw moment towards the concrete barrier. With an increase in the friction coefficient, the rear corner of the

vehicle and the corner of the door did not protrude as far behind the barrier. Also, at higher friction values, the model showed greater instability. Thus, a lower friction value was desired for stability. At all coefficients of friction larger than 0.05, the maximum ZOI point occurred at the corner of the hood. The difference between the maximum ZOI point at friction values of 0.10 and 0.40 was 0.7 in. (19 mm). Based on the model stability and the severity of the ZOI values at each point, it was decided that the coefficient of friction for the vehicle body-to-barrier contact should be 0.10.

5.10 Elastic Barrier Study

The barrier material can greatly affect the behavior of the system. In most simulated permanent concrete barrier systems, the barrier is modeled out of rigid material. While the rigid material is a good approximation for the barrier behavior, no material is perfectly rigid, and there is some elastic response in the barrier. However, LS-DYNA contact algorithms do take into account the actual material properties in determining reaction forces. Thus, parts defined as rigid behave somewhat elastically when impacted.

Modeling the barrier as an elastic, deformable material is more computationally expensive. To determine the benefit of an elastic barrier, the barrier was modeled as an elastic material and compared to the behavior of the model using the rigid material definition.

The barrier was split into three sections – a 26.9-ft (8.2-m) long elastic section for the length of contact with the vehicle and two rigid barrier portions for the ends of the barrier serving as anchorage for the elastic barrier and for visual effect. The elastic barrier

was modeled as shell elements having a density of 8,300 lb/ft^3 (60,000 kg/m^3), a Poisson's ratio of 0.28, and a stiffness of 2,900 kpsi (20 GPa).

For the first simulation, the barrier was constrained along the upstream and downstream ends of the 26.9-ft (8.2-m) long elastic barrier section. The bottom edge of the barrier was free to move laterally. The first simulation utilizing the elastic barrier encountered unrealistic barrier deformations. The base of the barrier deformed 2.6 in. (65 mm) laterally inward, and the center of the barrier deformed 1.6 in. (40 mm) laterally inward.

The lateral movement of the base of the barrier diverged from the physical testing results significantly. Permanent concrete barriers are often cast into the ground, and the base of the barrier deflection is negligible. Thus, the base of the barrier was fixed to prevent movement, and the simulation was performed again. The barrier had the same properties as before, and the maximum deformation seen in the barrier was measured as 1.1 in. (28 mm) at a height of 22.2 in. (563 mm). While this represented a marked improvement in the barrier motion, the deflection of the barrier was still unreasonable.

To determine the effect of barrier stiffness on the vehicle motion and the ZOI, the barrier stiffness was altered. In the previous simulations, the barrier stiffness was 2,901 kpsi (20 GPa). The barrier stiffness was changed to 5,802 kpsi (40 GPa) and 1,450 kpsi (10 GPa), which resulted in maximum barrier deformations of 0.68 in. (17 mm) and 1.7 in. (43 mm), respectively. A summary of the barrier deformation for each condition simulated is given in Table 9. The ZOI measured for each test is also shown in Table 9.

Table 9. Elastic Barrier Study Summary

Restrained / Unrestrained Barrier Base	Barrier Stiffness kpsi (GPa)	Max Barrier Deformation in. (mm)	ZOI – in. (mm)			
			Front Fender	Hood	Rear Corner of Box	Door
Unrestrained	2,901 (20)	2.6 (65)	11.5 (292)	8.6 (218)	9.0 (229)	6.5 (166)
Restrained	2,901 (20)	1.1 (28)	11.7 (296)	8.6 (219)	7.9 (201)	6.0 (153)
Restrained	5,802 (40)	0.68 (17)	11.2 (284)	8.3 (210)	7.1 (180)	6.0 (152)
Restrained	1,450 (10)	1.7 (43)	12.3 (313)	8.9 (226)	8.3 (210)	5.7 (144)

Barrier deformation at the impact location varied for each simulation. As noted previously, the differing barrier profile at the impact location may affect the post-impact trajectory of the vehicle. The barrier shape at impact was found by taking a cross-section of the barrier at impact and showing the initial and final deformed states, as shown in Figure 42. The deformed barrier shapes for each of the elastic barrier simulations are shown in Figure 43.

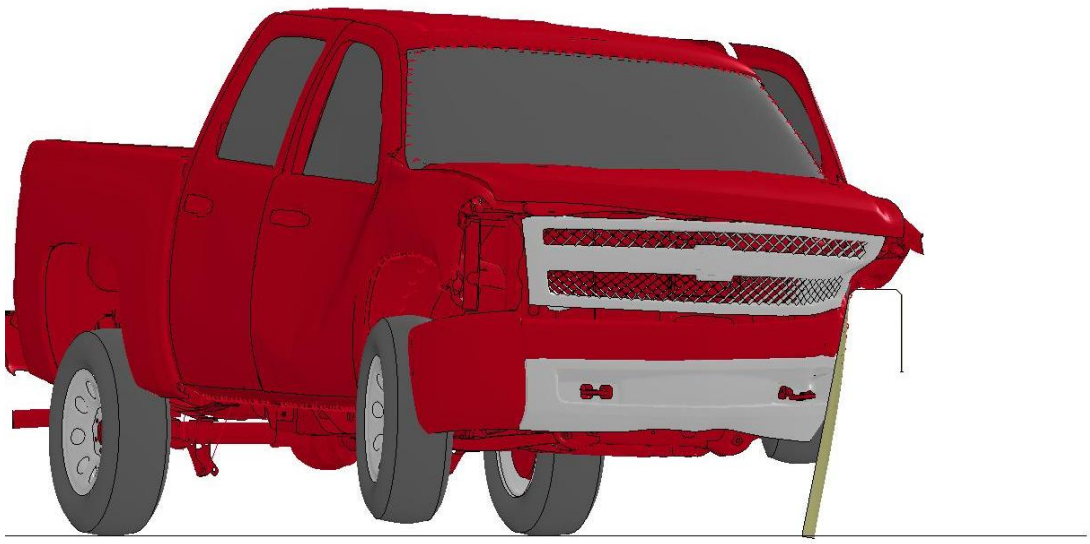

Figure 42. Elastic Barrier Deformation during Impact

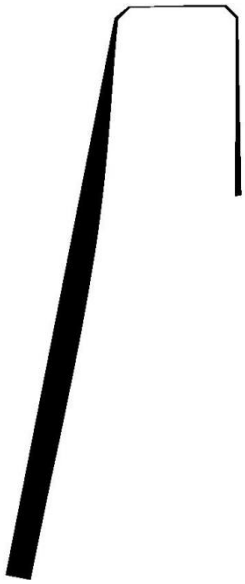

Unrestrained Barrier Base
20 GPa Barrier Stiffness

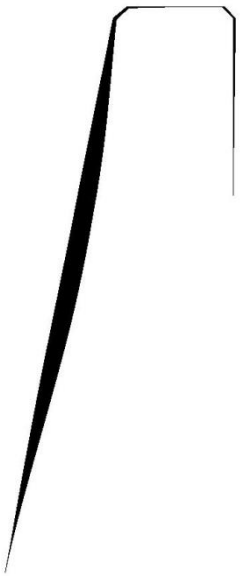

Restrained Barrier Base
20 GPa Barrier Stiffness

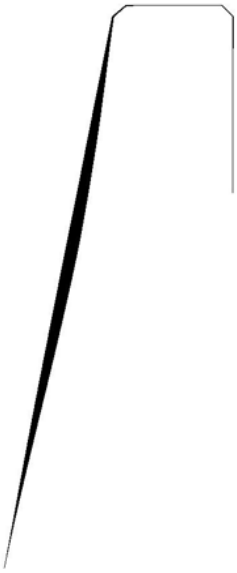

Restrained Barrier Base
40 GPa Barrier Stiffness

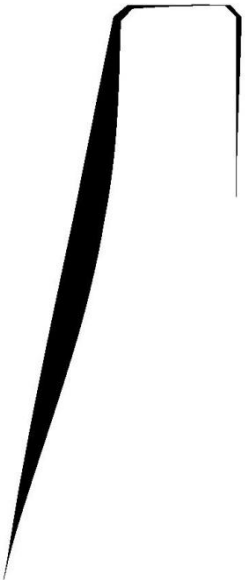

Restrained Barrier Base
10 GPa Barrier Stiffness

Figure 43. Deformed Barrier Shapes for Each Elastic Barrier Simulation

The internal energy of the barrier was reviewed to determine how much energy was absorbed by the barrier during the impact. The pre-impact lateral kinetic energy (or impact severity) of the vehicle prior to impact is given by

$$Impact\ Severity = \frac{1}{2}mV^2\sin(\theta)$$

where m is the mass of the vehicle, V is the velocity of the vehicle, and θ is the impact angle. For the simulated impact, the impact severity was 273.0 kip-ft (370.1 kJ). In comparison, the peak energy absorbed by the elastic barrier was nearly 50 times less than this. Energy absorbed by the concrete barrier is shown in Figure 44. Thus, the vehicle's angular motions, vertical deflection, and deformations account for at least 98% of the lateral energy transfer.

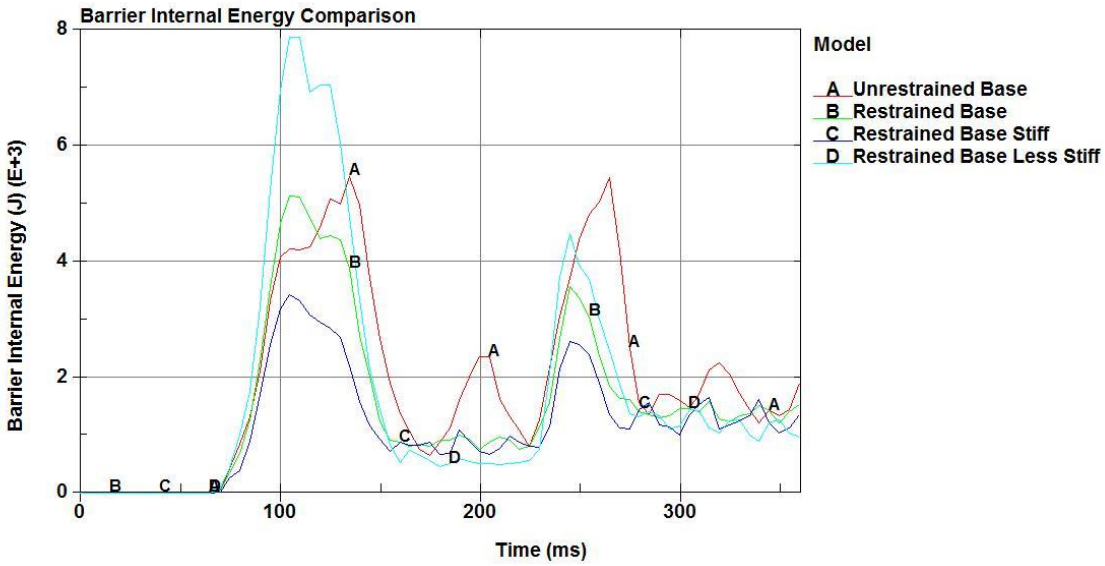

Figure 44. Energy Absorbed by the Elastic Barrier

Vehicle trajectories for the elastic barrier simulations were compared to the rigid barrier. The vehicle roll angle and c.g. height are plotted through 200 ms in Figures 45 and 46. The roll motion of the vehicle was nearly identical for each simulated case

throughout the impact phase. The unrestrained elastic barrier showed the largest roll angle, while the restrained elastic barrier simulations showed the lowest roll angle. As for the vertical deflection, as the barrier stiffness increases, the maximum vehicle c.g. height increased, and the rigid barrier showed the highest c.g. deflection. However, the maximum height difference between the stiff elastic, less-stiff, and rigid barrier simulations was less than 5%.

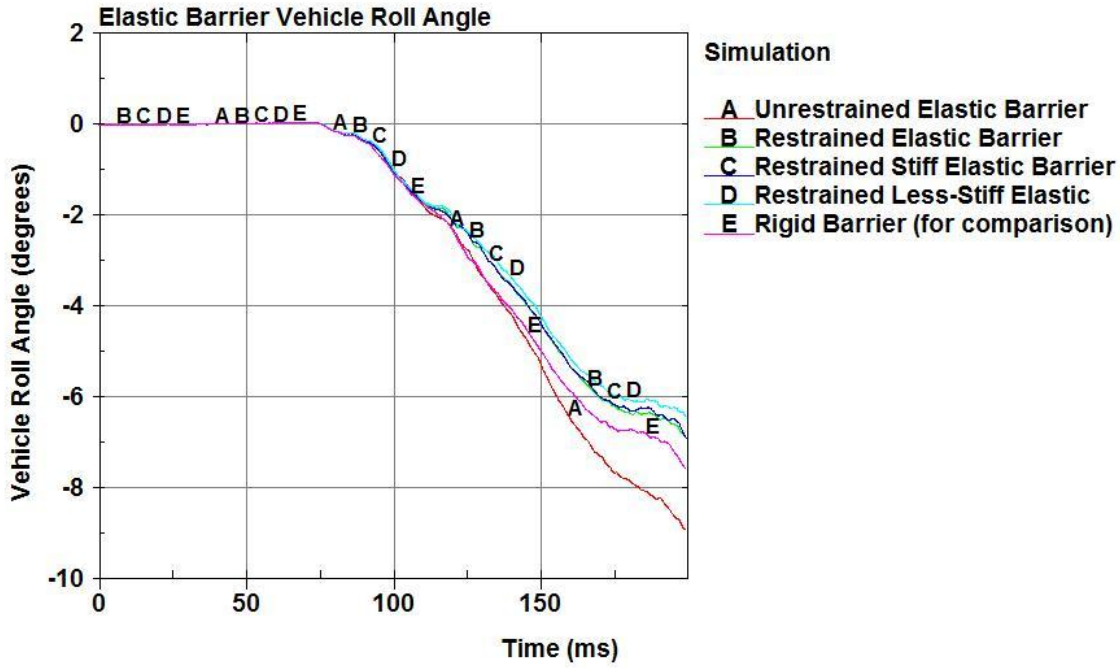

Figure 45. Vehicle Roll Angle Comparison for Elastic Barrier Impacts

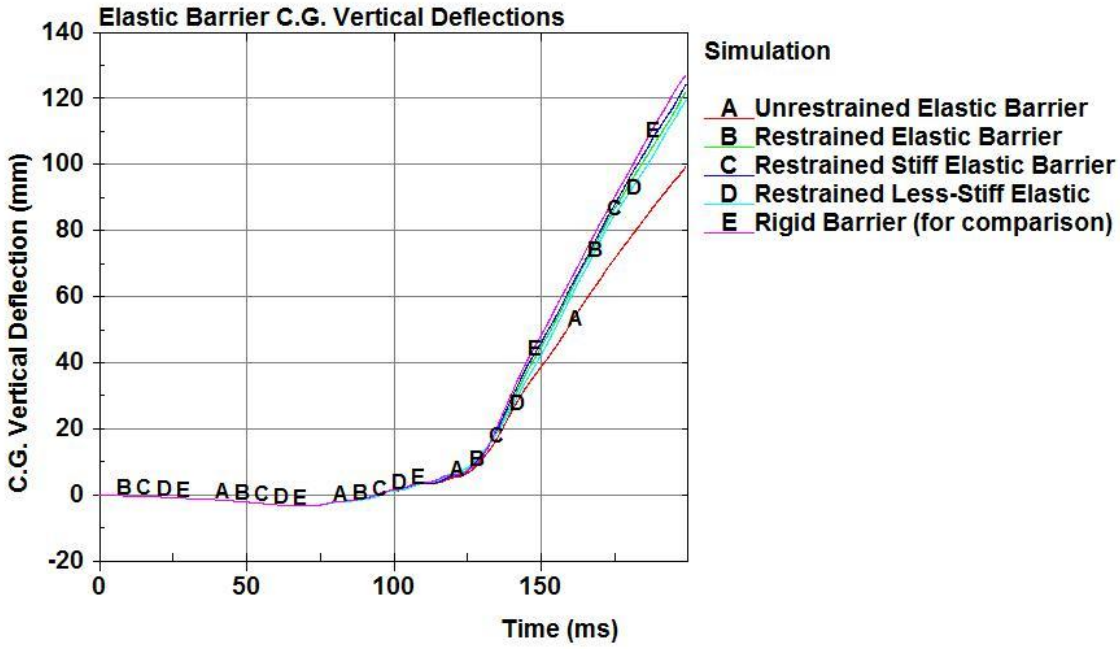

Figure 46. Vehicle C.G. Vertical Motion Comparison for Elastic Barrier Impacts

Simulations with the elastic barrier decreased the computational time. The elastic barrier simulations were each calculated with a 200 ms simulation duration on 16 processors, and the time required to compute these simulations is shown in Table 10. The difference in computation time between the rigid and elastic barrier systems was approximately 21%.

Table 10. Elastic Barrier Computation Time Comparison

Simulation Conditions	Time (hours minutes seconds)
Rigid Barrier	13h 43m 55s
Unrestrained Elastic Base	10h 1m 8s
Restrained Elastic Base	10h 56m 43s
Restrained Elastic Base, Stiffer Barrier Material	10h 33m 41s
Restrained Elastic Base, Less-Stiff Barrier Material	10h 46m 51s

5.10.1 Conclusions

Based on the results of the elastic barrier study, the restrained elastic barriers showed a higher ZOI, lower roll angles, and lower c.g. height deflections than the rigid barrier. While unreasonable deformations were seen in the unrestrained concrete barrier, the dynamic compression of the concrete barrier was not evaluated during this study. For simplicity's sake, the barrier was modeled as a rigid barrier, but it is recommended for future simulations that the barrier be modeled as an elastic material.

6 ZOI SIMULATION MODELS

The baseline model used to determine the ZOI values is shown in Figure 47. The 36-, 42-, and 56-in. (914-, 1,067-, and 1,422-mm) tall, single-slope concrete barriers were modeled according to standard 14B32 of the Wisconsin Department of Transportation. The three different barrier profiles are shown in Figure 48. In the baseline vehicle model, the suspension joints did not fail, and the impacting tire did not deflate.

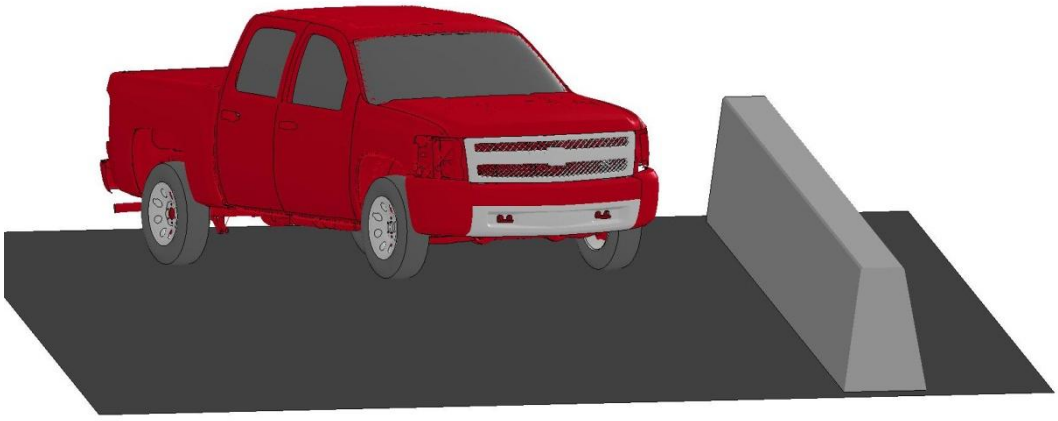

Figure 47. Baseline Simulation Model Used to Determine ZOI

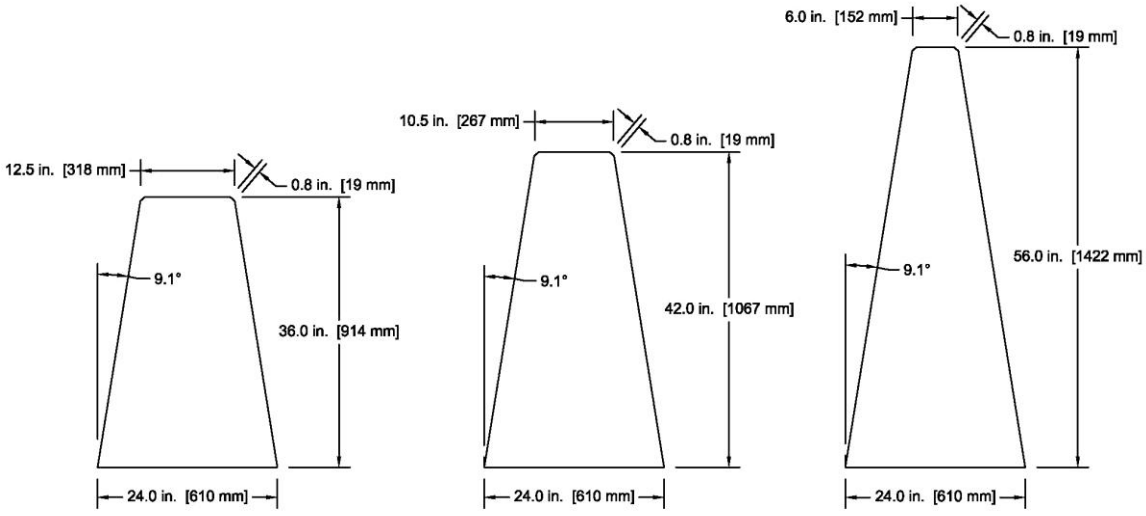

Figure 48. Simulated 9.1-degree Barrier Profiles

Based on the results of the Texas 10.8-degree single-slope barrier simulations, the barrier was chosen to be rigid material with a mesh size of 0.79 in. (20 mm). For contact purposes, the elastic modulus was defined as 4.64 Mpsi (32.0 GPa), and the Poisson's ratio was 0.20. Both of these values were consistent with actual concrete. The coefficient of friction between the tires and the concrete barrier was 0.15, and the coefficient of friction between the vehicle and the barrier was 0.10.

7 ZONE OF INTRUSION ANALYSIS

7.1 Baseline Evaluation

The ZOI was evaluated initially by impacting the 2270P vehicle model into the three barriers shown in Figure 48. No modifications were made to the vehicle suspension or tires. Comparisons were made between the three simulations to determine the effect of barrier height on the impact performance of the barrier.

7.1.1 Vehicle C.G. Height

The vehicle c.g. heights during the simulations were measured and plotted in Figure 49. Overall, the vehicle c.g. height was fairly consistent between the 42-in. and 56-in. (1,067-mm and 1,422-mm) tall barrier impacts. However, the 36-in. (914-mm) tall barrier impact caused the vehicle to climb up the barrier over 4 in. (102 mm) more than the taller barriers. Forces occur at two distinct periods; the first during the impact phase and the second during the tailslap phase.

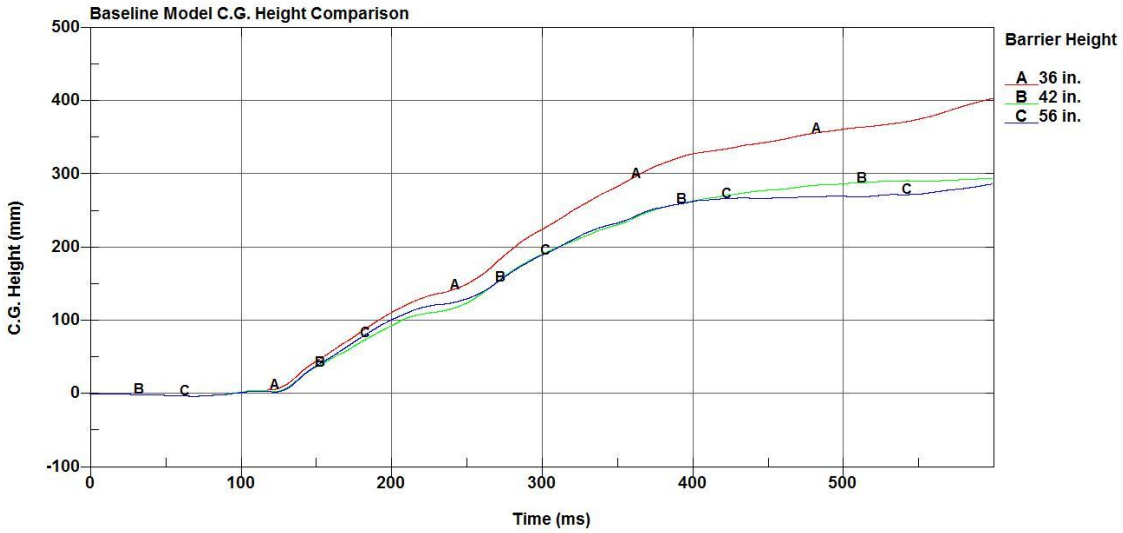

Figure 49. Baseline 9.1-degree Single-Slope Barrier Simulation C.G. Height Comparison

7.1.2 Contact Force Analysis

Vertical forces between the vehicle and the barrier were filtered with an SAE 60 filter and plotted for different vehicle components for the 36-in. (914-mm) barrier simulation, as shown in Figure 50. The vertical force between the vehicle body and the barrier was larger than the vertical force between the barrier and either of the tires.

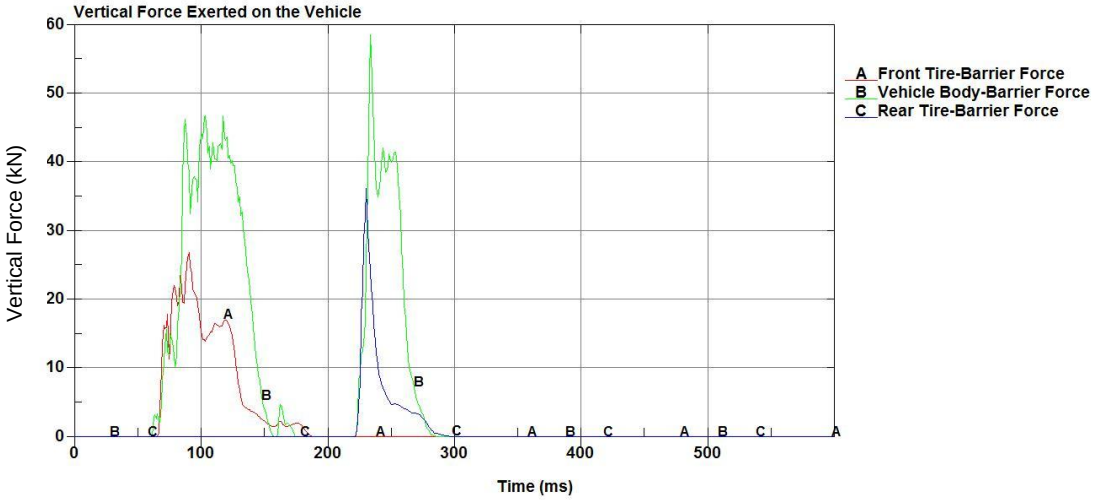

Figure 50. Contact Forces by Component

Total vertical forces between the vehicle and the barrier were plotted for each barrier height, as shown in Figure 51. The peak vertical forces were nearly identical for the 36-, 42-, and 56-in. (914-, 1,067-, and 1,422-mm) tall barriers. However, the 42- and 56-in. (1,067- and 1,422-mm) barriers showed a steep decline following the peak vertical force. Vertical forces on the vehicle from the 36-in. (914-mm) tall barrier did not decline as rapidly.

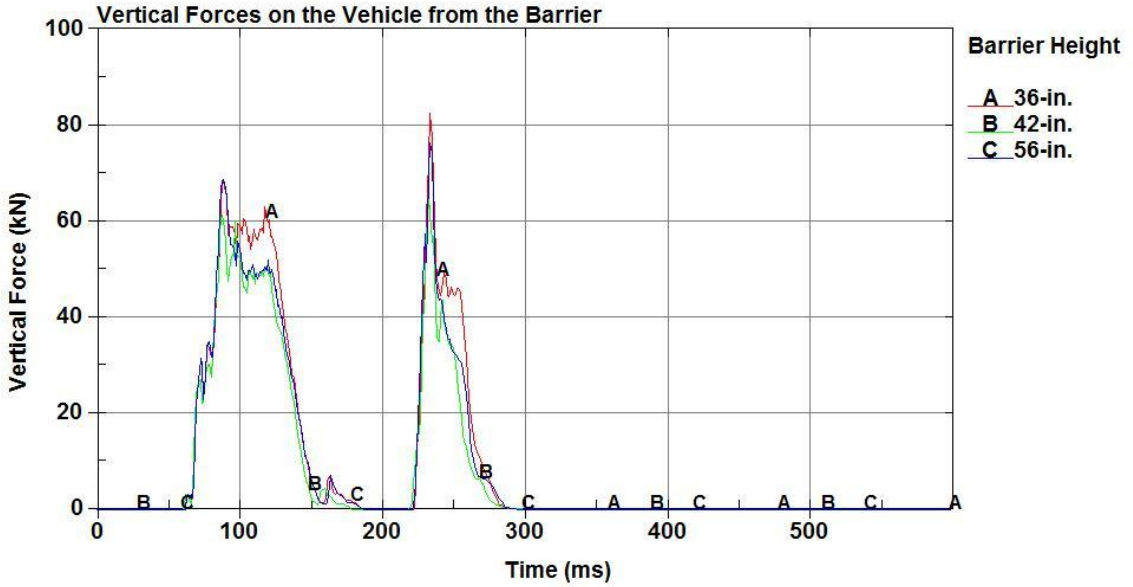

Figure 51. Total Vertical Force Between the Vehicle and Barrier

7.1.3 Roll Angle

As the vehicle was redirected, the roll angle of the vehicle increased. Increased vehicle roll pressed the vehicle into the top of the barrier, causing the vehicle to be lifted in the air, as shown in Figure 52. Aside from the vertical force exerted on the vehicle, the vehicle rolled about the base of the barrier, so the vehicle c.g. lifted up as the roll angle increased. The roll angle was largest for the vehicle impacting the 36-in. (914-mm) tall barrier, as shown in Figure 53. With the vehicle rolling about the toe of the barrier, the vehicle center of gravity rose vertically with increased roll angle.

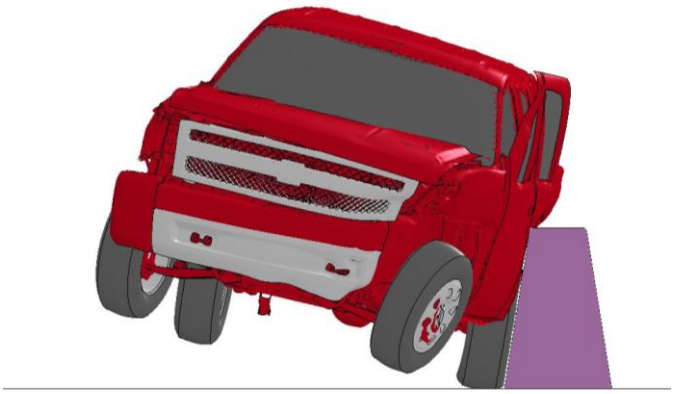

Figure 52. Vehicle Roll Toward the Barrier

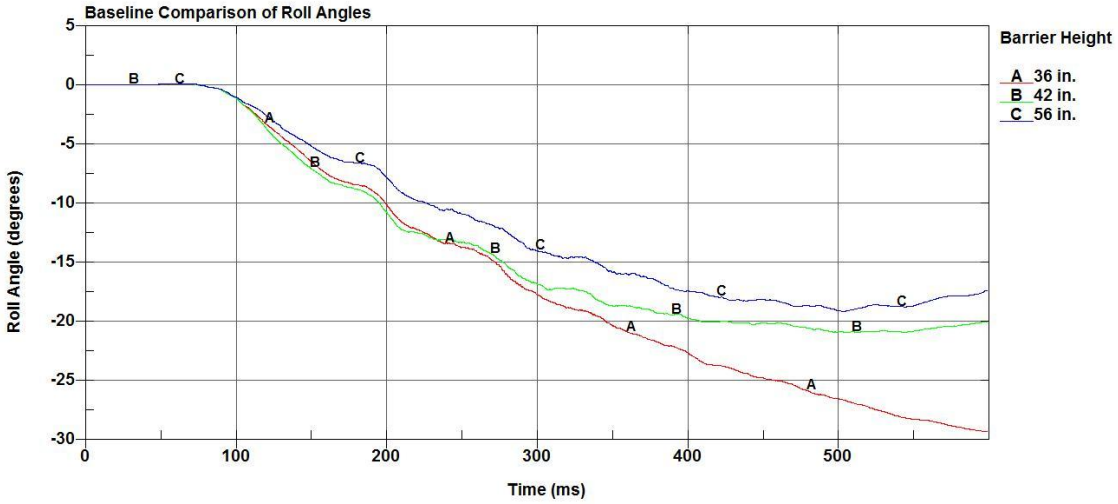

Figure 53. Baseline 9.1-degree Single-Slope Barrier Simulation Vehicle Roll Angles

Vehicle roll into the barrier was caused by the lateral force at the bottom of the tire and at the fender below the vehicle c.g. With the shorter barriers, the maximum roll angle was higher, as shown in Figure 53. With taller barriers, the upper part of the barrier exerted a lateral force on the vehicle above the vehicle c.g., which created a moment counteracting the vehicle roll toward the barrier. This moment was smaller in shorter barriers, which meant higher overall roll angles.

7.1.4 Yaw Angle

The vehicle yaw angle was plotted for each barrier height, as shown in Figure 54. While some variation existed between the three runs, the yaw angle was fairly consistent; the barrier height does not affect the vehicle yaw angle significantly.

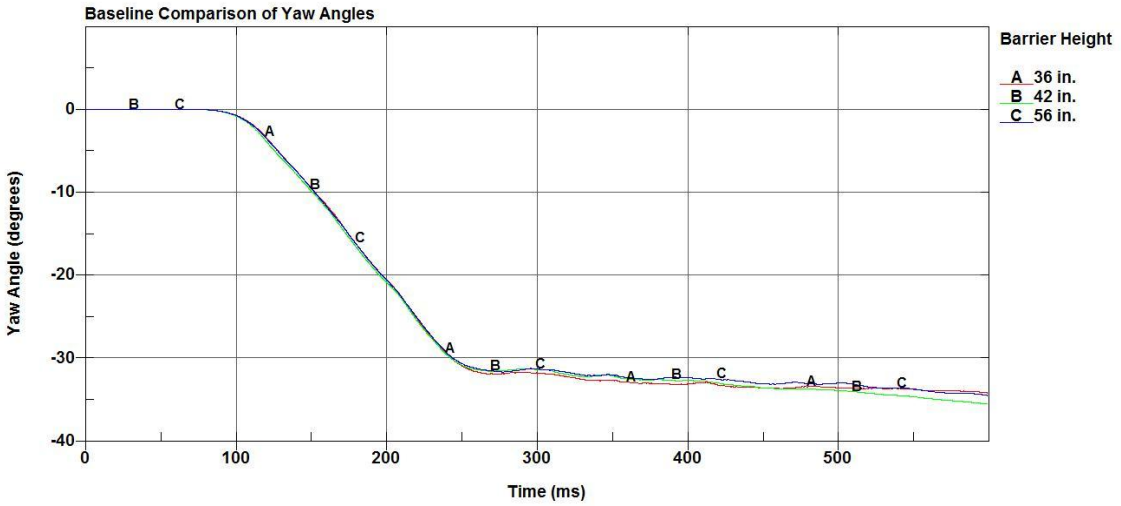

Figure 54. Baseline 9.1-degree Single-Slope Barrier Simulation Vehicle Yaw Angle

7.1.5 Pitch Angle

Vehicle pitch angle was difficult to measure, as discussed in Section 5.8. After plotting the pitch angles, the results varied widely, as shown in Figure 55. The 42-in. (1,067-mm) tall barrier experienced the lowest pitch angle, while the 36-in. and 56-in. (914-mm and 1,422-mm) tall barriers both experienced similar pitch behavior. Vehicle pitch motion was caused by sudden compression of the left-front suspension as the impacting tire contacted the barrier and began to climb up the barrier. As the vehicle redirected away from the barrier, the two front tires became airborne, and the front of the vehicle pitched downward. As the vehicle traveled forward, the front of the vehicle contacted the ground, and the front of the vehicle pitched upward.

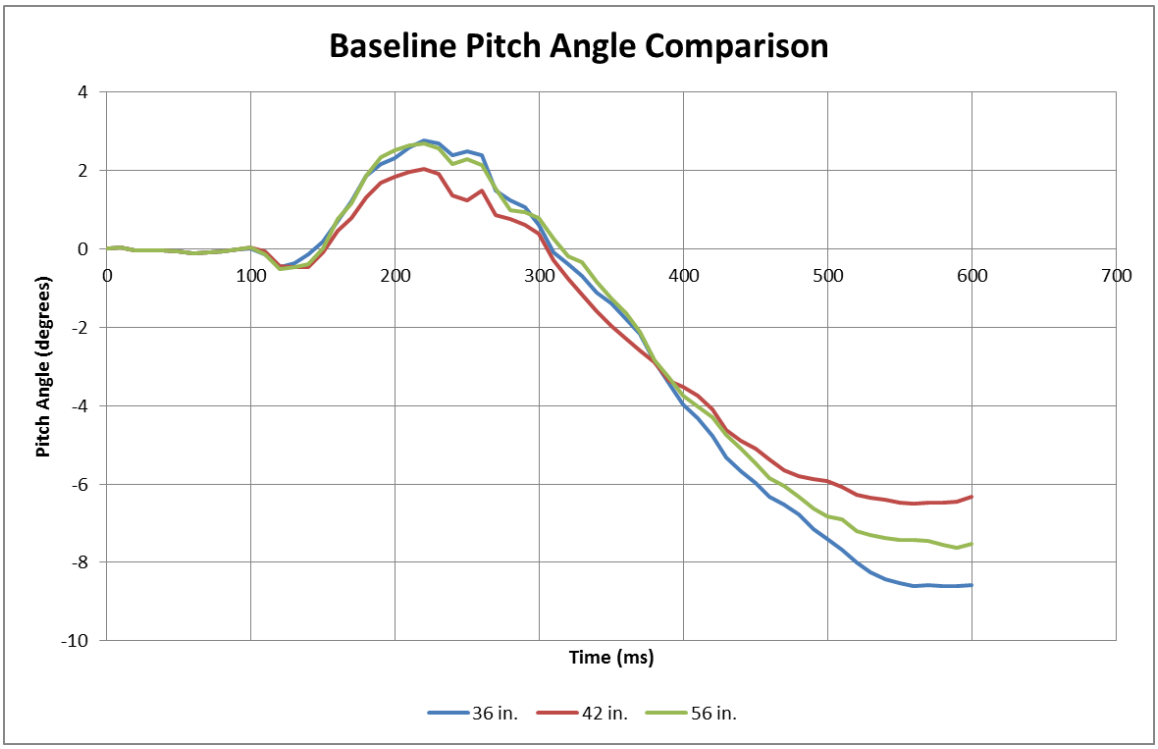

Figure 55. Baseline Simulation Vehicle Pitch Angles

7.1.6 Suspension Damage

From the full-scale test review conducted in Section 3.5, the steering link disengages from the vehicle under relatively small impact loads. The total force transmitted through the steering link in the simulation was plotted in Figure 56. The steering link transmitted nearly 20 kips (90 kN) after the vehicle impacted the barrier. Comparatively, the maximum loads transmitted through the lower and upper control arms were approximately 20 kips (90 kN) and 11 kips (50 kN), respectively. From full-scale testing damage, the steering link would be expected to disengage at a significantly lower load than the failure loads of the lower and upper control arms.

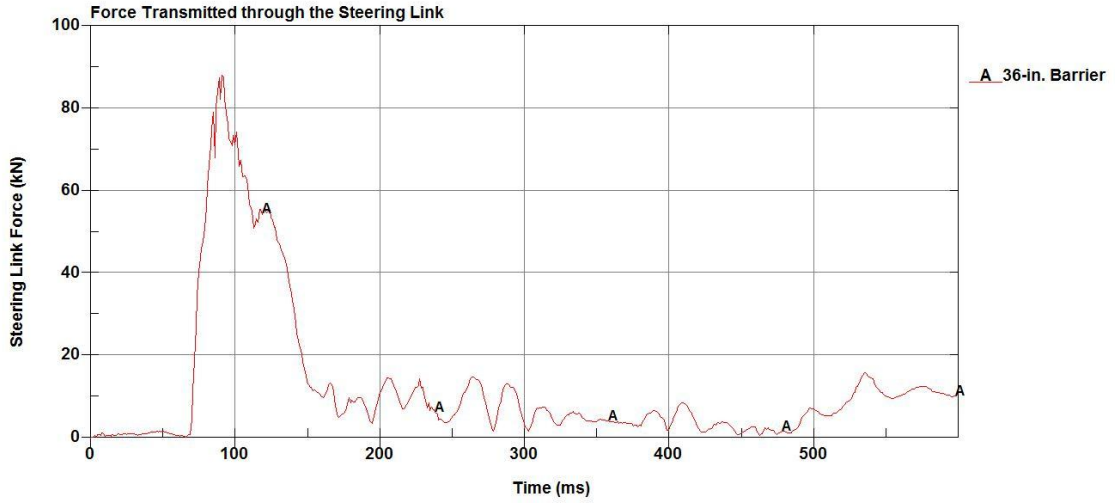

Figure 56. Force Transmitted Through the Steering Link

The lower control arm experienced some damage during the simulation, while the upper control arm remained relatively undamaged. Damage to the simulated suspension is shown in Figure 57. Comparing this damage to the full-scale damage seen in Figure 9, the Silverado suspension damage and the Dodge Ram suspension damage are similar in nature, and this extent of damage could be expected in a full-scale crash test.

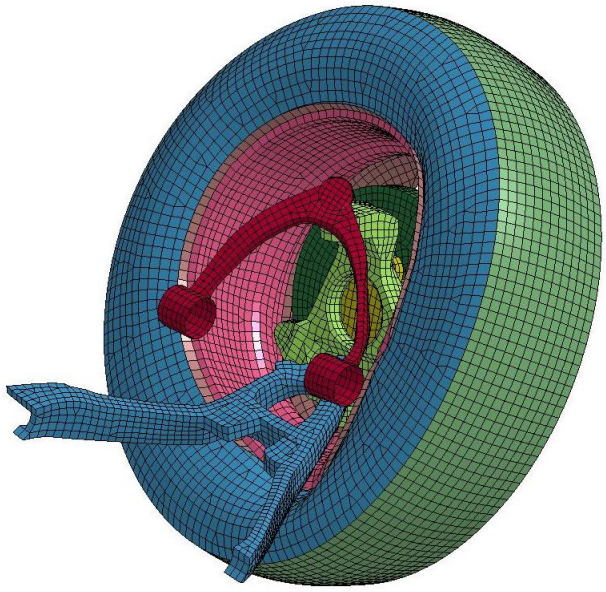

Figure 57. Suspension Damage for the Model with Tire Deflation

7.1.7 Zone of Intrusion Results

Images of the maximum ZOI during the impact stage and during the tailslap stage are shown in Figure 58.

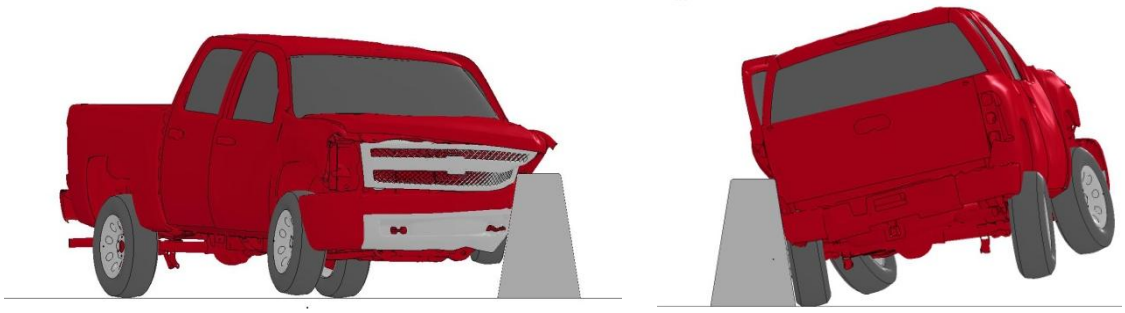

36 in. (914 mm)

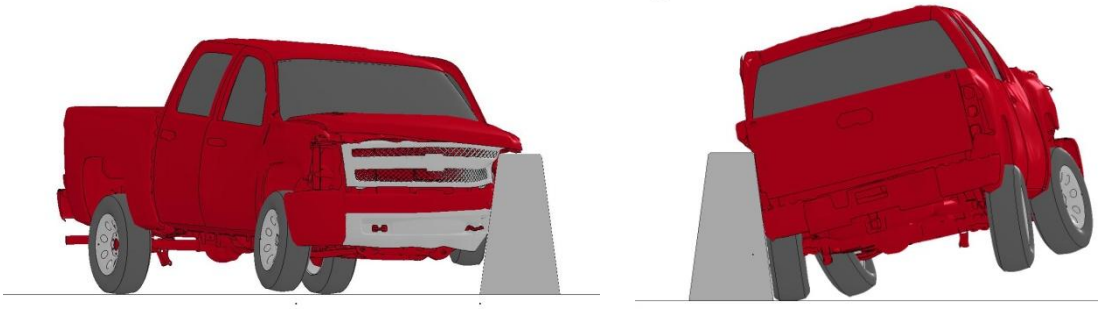

42 in. (1,067 mm)

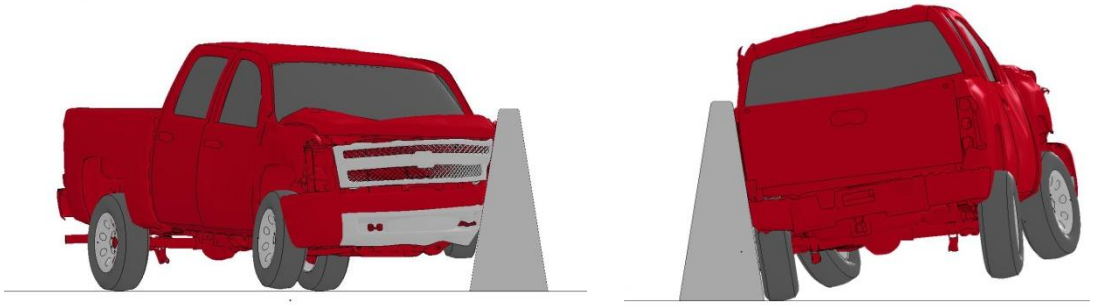

56 in. (1,422 mm)

Figure 58. Baseline Maximum ZOI Positions

The procedure for identifying the zone of intrusion points was given in Section 5.8. ZOI measurements were taken for the baseline simulation for each of the heights of

single-slope barrier. Initial measurements showed that the ZOI was larger for shorter barriers, which was expected. ZOI results from the baseline simulation are shown in Table 11. Shorter barriers allow the vehicle to experience higher roll angles. Also, for shorter barriers, the redirective force acting on the vehicle occurs at a lower position on the vehicle, which creates a longer moment arm and allows more deflection at the top of the vehicle. Simulation results showed that there was no protrusion over and behind the 56-in. (1,422-mm) tall barrier. This occurred because the tire deflation softened the impact between the tire and the barrier, which slightly reduced the yaw moment of the vehicle and lowered the severity of the impact during the tailslap phase.

Table 11. ZOI Comparison for the Baseline 9.1-degree Single-Slope Simulation Model

Barrier Height	Zone of Intrusion – in. [mm]			
	Front Fender	Corner of Hood	Rear Corner of Box	Edge of Door
36 in. (914 mm)	11.5 (293)	8.4 (214)	8.5 (216)	9.4 (240)
42 in. (1,067 mm)	6.3 (160)	5.9 (151)	4.3 (110)	3.4 (85)
56 in. (1,422 mm)	NA	NA	NA	NA
36-in. (914-mm) tall Texas 10.8-degree single slope barrier simulation	11.2 [285]	8.2 [207]	7.9 [199]	6.9 [175]

ZOI results from the 36-in. (914-mm) tall, Texas 10.8-degree single-slope barrier are also shown in Table 11. ZOI values were lower for the 10.8-degree barrier than the 9.1-degree barrier at every location. From the literature review [3], vertical barriers imparted the largest lateral loads on the vehicle, resulting in the highest lateral accelerations and the largest moment exerted on the vehicle. Similarly, the steeper single-

slope barriers show that they encounter higher protrusions from higher lateral impact accelerations. Thus, the 9.1-degree barrier would be expected to have higher ZOI values than the 10.8-degree barrier.

As stated in Section 5.8.6, it was assumed that an impact with the front fender would not pose a significant risk to the occupants of the vehicle. Thus, the ZOI from the baseline model would be determined from the other three ZOI points. For the 36-in. (914-mm) barrier, the edge of the door protruded 9.4 in. (240 mm) behind the top-front edge of the barrier, which was larger than the hood protrusion behind the barrier. For both the 42-in. and 56-in. (1,067-mm and 1,422-mm) tall single-slope barriers, the hood protruded the farthest behind the barrier.

7.2 Simulation with Tire Deflation

In Section 3.4, one full-scale crash test indicated that the impacting tire ruptured when the sidewall was pinched between the rim and the toe of the concrete barrier. The impacting tire pressure for the baseline simulation was plotted for the three barrier heights, and the results are shown in Figure 59. All three simulations agreed that the peak tire pressure only increased by about 2.2 psi (15 kPa). As noted in reviews of 2270P vehicle crash tests, the vehicle tire ruptured during each rigid or restrained-motion concrete barrier test. Based on the damage seen on the tire, it is believed that tire pressure is not the primary cause of tire deflation during a full-scale impact event.

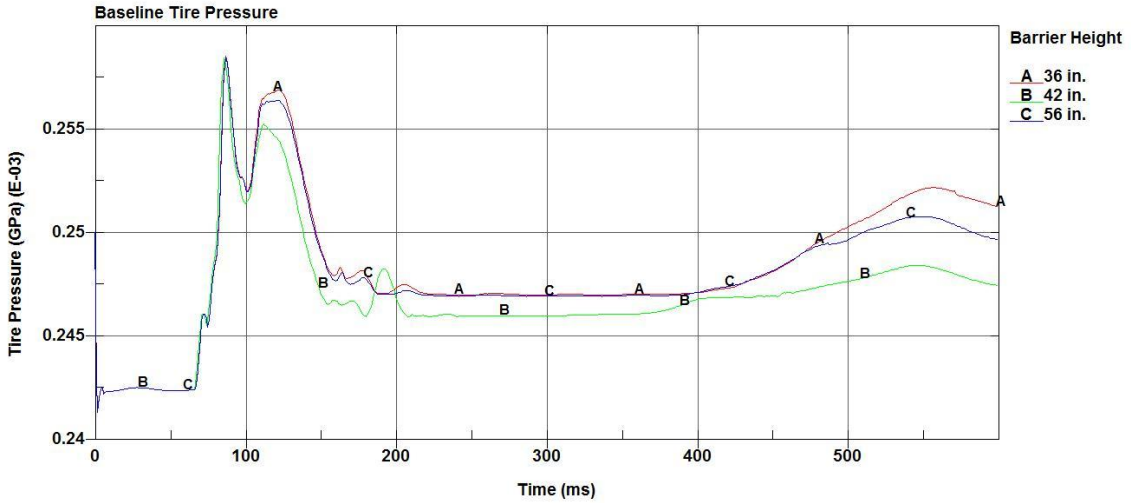

Figure 59. Baseline 9.1-degree Single-Slope Barrier Simulation Tire Pressure

The tire in the Silverado model is simulated as an airbag. Pressure on the sidewalls helps the tire maintain its rigidity. To simulate tire deflation, the pressure inside of the tire was brought to zero over 5 ms. Full-scale crash testing was reviewed to determine the deflation time for the impacting tire. It was determined that the tire deflated at approximately 22 ms after impact, or 82 ms into the simulation.

7.2.1 Simulation Results

The maximum protrusions behind the barrier during the impact and tailslap phases of the tire deflation simulations are shown in Figure 60.

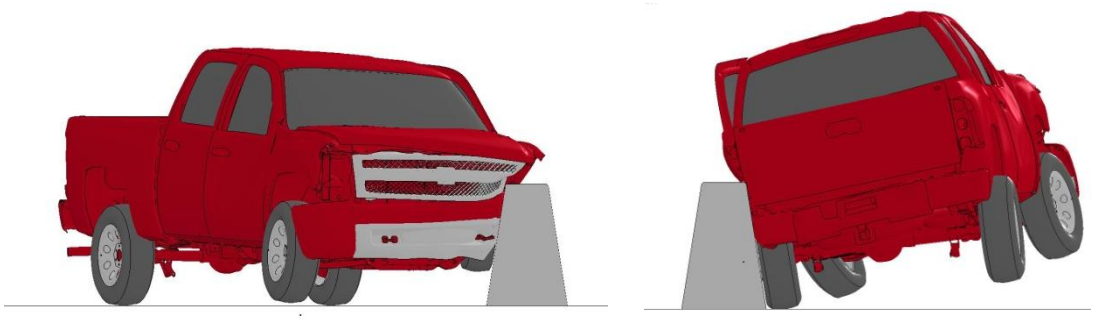

36 in. (914 mm)

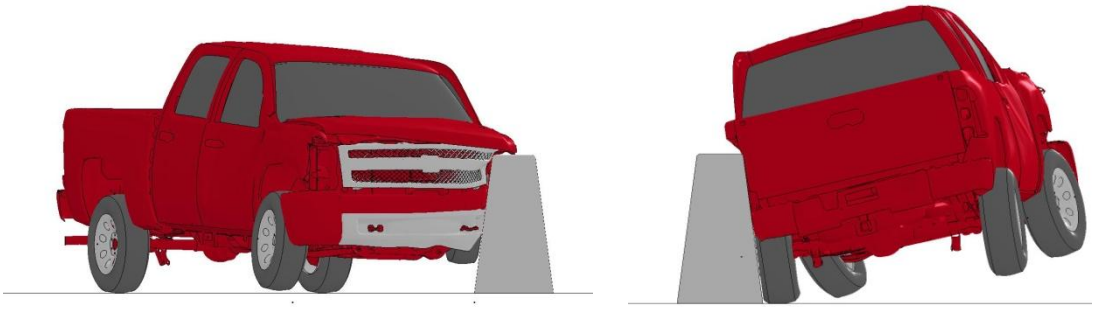

42 in. (1,067 mm)

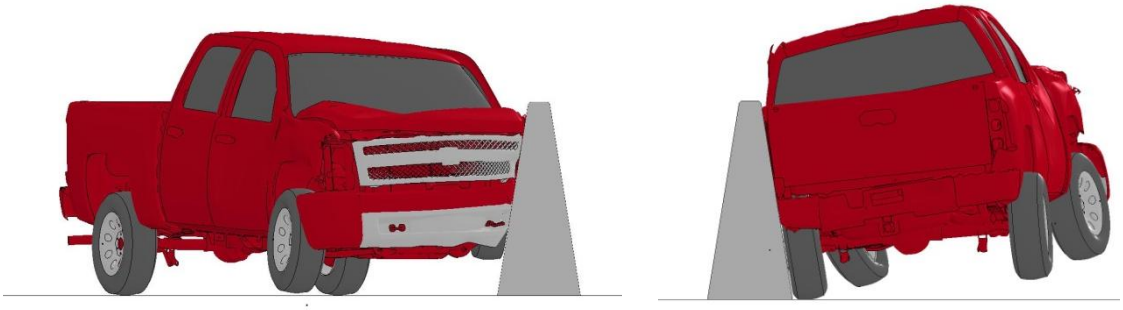

56 in. (1,422 mm)

Figure 60. Maximum ZOI Positions for the Tire Deflation Model

7.2.2 Vehicle Trajectory

The c.g. height of the vehicle is shown in Figure 61. With the simulated tire deflation, the vehicle c.g. did not climb up the barrier as high. However, the decreased c.g. height corresponded with higher roll angles toward the barrier, as shown in Figure

62. The yaw and pitch angles for the model with tire deflation were similar to the angular deflections seen in the baseline model.

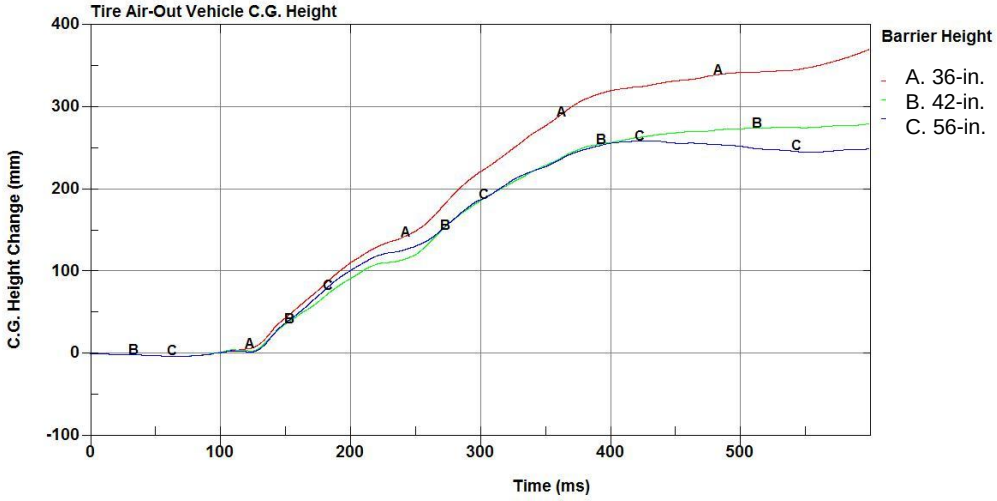

Figure 61. Tire Deflation Simulation Vehicle C.G. Height

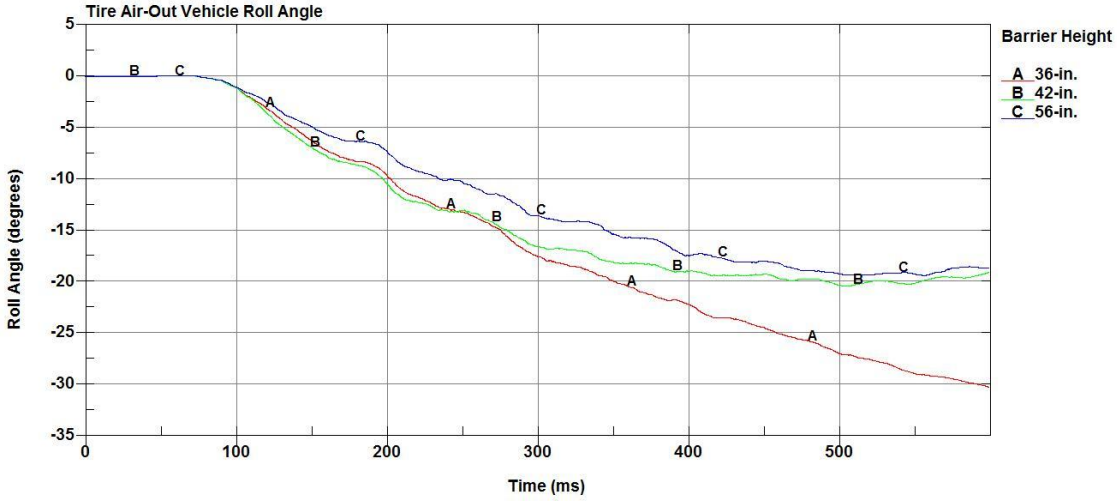

Figure 62. Tire Deflation Simulation Vehicle Roll Angle

7.2.3 Zone of Intrusion Analysis

The ZOI for tire deflation simulations are shown in Table 12. Tire deflation did not significantly increase the ZOI values from the values recorded in Table 11 for the baseline simulations. The fender, hood, and rear corner of the box protruded marginally more for the 36-in. and 42-in. (914-mm and 2,067-mm) tall barriers, while the edge of the

door showed lower ZOI values than those seen in the baseline simulations. Once again, the 56-in. (1,422-mm) tall barrier did not show any protrusion behind the barrier.

Table 12. ZOI Results for the Model with Tire Deflation

Barrier Height	Zone of Intrusion – in. (mm)			
	Front Fender	Corner of Hood	Rear Corner of Box	Edge of Door
36 in. (914 mm)	11.6 (295)	8.5 (216)	8.5 (215)	8.8 (223)
42 in. (1,067 mm)	6.3 (160)	6.1 (155)	4.4 (112)	3.0 (77)
56 in. (1,422 mm)	NA	NA	NA	NA

7.2.4 Tire Deflation Recommendation

Between the baseline simulation model and the tire deflation model, the major difference in ZOI values was seen at the edge of the door, which was the maximum ZOI point for the 36-in. (914-mm) tall barrier simulation. For the joint suspension models, it was recommended that tire deflation be included to model a realistic impact. However, it is unknown whether the method of simulating tire deflation accurately depicts real tire deflation.

7.3 Suspension Joint Failure Models

Three joints connect the wheel to the vehicle – the upper control arm, the lower control arm, and the steering link. All three joints must fail in order for the wheel to detach from the vehicle. Suspension failure times were determined from analyzing full-scale test results and reviewing the forces transmitted through each joint in the wheel from the simulations.

Based on what was reviewed from full-scale crash testing, it was expected that the vehicle would encounter full suspension failure or failure of the lower control arm and steering link. Other suspension failure modes were analyzed to determine the most critical suspension failure mode. Tire deflation was modeled for each of the models incorporating suspension joint failure. This would also create a more severe impact with the barrier, since simulation testing with tire deflation showed a larger ZOI than the baseline model.

The vehicle positions at the maximum ZOI during the impact and tailslap phases for each of the suspension failure test are shown in Figures 63 through 65.

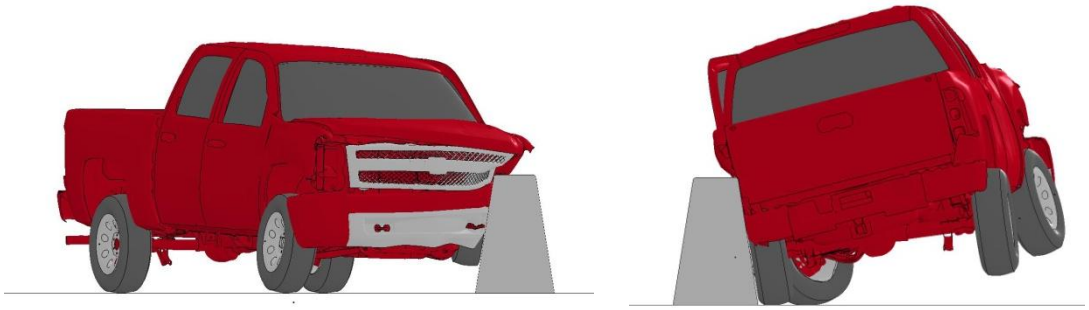

36 in. (912 mm)

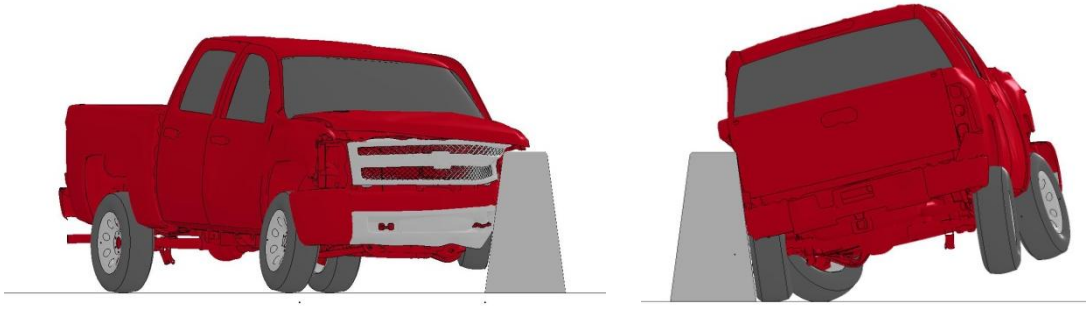

42 in. (1,067 mm)

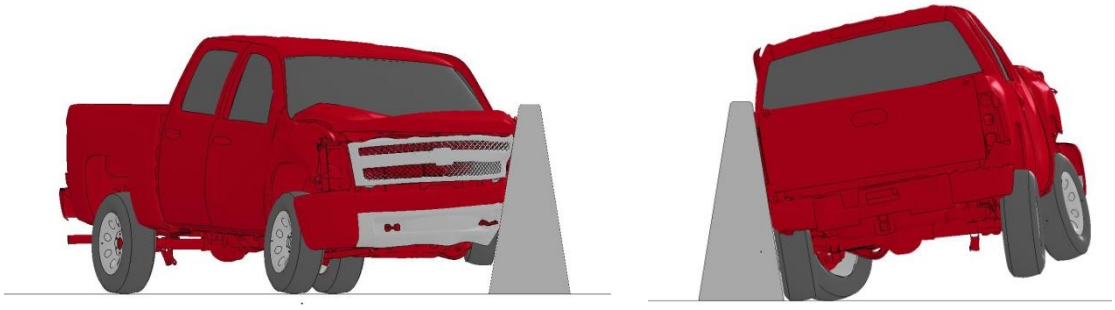

56 in. (1,422 mm)

Figure 63. Maximum ZOI Positions for the Full Suspension Failure Simulation

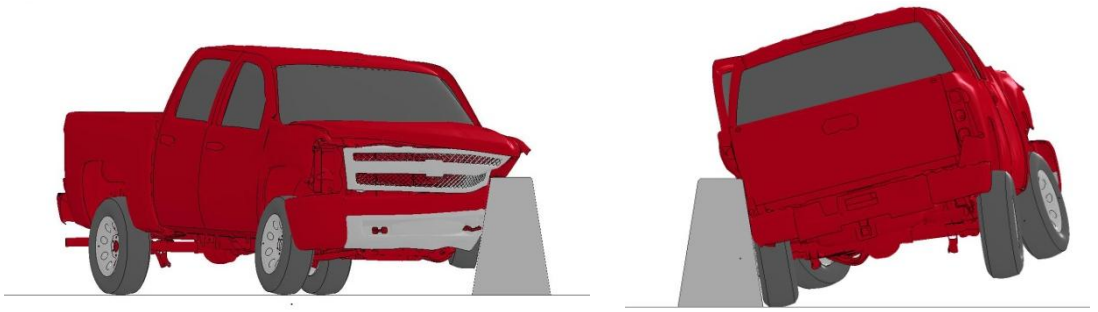

36 in. (912 mm)

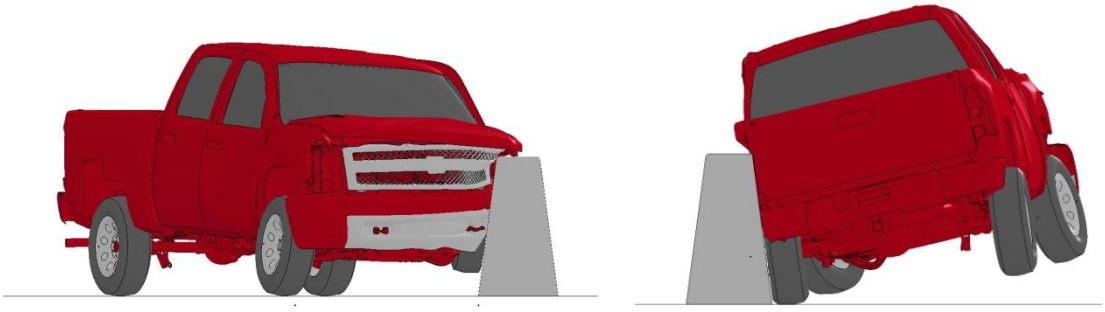

42 in. (1,067 mm)

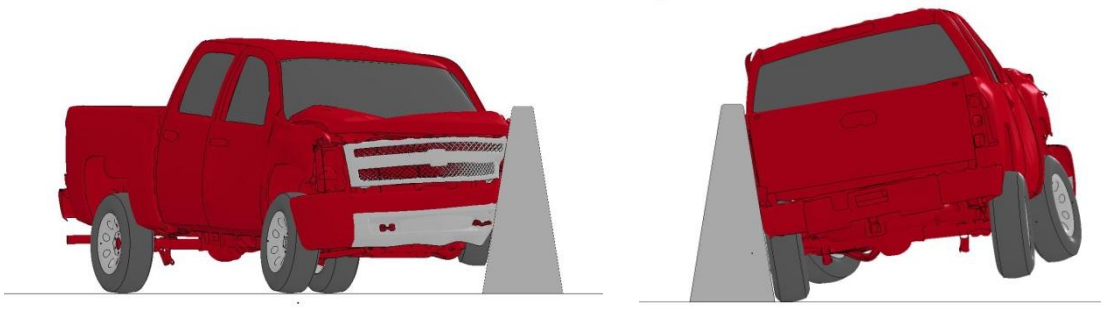

56 in. (1,422 mm)

Figure 64. Maximum ZOI Positions for the Model with Lower Control Arm and Steering Link Failures

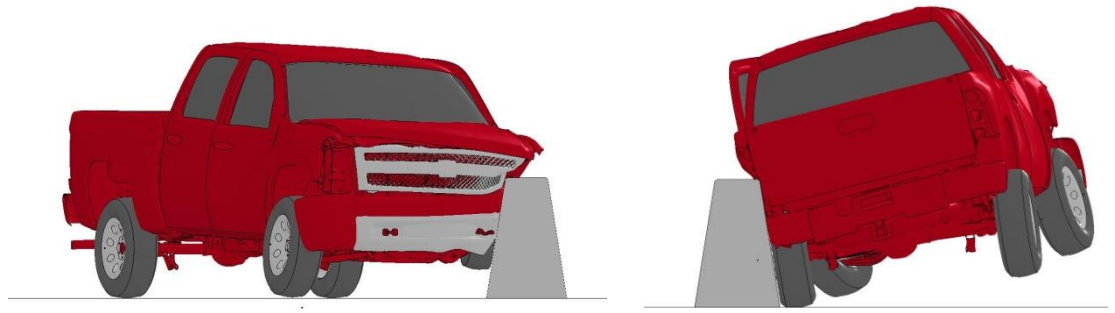

36 in. (912 mm)

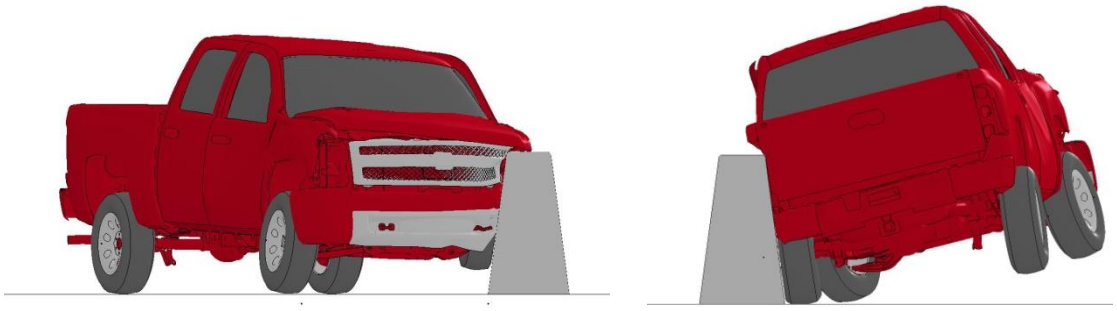

42 in. (1,067 mm)

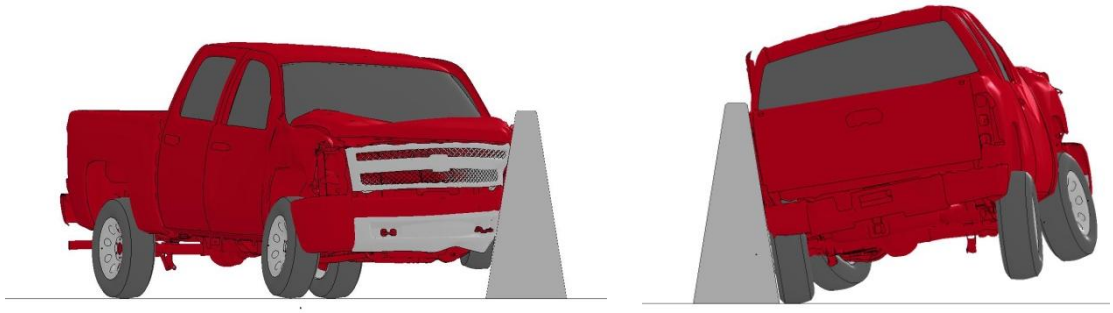

56 in. (1,422 mm)

Figure 65. Maximum ZOI Positions for the Model with Lower Control Arm Failure

Vehicle trajectories from the suspension failure models were similar to those seen in the baseline model. However, for each model incorporating joint failure, the damage to the suspension was notably larger than the damage shown in Figure 57. For example, for the model where the tire disengaged from the vehicle (i.e. all three wheel joints failed), the lower control arm and upper control arm encountered significant plastic deformation, as shown in Figure 66. These deformations are notably larger than those seen in the full-scale crash test into an F-shape barrier, shown in Figure 9. However, the effects of the geometrical differences between the Dodge Ram suspension and the Silverado suspension prevent direct comparison of the damage to the two vehicles.

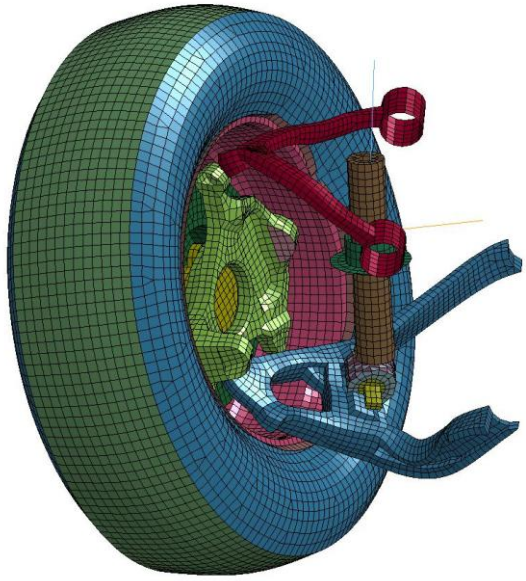

Figure 66. Suspension Damage for the Model with Full Suspension Failure

For the simulations run with suspension component failure, the model utilizing full suspension failure (i.e. all three joints connecting the wheel to the vehicle) experienced the greatest ZOI, as shown in Table 13. With all of the joints failing, the wheel did not provide as large of a redirective force initially, allowing the vehicle to

penetrate slightly farther behind the system during the impact phase. Comparing the joint failure ZOIs to the values obtained in the tire deflation simulations, the rear corner of the box and the edge of the door did not protrude as far in the suspension failure tests.

Table 13. ZOI Values for Tire Suspension Failure Models

Barrier Height	Zone of Intrusion – in. (mm)			
	Front Fender	Corner of Hood	Rear Corner of Box	Edge of Door
Full Suspension Failure				
36 in. (914 mm)	12.2 (310)	9.0 (228)	8.2 (207)	8.5 (216)
42 in. (1,067 mm)	6.4 (162)	6.5 (165)	4.5 (113)	2.7 (67)
56 in. (1,422 mm)	NA	NA	NA	NA
Lower Control Arm Failure Only				
36 in. (914 mm)	11.6 (295)	8.5 (217)	8.4 (213)	8.6 (217)
42 in. (1,067 mm)	6.3 (161)	6.1 (156)	4.7 (121)	3.3 (83)
56 in. (1,422 mm)	NA	NA	NA	0.4 (11)
Steering Link and Lower Control Arm Failure				
36 in. (914 mm)	12.2 (310)	8.9 (226)	8.1 (207)	8.6 (217)
42 in. (1,067 mm)	6.4 (162)	6.4 (163)	4.2 (108)	2.3 (58)
56 in. (1,422 mm)	NA	NA	NA	NA

For the models that did not include failure of the steering link, forces transmitted through the steering joint exceeded the forces noted in Figure 56 and were significantly higher than the force transmitted through any other joint. For this reason, it is believed that those models provided an inaccurate depiction of the impact scenario.

Only one of the models experienced protrusion above the 56-in. (1,422-mm) tall barrier, and this occurred only when the lower control arm failure was modeled. All of the other models showed that the ZOI was zero for each impact. However, the force transmitted through the steering link was excessively large in that model and is believed to have caused the protrusion.

7.4 Zone of Intrusion for Wisconsin 9.1-Degree Single-Slope Barriers

The maximum ZOI was taken from Tables 11 through 13. As stated in Section 5.8.6, a longitudinal impact with the fender behind the barrier is assumed to not pose a risk to the vehicle occupants. The maximum protrusion of the other three ZOI points is shown in Table 14. The maximum fender protrusion was also shown in Table 14.

Table 14. Zone of Intrusion of the Rigid Wisconsin 9.1-degree Single-Slope Barrier

Barrier Height in. (mm)	Fender ZOI in. (mm)	Hood ZOI in. (mm)	Rear Corner of Box ZOI in. (mm)	Edge of Door in. (mm)
36 (914)	12.2 (310)	9.4 (240)	8.5 (215)	9.4 (240)
42 (1,067)	6.4 (162)	6.5 (165)	4.5 (113)	3.4 (85)
56 (1,422)	0 (0)	0 (0)	0 (0)	0 (0)

7.5 Working Width Analysis

Working width is measured from the frontmost point on the barrier to the rearmost point on the system or vehicle during an impact. The working width depends on the vehicle protrusion behind the barrier, the barrier deflection, and the width of the barrier. For rigid, unmoving systems (such as permanent concrete barrier systems), the working width is measured as the largest of two values:

- (Maximum Zone of Intrusion)+(Distance from Top Front Corner to Front Corner of Barrier)
- Maximum Width of Barrier

For temporary, non-rigid barrier systems, the working width may also be:

- (Maximum Barrier Deflection)+(Width of Barrier at Point of Maximum Deflection)

Note that the temporary barriers rotate during impact, and the top back corner of the barrier may protrude further back than the toe of the barrier.

For these barriers, the full barrier width was 24 in. (610 mm). The L value for each of the barriers is given in Table 15. The working width measurements used during these simulations is shown in During each of the simulations, the vehicle did not protrude beyond the back edge of the barrier, so the working width in each simulation was the width of the barrier.

Table 15. Working Width for the Rigid Wisconsin 9.1-degree Single-Slope Barrier

Barrier Height in. (mm)	Distance from Frontmost Point on the Barrier to the Top Front Corner in. (mm)	Maximum Working Width in. (mm)	Maximum Working Width in. (mm)
36 (914)	5.75 (146)	12.2 (310)	24.0 (610)
42 (1,067)	6.75 (171)	6.5 (165)	24.0 (610)
56 (1,422)	9 (229)	0 (0)	24.0 (610)

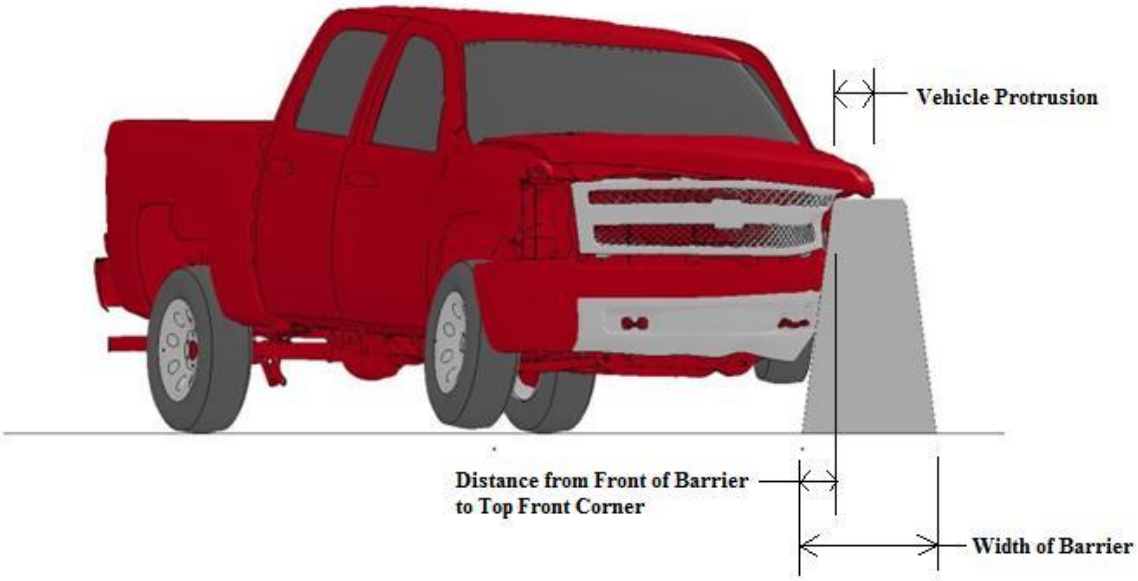

Figure 67. Working Width Measurements

8 SIMULATED OCCUPANT RESEARCH

The automotive industry has been successfully modeling dummies in vehicles for many years. Unfortunately, details of such models are not available due to proprietary reasons. Simulating dummies in roadside safety applications has been rare. Work presented herein is a first attempt at such modeling. These techniques are complicated and will need significant research before results could be considered realistic.

8.1 Introduction

Instrumented and non-instrumented dummy occupants have been used in crash testing for decades. However, following a study conducted by TTI in the 1980's, instrumented dummies were not recommended for use in full-scale crash-testing, and have not been extensively used since [31]. Since the implementation of NCHRP Report No. 350, only non-instrumented dummy occupants have been utilized in concrete barrier testing. However, not all testing agencies utilize dummy occupants in their tests, and MwRSF has been the only testing agency to place a dummy occupant into a 2270P vehicle when impacting a rigid concrete barrier system. Simulating a dummy occupant in the 2270P model would allow for further research into occupant interactions with a vehicle's interior during a full-scale crash event.

The automotive industry has been successfully modeling dummies in vehicles for many years. Unfortunately, details of such models are not available due to proprietary reasons. Simulating dummies in roadside safety applications has been rare. Work presented herein is a first attempt at such modeling. These techniques are complicated and will need significant research before results could be considered realistic.

8.2 Simulated Occupant Model Components

8.2.1 Dummy Occupant Model

Several dummy models are available from the Livermore Software Technology Corporation (LSTC) [33]. A 95th percentile male dummy model was chosen for this study, as shown in Figure 68. The larger male dummy represents one of the largest and heaviest human dummies available with the highest inertia; thus, the 95th percentile male dummy would have the greatest effect on the vehicle motion. A more detailed 95th percentile male dummy model was also available. However, it was believed that the general dummy motion and its effect on the vehicle trajectory for an initial study would be served best by using the simplified, reduced model.

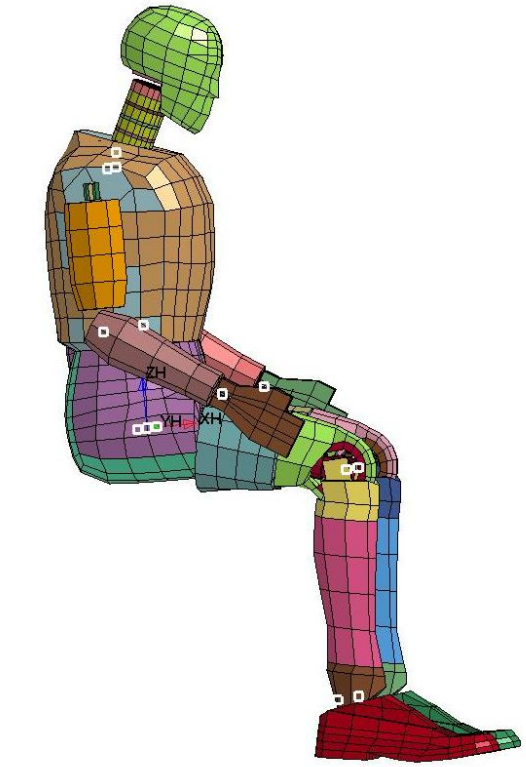

Figure 68. Simulated Occupant Model

8.2.2 Seat Model

The front seats in a 2007 Silverado pickup truck are bucket seats, and the optimal simulation would include similar seat geometry. Developing a new seat model would be costly and take a lot of time, and the seat model was outside of the scope of this research. Bucket seats were developed and implemented into the 2008 Toyota Yaris model [34]. The seat from the Yaris model was isolated and used for these simulations, and is shown in Figure 69.

Figure 69. Bucket Seat Model

8.2.3 Seatbelt Model

A retracting seatbelt model was provided in a tutorial from LSTC. The model included meshed fabric seatbelt elements that were in contact with the occupant and thin, 1-dimensional beam elements to simulate the rest of the seatbelt, as shown in Figure 70.

The retracting seatbelt model was configured to draw tight against the occupant as the simulation started. Sensors in the seatbelt were set to detect a threshold acceleration and lock the retractor to prevent the seatbelt from spooling out.

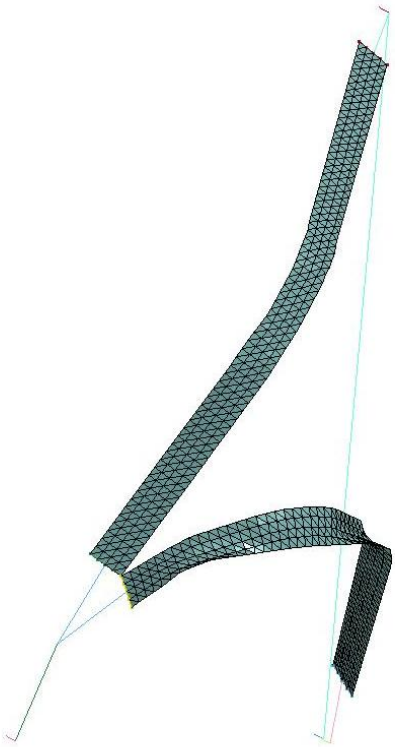

Figure 70. Seatbelt Model

8.3 Seat Stability and Acceleration

In order to help verify that the seat model would perform acceptably in the 2270P model, it was set in motion following a trajectory similar to a full-scale crash test. A rigid block was created to simulate the vehicle, and the seat model was rigidly attached to the block, as shown in Figure 71. The block and seat traveled forward at 62.1 mph (100 km/h). After 133 ms, a lateral acceleration was applied to the block, and the simulation was allowed to run for 250 ms. The lateral acceleration curve was similar to the

acceleration trace observed in the simulations with the 9.1-degree single-slope concrete barrier. The acceleration curve is shown in

Figure 71. Seat and Rigid Block Model

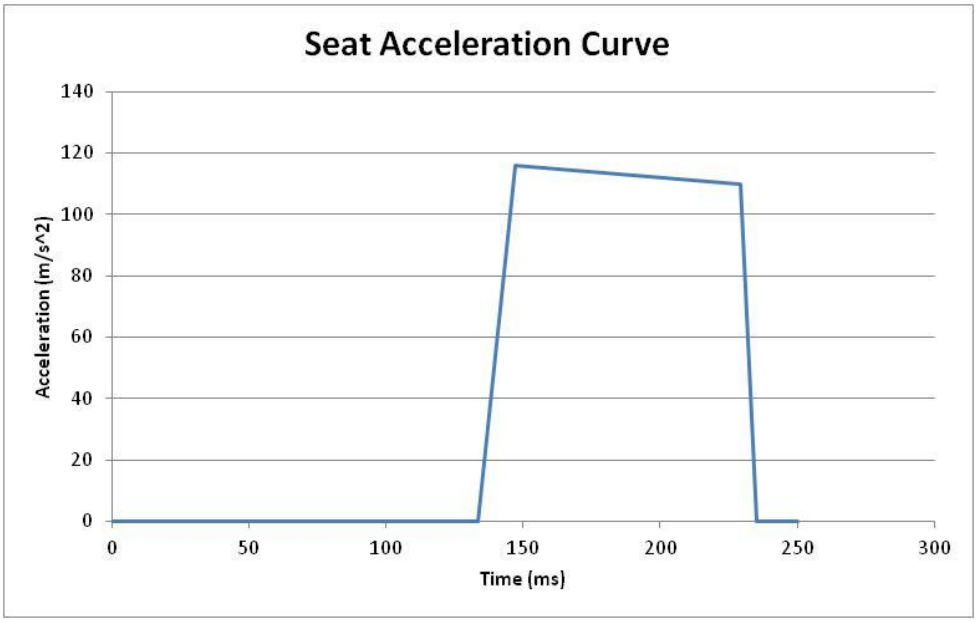

Figure 72. Seat Acceleration Curve

Simulations showed that the seat model was stable, and lateral accelerations did not cause the seat model to fail. The seat did not deform significantly, and the seat was determined acceptable for use in the next phase of simulations.

8.4 Occupant-In-Seat Model

The dummy model was placed into the seat model attached to the rigid block, as shown in Figure 73. The limbs on the dummy were positioned to be similar to the positioning of the dummy's limbs during a full-scale crash test by using the dummy positional tools available in the preprocessing software LS-PrePost. The dummy was moved until it was nearly touching the seat. However, there was a separation between the dummy and the seat, ensuring that there would be no initial penetrations in the contact when the simulation started. The simulated occupant was reclined to match the shape of the seat as well.

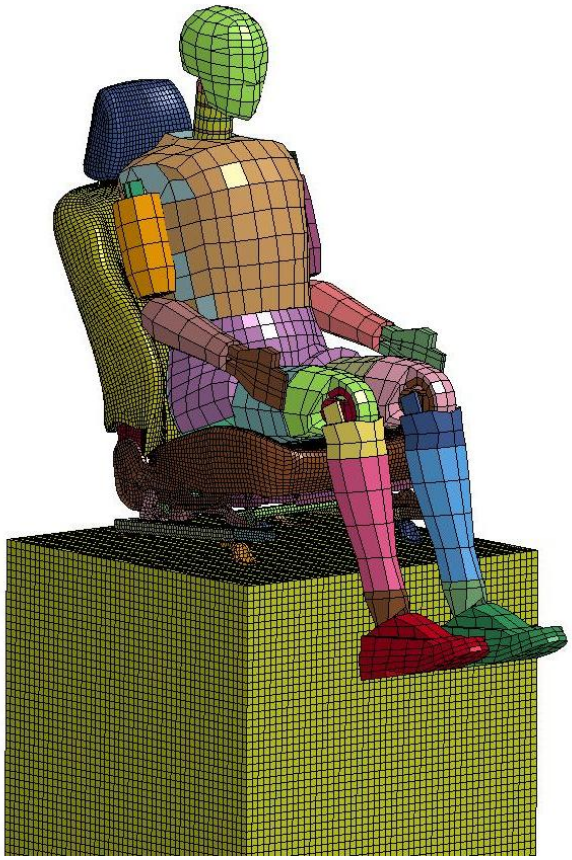

Figure 73. Seat, Rigid Block, and Simulated Occupant Model

After the dummy and seat model showed stability traveling straight forward, a lateral acceleration was applied to the rigid block supporting the seat model. As the seat accelerated, the dummy slid off of the seat, rotating away from the seat, as shown in Figure 74.

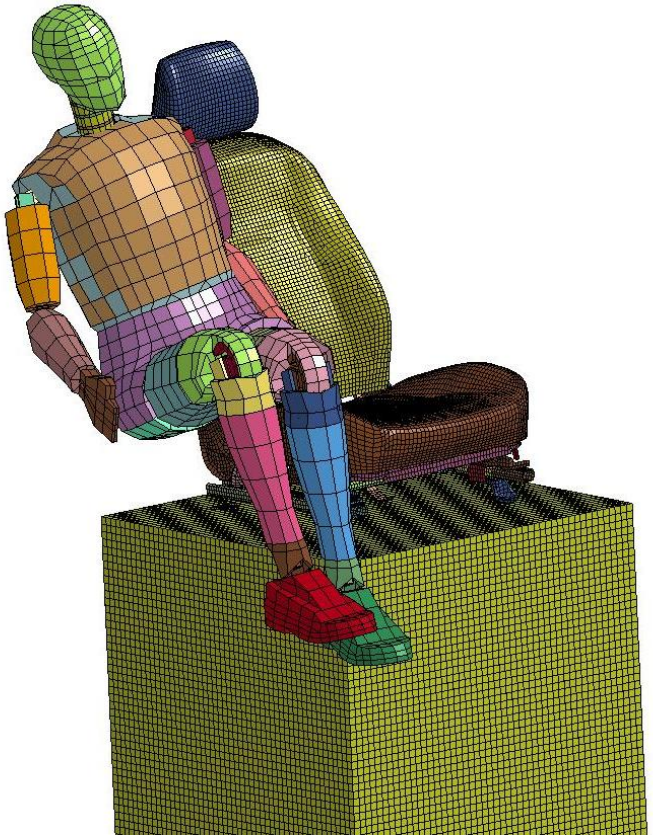

Figure 74. Dummy Sliding Out of Seat

8.4.1 Hourglassing and Element Formulation

Hourglassing is unforced deformations of the material, a mathematical phenomenon that is physically impossible. Hourglassing was noted in the seat bottom as the dummy slid off of the seat. Fully-integrated elements do not experience hourglassing. Thus, the element formulation was switched to the fully-integrated formulation.

Simulation time for the seat and block model nearly doubled using the fully-integrated element formulation in the seat base. Comparisons between the fully-integrated and the default constant-stress solid element formulation showed little difference in the dummy trajectory.

Despite the hourglassing observed in the lower seat, the constant-stress solid element formulation was the most cost-effective and stable material to model the seat foam, and it was used for the remainder of the simulations.

8.5 Seatbelt Stability and Acceleration

The seatbelt model was positioned in front of the dummy model in the seat, and the ends of the seatbelt were rigidly attached to the seat. The seatbelt was not tight against the occupant to prevent the seatbelt elements from intersecting the dummy elements. A simulation was conducted to determine the stability of the seatbelt with the seat, as shown in Figure 75. For this simulation, the dummy was removed.

Figure 75. Seatbelt, Seat, and Rigid Block Model

The seatbelt was modeled using the MAT_FABRIC material, which has a relatively large tensile strength but a small compressive strength, which attempts to simulate minimal bending stiffness of a fabric. As the seatbelt was accelerated laterally, the elements began to buckle, as shown in Figure 76. This did not cause instability in the simulation, and no steps were taken to remove the seatbelt buckling.

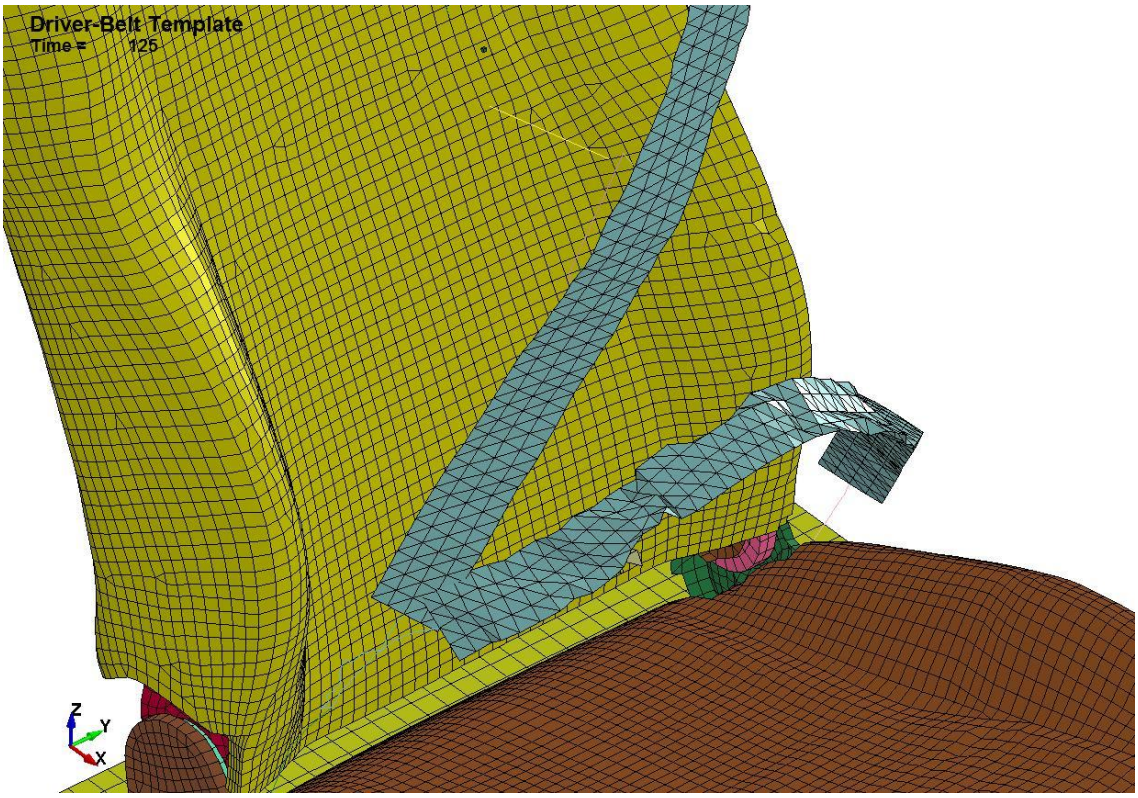

Figure 76. Belt Deformation During Simulation

8.6 Seatbelt and Simulated Occupant

8.6.1 Seatbelt Model with Beam Elements

The dummy occupant was placed in the seat attached to the rigid block, and the seatbelt was placed to restrain the occupant in the seat. As the rigid block accelerated laterally, the dummy slid out of the seat and the seatbelt attempted to prevent the lateral

motion of the occupant. The lap belt stretched and traveled with the dummy and did not restrain the occupant's lateral motion, as shown in Figure 77.

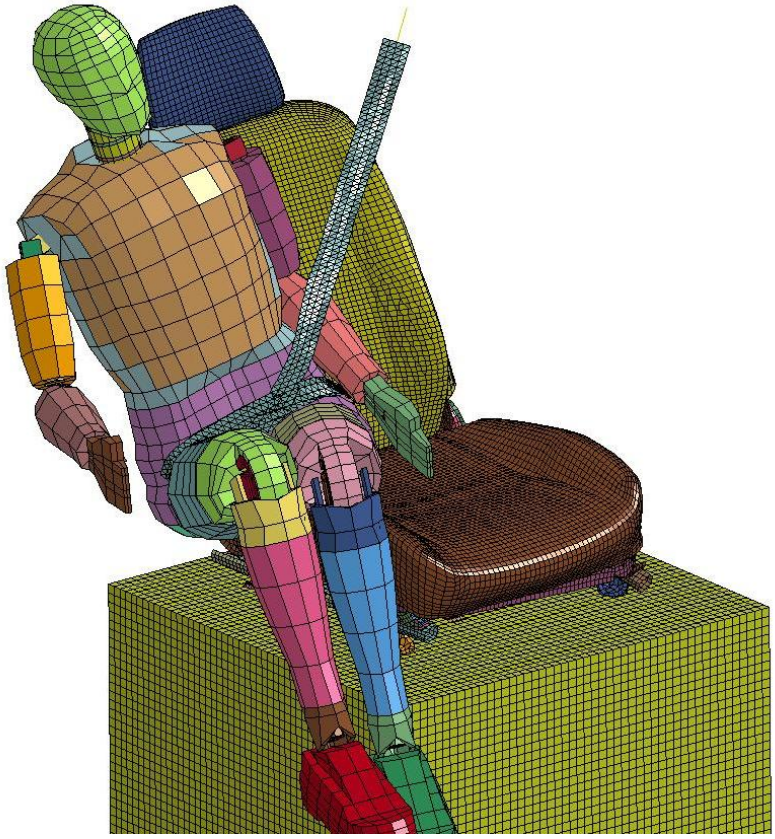

Figure 77. Seatbelt Stretch

8.6.2 Seatbelt Model with Shell Elements Fixed to Seat

To provide increased resistance to the lateral motion of the dummy during the impact, the beam elements were removed from the seatbelt model, and the shell elements on the ends of the seatbelt were rigidly attached to the seat. When this simulation was performed, more realistic results were observed. The 2-dimensional elements deformed, but it did not show unreasonable behavior, as shown in Figure 78. The simulated occupant pushed against the belt, and the belt properly restrained the occupant's motion.

However, it was noted that, for these simulations, the seatbelt did not extend downward far enough, and the occupant was able to slip under them and escape from the seatbelt.

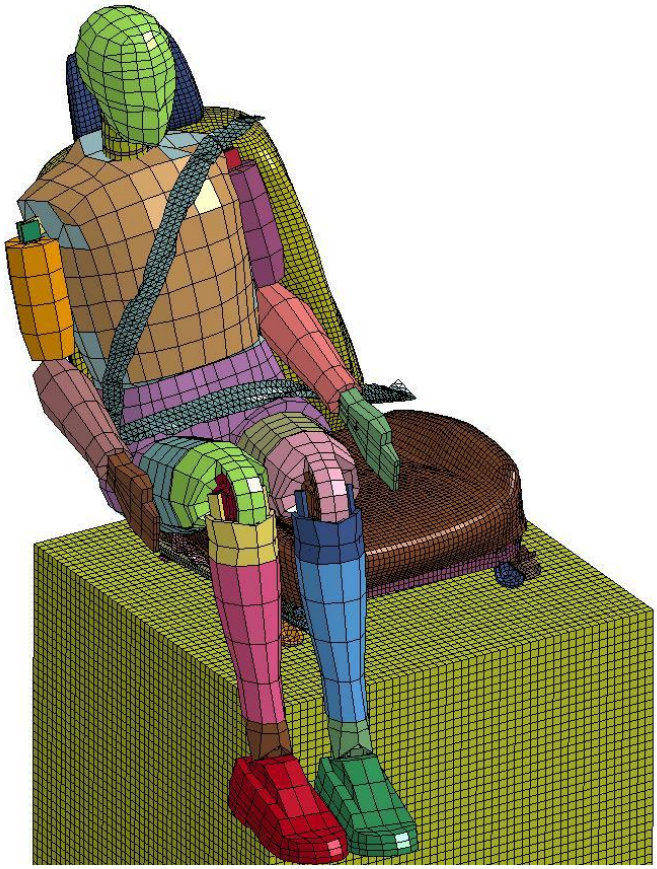

Figure 78. Seat, Seatbelt, and Dummy Accelerated to the Left

The seat and rigid block were accelerated in the other direction, as shown in Figure 79. Since the seatbelt was rigidly attached to the seat, the force from the seatbelt resisting the occupant's movement caused the seat to deform. Also, the lap belt sufficiently restrained the occupant's lateral motion. However, the end of the shoulder strap contacted the neck of the dummy, showing potential to allow the dummy to release underneath it, which is not realistic.

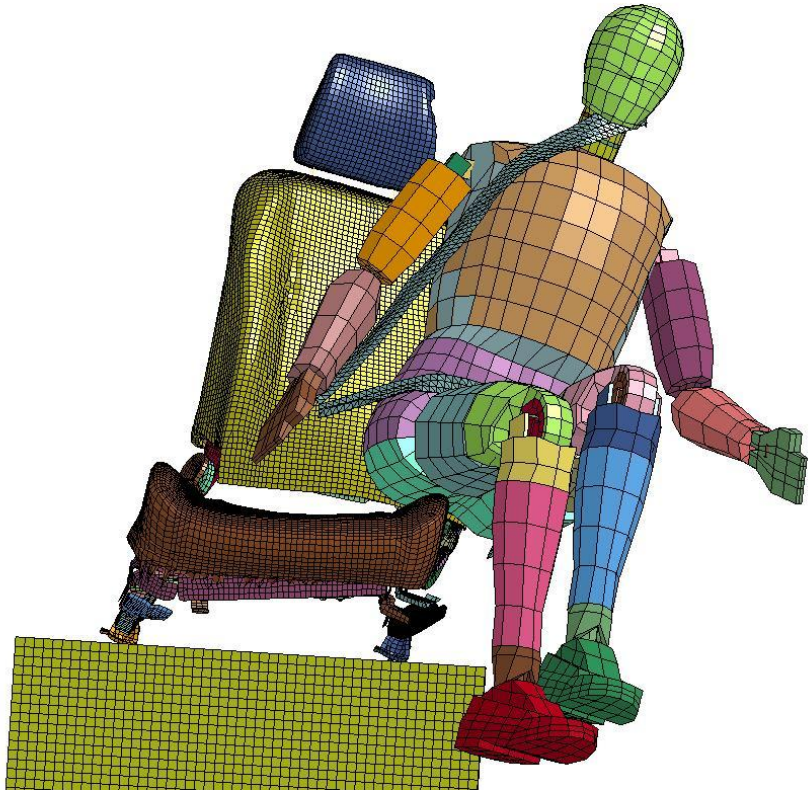

Figure 79. Seat, Seatbelt, and Dummy when Accelerated to the Right

8.7 Implementation into the Vehicle

8.7.1 Model Description

The dummy, seat, and seatbelt model were placed in the 2270P vehicle. The legs of the seat were rigidly attached to the floorboard of the vehicle, the lap seatbelt was rigidly attached to the floorboard of the vehicle on both sides of the seat, and the shoulder seatbelt was rigidly attached to the floorboard and the vehicle's A-pillar.

The 2270P vehicle model with the dummy occupant was simulated impacting into the 36-in. (914-mm) tall, 9.1-degree single-slope concrete barrier. The model was simulated without any suspension component failure or tire deflation.

8.7.2 Simulation Results

Simulation results are shown in Figure 80, and the dummy reaction in the vehicle is shown in Figure 81. The vehicle rolled over during the simulation. A simulation performed without a dummy in the seat showed behavior similar to the baseline simulation behavior in Section 7.1, which shows that the presence of the dummy occupant changes the vehicle trajectory during the simulation.

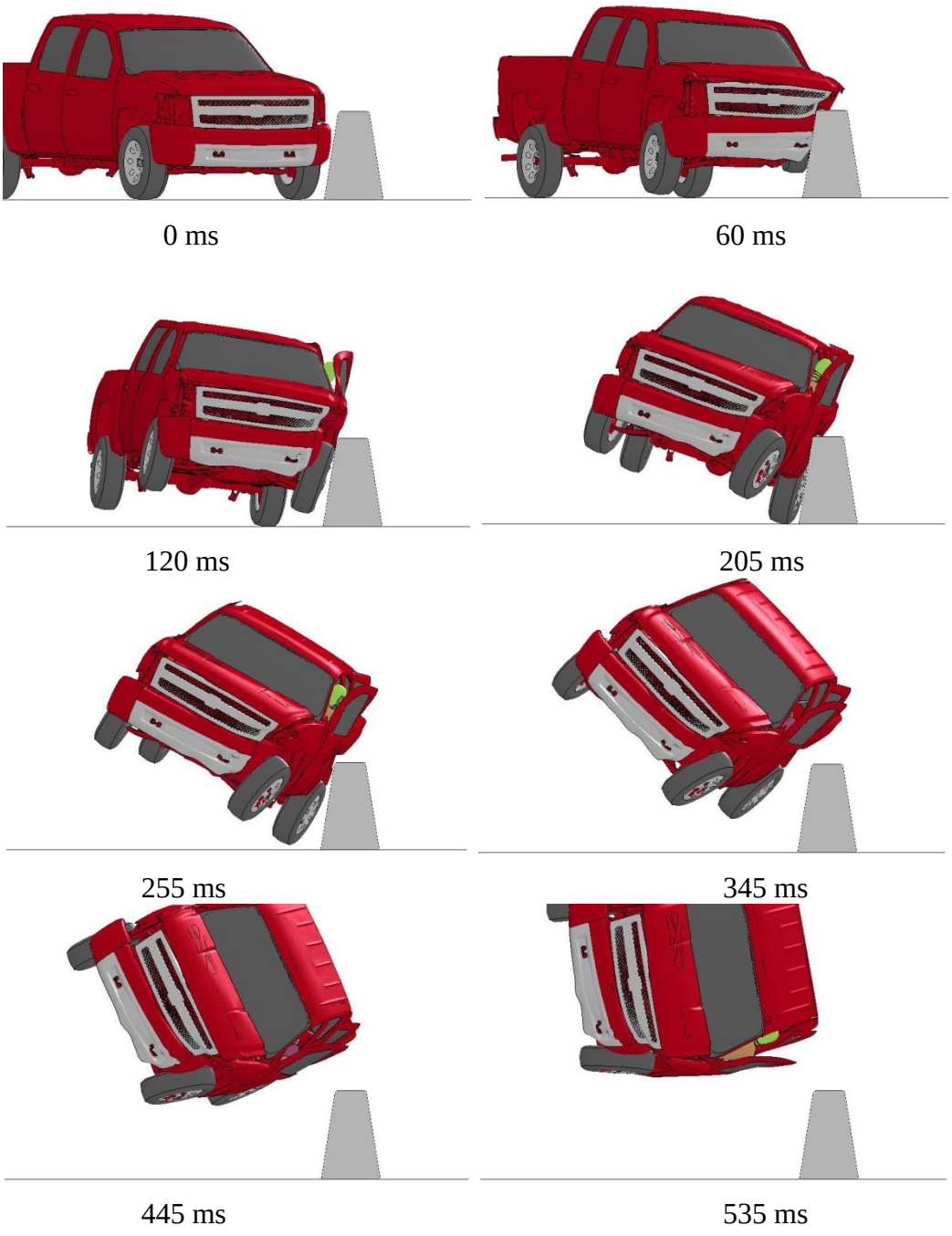

Figure 80. Dummy, Seat, Seatbelt, and Vehicle Simulation

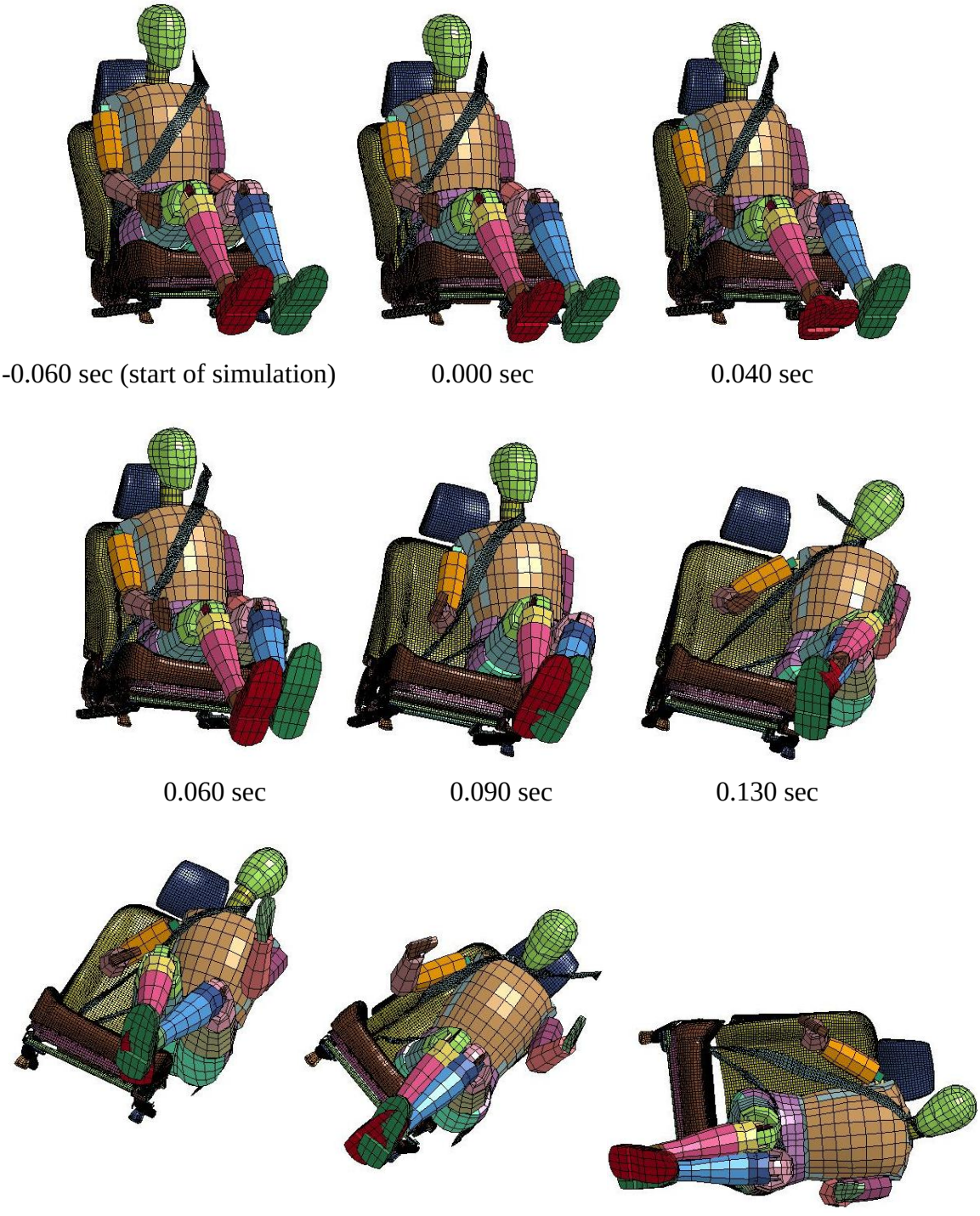

Figure 81. Dummy Reaction in the Vehicle

8.7.3 Head Protrusion Out of Vehicle

As the dummy impacted the door of the vehicle, the top of the impact-side door separated from the vehicle and the dummy occupant's head protruded outside of the vehicle, as shown in Figure 82. The deflection of the top of the door was compared between full-scale tests conducted with and without dummies, as shown in Figure 83. Note that both of these tests utilized restrained-motion barriers. There have not been two similar tests conducted with 2270P vehicles on rigid concrete barrier systems.

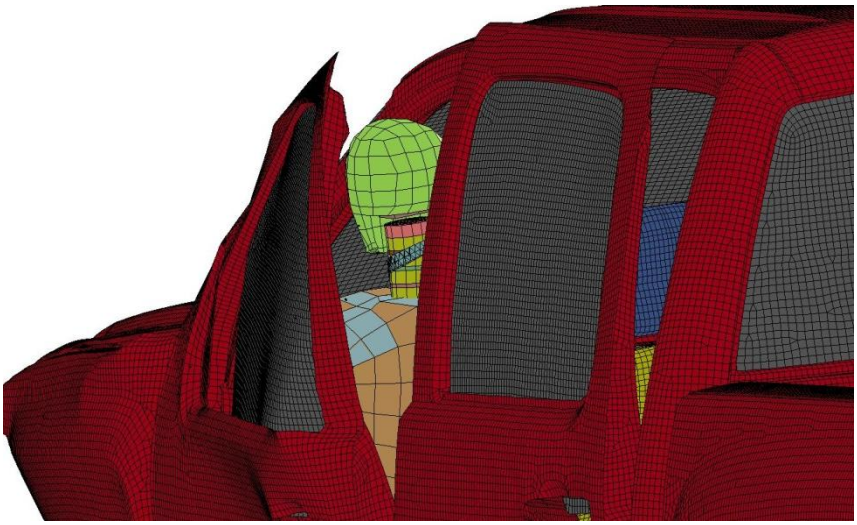

0.110 sec

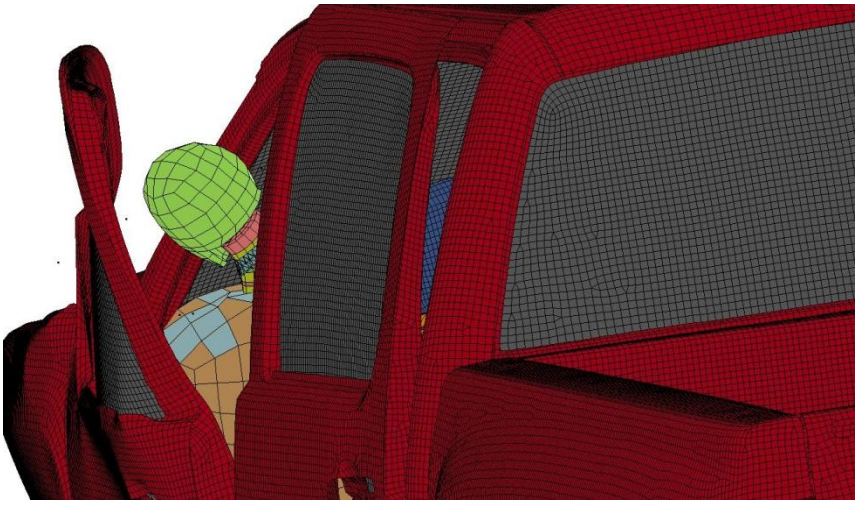

0.140 sec

Figure 82. Head Protrusion Out of the Vehicle

No Dummy Occupant [17]

Dummy Occupant [21]

Figure 83. Door Deflection With and Without Dummy Occupants

The window pane separated from the door in the lower photo in Figure 83. This behavior was not observed in every full-scale test, but the deflection at the top of the door was similar to the deflection from other tests (see Reference 18). This behavior was noted in full-scale crash tests into restrained-motion temporary barrier systems. Vehicle trajectory was similar between rigid and restrained-motion concrete barrier systems. Thus, it is believed that the protrusion of the dummy occupant's head out of the window in the simulation was not realistic in this simulation.

8.7.4 Seatbelt Forces

The seatbelt was initially slack on the occupant, and it did not exert a force on the occupant until approximately 50 ms after impact (110 ms into the simulation), as shown in Figure 84. Note that the impact between the vehicle and the barrier occurred at 60 ms in Figure 84. The lateral force exerted by the seatbelt on the occupant occurred in two peaks. The first peak was caused by the occupant's neck contacting the shoulder belt. The second peak occurred after the occupant's torso exited the chair and the lap belt resisted the lateral motion of the occupant. The occupant's torso contacted the door at approximately 105 ms which was before the seatbelt applied a force on the occupant. It is believed that an actual seatbelt would provide more resistance to the lateral motion of the occupant than what was observed during this simulation.

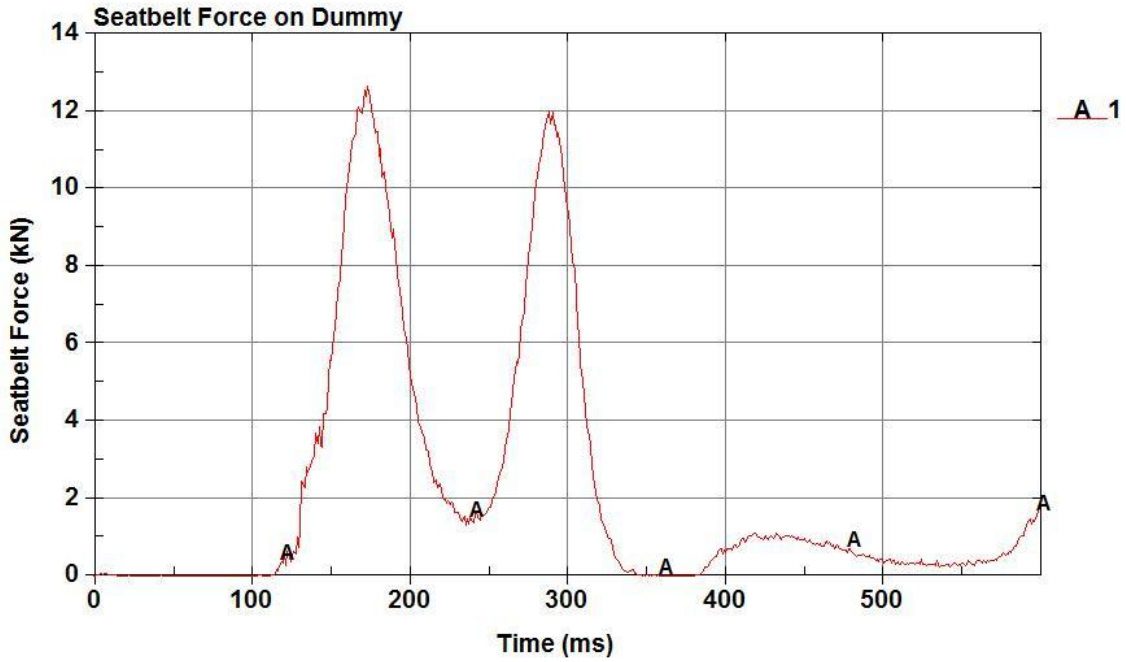

Figure 84. Seatbelt Forces on the Dummy Occupant

8.7.5 Impact Between the Occupant and the Door

The contact forces between the door and the occupant are shown in Figure 85. Impact forces climbed to nearly 3100 lb (14 kN) between the body of the occupant and the door. The maximum force between the head and the window was approximately 900 lb (4 kN). Contact forces between the occupant body and the door decreased as the seatbelt force on the dummy increased.

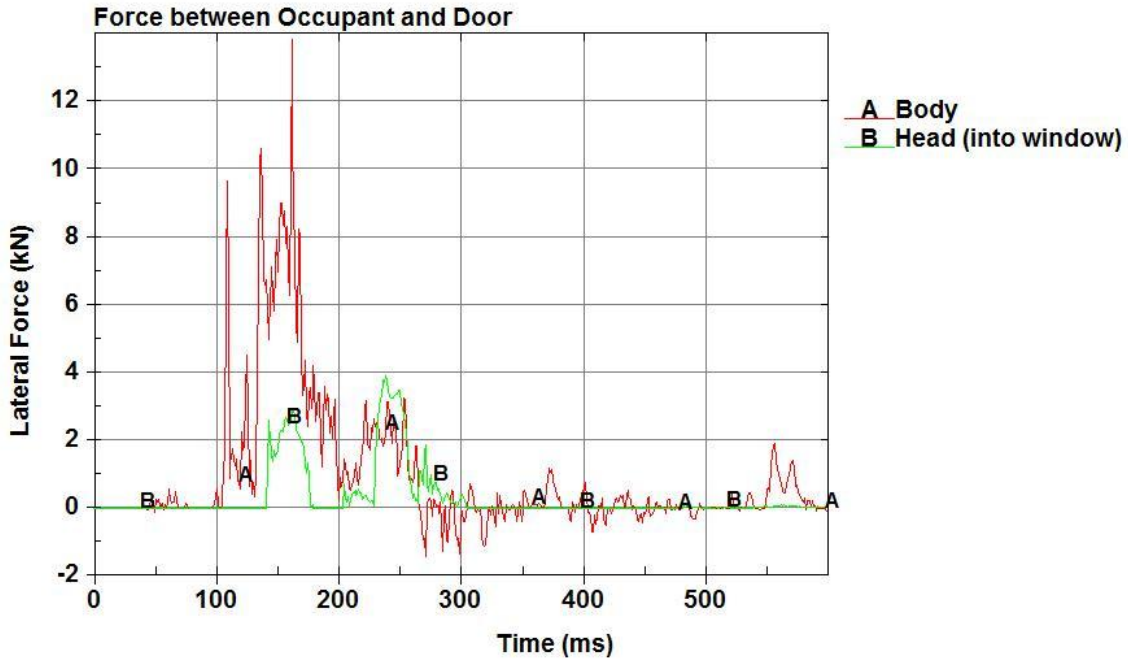

Figure 85. Forces Between the Dummy Occupant and the Door

8.8 Comparison with the Baseline

The dummy-in-vehicle simulation was compared to the baseline 36-in. (914-mm) tall, 9.1-degree single-slope barrier simulation described in Section 7.17.1. The vehicle model, barrier, and impact conditions were the same for both simulations. The only difference between the two was the inclusion of the dummy, seat, and seatbelt model.

8.8.1 Vehicle Vertical C.G. Displacement

The vertical displacement of the vehicle was very similar between the two simulations, as shown in Figure 86. Note that impact in this simulation occurred at 60 ms. The dummy, seat, and seatbelt inclusion did cause the vehicle to travel slightly higher, but as time progressed, the vertical displacement of the vehicles converged. The vertical force between the vehicle and the barrier is shown in Figure 87. There was little

difference in the vertical forces between the two simulations until the tailslap phase, where the vehicle with the occupant had a slightly higher vertical force.

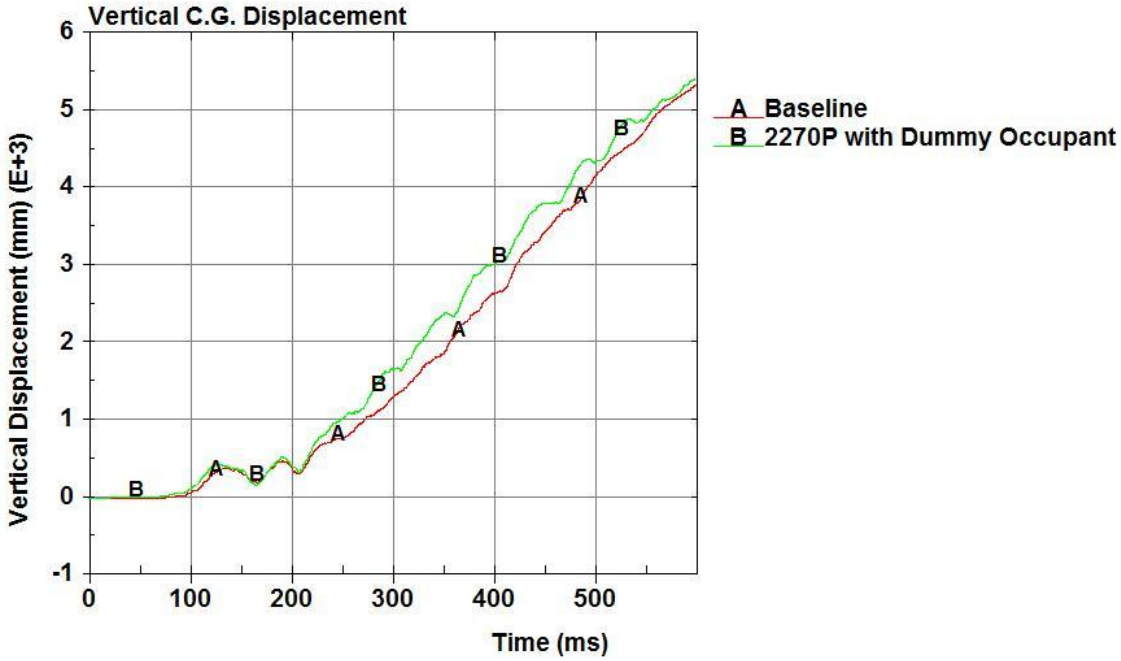

Figure 86. Vehicle Vertical Displacement

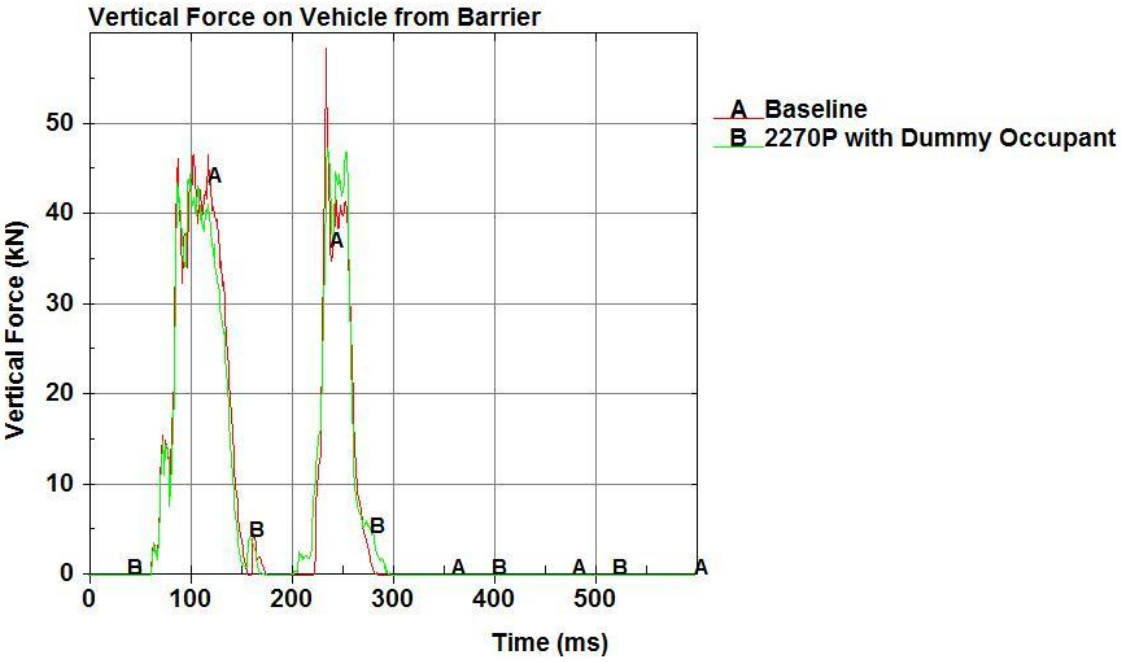

Figure 87. Vertical Force between the Vehicle and the Barrier

8.8.2 Vehicle Roll Angle

The roll angles of the baseline and dummy-in-vehicle simulations are shown in Figure 88. Note that impact occurred at 60 ms into the simulation. The roll angles diverged at approximately 105 ms, which was the same time that the dummy occupant impacted into the door. The roll angular rates of the two simulations were filtered using an SAE 60 12-point average filter and are shown in Figure 89. The roll rates were larger for the vehicle model that included the dummy model, but the roll rate peaks occurred at the same time in each simulation.

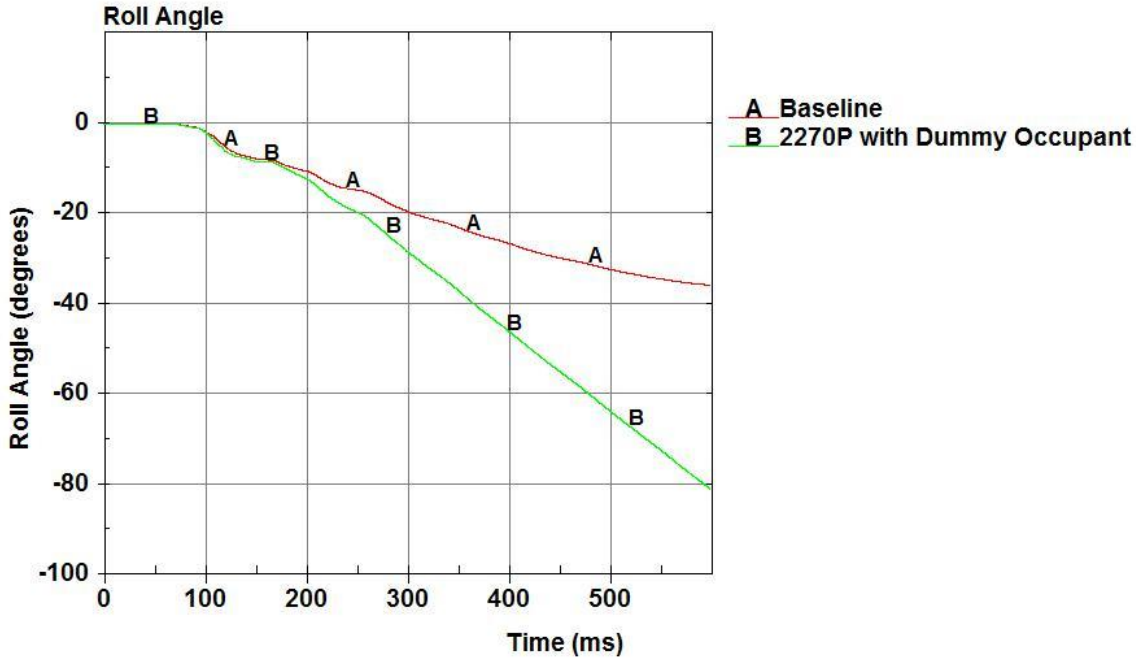

Figure 88. Vehicle Roll Angle

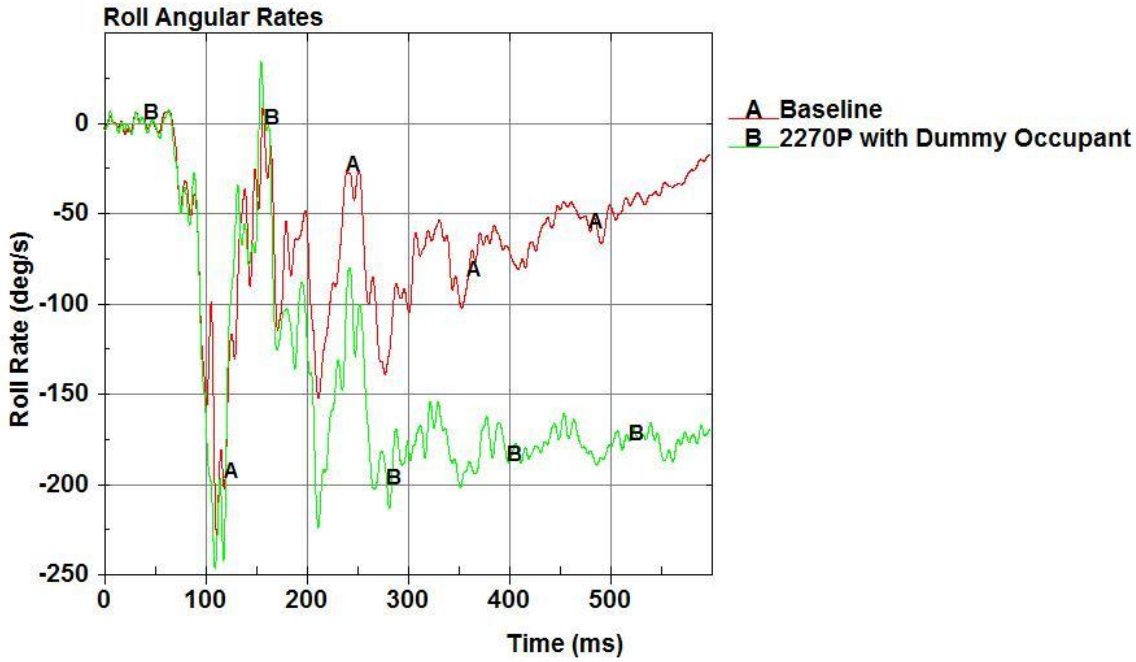

Figure 89. Vehicle Roll Angular Rates

8.9 Conclusions and Future Work

The inclusion of a dummy, seat, and seatbelt model into a 2270P simulated vehicle caused the vehicle to roll over during the simulation. The impact between the dummy and the door was more severe than impacts seen in full-scale crash testing, and several factors may have caused this:

- Impact forces between the dummy occupant and the door were relatively large. Based on the deflection of the door during the simulation, it is believed that this force was excessive. However, the actual impact forces between the dummy occupant and the vehicle door are currently unknown.
- The seatbelt model was not initially in contact with the occupant, providing a gap between the dummy occupant and the belt. At the same time, the dummy occupant was not initially in contact with the seat. The

dummy settled into the seat as the simulation progressed, which further separated the occupant from the seatbelt. A large gap existed between the seatbelt and the dummy occupant at impact time. Thus, the dummy occupant traveled unrestrained laterally for some time before impacting the door.

- The top-front corner of the 9.1-degree single-slope barrier was modeled as three lines connected by sharp points. The sharp edges defining the top of the barrier may have contributed to the vertical force on the vehicle, increasing the vehicle climb. However, this does not explain why the vehicle rolled over.

This simulation model needs improvement and verification before the dummy-in-vehicle model can be used to quantitatively assess the interaction between the occupant and the occupant compartment.

- The dummy occupant that was chosen for this simulation was a simplified dummy model. Other 95^{th} percentile simulated male occupants may impart different forces on the door.
- The coefficient of friction between the vehicle and the barrier (studied in Section 5.9) showed that lower vehicle-to-barrier friction coefficients caused higher yaw rates into the barrier, which contributes to the severity of the impact between the dummy and the door. Choosing a higher friction coefficient may reduce the force between the vehicle and the door.
- At impact, the seatbelt should be taut against the dummy occupant. This could be performed by allowing the dummy to settle into the seat,

prestressing the foam seat bottom and backs to support the occupant, and tightening the seatbelt on the model to make a more snug fit.

- Contact definitions need to be improved for the seatbelt and occupant. The legs intersected each other during the simulation, and the seatbelt went through the chair. While these intersections probably would not drastically affect the trajectory of the vehicle, they are pertinent for studying the interaction between the occupant and the occupant compartment.

8.10 Disclaimer

Note: the following is duplicated from the beginning of this chapter, but it warrants repeating.

The automotive industry has been successfully modeling dummies in vehicles for many years. Unfortunately, details of such models are not available due to proprietary reasons. Simulating dummies in roadside safety applications has been rare. Work presented herein is a first attempt at such modeling. These techniques are complicated and will need significant research before results could be considered realistic.

9 CONCLUSIONS

Simulation of a 2270P Silverado model impacting 36-in., 42-in., and 56-in. (914-mm, 1,067-mm, and 1,422-mm) tall, 9.1-degree single-slope concrete barriers were performed according to the TL-3 specifications set forth in MASH. Prior to the simulations being conducted, an extensive literature review and parameter study was conducted to verify that the values determined in this study were the most realistic. Critical ZOIs and working widths were calculated from this research. Each barrier was evaluated under multiple suspension failure conditions, and the maximum values for each barrier height are shown in Table 16. It was assumed that the fender protrusion would not pose a risk to the vehicle's occupants if impacted behind the barrier, but it is shown in Table 16 for comparison. Note that the fender only protruded the farthest for the 36-in. (914-mm) tall, single-slope barrier.

Table 16. ZOI and Working Width of the Rigid 9.1-degree Single-Slope Barrier

Barrier Height in. (mm)	Fender ZOI in. (mm)	Hood ZOI in. (mm)	Working Width in. (mm)
36 (914)	12.2 (310)	9.4 (240)	24.0 (610)
42 (1,067)	6.4 (162)	6.5 (165)	24.0 (610)
56 (1,422)	0 (0)	0 (0)	24.0 (610)

For these simulations, the working width was dependent on the vehicle penetration behind the barrier (or the ZOI) and the width of the barrier. However, none of the vehicle components protruded beyond the back of the barrier. Thus, the working width for each system was determined to be the width of the barrier, as shown in Table 16.

10 FUTURE WORK

For this study, several issues were noted that warrant further investigation in order to gain a better understanding of concrete barriers, further investigate the zone of intrusion, and to improve vehicle to concrete barrier models.

10.1 Concrete Barrier Research

- Many of the concrete barriers on the roadway today were designed for vehicles and impact conditions from over 40 years ago. The vehicle fleet has changed dramatically in 40 years, yet concrete barriers have not. Research conducted by the Southwest Research Institute while developing the F-shape barrier showed that steeper barrier slopes resulted in more stable vehicle trajectory [30]. The Texas single-slope barrier was developed based on the width of many medians seen in Texas, while the California single-slope barrier was developed based on the width of many medians seen in California. With the resources available to researchers today, a concrete barrier can be designed for today's vehicle fleet to optimize vehicle stability, reduce vehicle damage, and prevent rollover.
- Full-scale pickup truck crash tests into concrete barriers have only been performed at an impact angle of 25 or 20 degrees. However, when the New Jersey barrier was developed, it was understood that the vehicle trajectory changed with impact angle, and some impact angles were noted to have adverse effects on vehicles. It is recommended that each concrete barrier system be evaluated at different impact angles ranging from 25 degrees down to 2 degrees.

- As noted in this study, unrestrained or lightly-restrained temporary barrier systems behave differently from restricted-motion temporary barrier systems and permanent, rigid concrete barrier systems. With a wealth of crash tests available, researchers may be able to note similarities between temporary barrier systems and determine factors affecting vehicle trajectory and impact severity for temporary barrier systems. Such research could also give more insight into the effects of restricting barrier motion.
- Several concrete barrier research reports suggested that the interaction between the vehicle and the barrier was dependent on the c.g. height of the impacting vehicle. With modern crash-testing standards, the vehicle c.g. height is fairly static, and a small sampling of c.g. heights is available. In order to assess the crashworthiness of each barrier system for a variety of vehicles, concrete barriers must be evaluated when impacted by vehicles of different c.g. heights.

10.2 Vehicle and Vehicle Model Research

- The anti-roll bar in a vehicle is important for good vehicle dynamics behavior. Its influence on rollover during an impact event is unknown. An investigation into the roll bar on both the C2500 and Silverado models is recommended.
- For both the 2270P and 2000P vehicle models, the vehicle climb up the barrier was less than observed in full-scale crash testing. Further work is needed to investigate the vehicle climb up a concrete barrier.

10.3 ZOI Research

- During this test, the ZOI was determined for three barrier heights of the 9.1-degree single-slope barrier. ZOI values have not been determined for the New Jersey, F-Shape, vertical, or Texas 10.8-degree single-slope barrier at other heights. This effort would require a detailed investigation of the front-end geometry for various pickup trucks (e.g. the Dodge Ram vs. the Chevy Silverado). Full-scale crash tests and simulations are recommended to determine the ZOI for other types of concrete barriers.
- ZOI is measured from critical points on the vehicle that may impact objects behind the front face of the barrier. Currently, it is assumed that the fender does not pose a risk to the occupant compartment, but impacts with the hood will cause risk of penetration. However, it was noted in crash test no. CBPP-1 that an impact from the vehicle hood into a rigid concrete pier behind the barrier did not pose a risk to the occupants of the vehicle [14]. To best understand how to measure ZOI, research should be conducted to determine the critical points on the barrier.
- Crash testing agencies rarely conduct full-scale crash tests at impact angles higher than 25 degrees. For higher-angle impacts, the impact severity is higher, and this would result in higher ZOI values. At some angle, the ZOI will be at a maximum. Finding the angle of maximum ZOI would help researchers understand how better to shield occupants from hazards located behind or on top of barrier systems.

- TTI conducted a test to determine the ZOI of a free-standing temporary barrier system [13]. A 2270P vehicle impacted into a 32-in. (813-mm) tall F-shape temporary concrete barrier with a rigid sign mounted on it, and the lateral distance between the top-front corner of the barrier and the sign was less than 3 in. (76 mm), which violated the ZOI. The test passed without the hazard causing excessive accelerations or penetrating into the occupant compartment. Since vehicle trajectory differs greatly between free-standing temporary barrier systems and rigid barrier systems, the ZOI is also expected to be different between the two systems. Research conducted into barrier resistance and ZOI could give greater insight into how ZOI can be applied to non-rigid systems.

10.4 Dummy Occupant Research

- For many crash tests, the 95th percentile male dummy is used because it tests the most massive dummy, which may have the greatest protrusion out of the vehicle and may cause the most significant difference in vehicle trajectory. Thus, other dummy types are not currently evaluated in roadside safety applications.
- While simulated occupants are placed in the front seat of many crash tests conducted according to MASH standards, there has been no research conducted to determine the effect of impacting barriers on occupants in other seating positions. As noted during this research, the impact-side rear door separated from the vehicle more than the impact-side front door. Thus, occupant ejection may be more severe at other locations in the

vehicle. The effect of placing a dummy at other locations in the vehicle would have to be evaluated to determine this effect.

- In the 1980s, the Texas A&M Transportation Institute published a report explaining how instrumented dummies do not provide an accurate measurement of impact severity or occupant safety during a crash event [31]. Following that report, TTI ceased to use dummies in their concrete barrier crash tests, and little research has been performed on the interaction between the occupant and the occupant compartment during a crash test. With new resources available to researchers today, occupant safety evaluation can be performed realistically with repeatable, accurate results. Since so little research has been conducted on occupant safety inside the occupant compartment during a full-scale crash, this is an area that warrants investigation. Work was performed in this study to set the grounds for future evaluation of the effects of crash tests on occupants, but it must be expanded.

11 REFERENCES

1. *Manual for Assessing Safety Hardware (MASH)*, American Association of State Highway and Transportation Officials (AASHTO), Washington, D.C., 2009.

2. Ross, H.E., Sicking, D.L., Zimmer, R.A. and Michie, J.D., *Recommended Procedures for the Safety Performance Evaluation of Highway Features*, National Cooperative Highway Research Program (NCHRP) Report No. 350, Transportation Research Board, Washington, D.C., 1993.

3. Stolle, C.J., Reid, J.D., and Faller, R.K., *Literature Review of the Zone of Intrusion for Concrete Barrier Systems*, Draft Report to the Wisconsin Department of Transportation, University of Nebraska-Lincoln, January 2013, Draft Report.

4. Beason, W.L., Ross Jr., H.E., Perera, H.S., Campise, W.L., and Bullard Jr., D.L., *Development of a Single-Slope Concrete Median Barrier*, TTI Research Report No. 9429CDK-1, Texas Transportation Institute, June 1989.

5. Mak, K.K., Bligh, R.P., and Menges, W.L., *Testing of State Roadside Safety Systems Volume VIII: Appendix G - Crash Testing and Evaluation of the Single Slope Bridge Rail*, TTI Research Report No. 471470-Vol. VIII, Texas Transportation Institute, February 1998.

6. Williams, W.F., Bligh, R.P., and Menges, W.L., *MASH Test 3-11 of the TxDOT Single Slope Bridge Rail (Type SSTR) on Pan-Formed Bridge Deck*, Research Report No. 9-1002-3, The Texas A&M Transportation Institute, The Texas A&M University System, College Station, TX, November 2010.

7. Jewell, J., Rowhani, P., Stoughton, R., and Crozier, W., *Vehicular Crash Tests of a Slip-formed, Single Slope, Concrete Median Barrier with Integral Concrete Glare Screen*, Caltrans Research Report No. 6367057, California Department of Transportation, December 1997.

8. Jewell, J., Peter, R., and Whitesel, D., *Compliance Crash Testing of a Type 60K Terminus*, Research Report No. FHWA/CA08-0287, California Department of Transportation, December 2008.

9. Jewell, J., Rowhani, P., Meline, R., and Peter, R., *Vehicle Crash Tests of the Type 70 Bridge Rail*, Caltrans Research Report No. 680600, California Department of Transportation, January 1998.

10. Keller, E.A., Sicking, D.L., Faller, R.K., Polivka, K.A., and Rohde, J.R., *Guidelines for Attachments to Bridge Rails and Median Barriers*, Final Report to the Midwest States Regional Pooled Fund Program, Transportation Record No. TRP-03-98-03, Midwest Roadside Safety Facility, University of Nebraska-Lincoln, February 26, 2003.

11. Wiebelhaus, M.J., Polivka, K.A., Faller, R.K., Rohde, J.R., Sicking, D.L., Holloway, J.C., Reid, J.D., and Bielenberg, R.W., *Evaluation of Rigid Hazards Placed in the Zone of Intrusion*, Final Report to the Midwest State's Regional Pooled Regional Pooled Fund Program, Transportation Research Report No. TRP-03-151-08, Project No.: SPR-3(017), Project Code: RPFP-03-03 - Year 13, Midwest Roadside Safety Facility, University of Nebraska-Lincoln, January 3, 2008.

12. Rosenbaugh, S.K., Sicking, D.L., and Faller, R.K., *Development of a TL-5 Vertical Face Concrete Median Barrier Incorporating Head Ejection Criteria*, Final Report to the Midwest States Regional Pooled Regional Pooled Fund Program, Transportation Research Report No. TRP-03-194-07, Project No.: SPR-3(017), Project Code: RPFP-05-01 - Year 15, Midwest Roadside Safety Facility, University of Nebraska-Lincoln, December 10, 2007.

13. Williams, W.F., and Menges, W.L., *MASH Test 3-11 of the TXDot Portable Type 2 PCTB with Sign Support Assembly*, Research Report No. 0-6143-1, The Texas A&M Transportation Institute, January 2011.

14. Rosenbaugh, S.K., Faller, R.K., Hascall, J.A.,Allison, E.M., Bielenberg, R.W., Rohde, J.R., Polivka, K.A., Sicking, D.L., and Reid, J.D., *Development of a Stand-Alone Concrete Bridge Pier Protection System*, Final Report to the Midwest States Regional Pooled Regional Pooled Fund Program, Transportation Research Report No. TRP-03-190-08, Project No.: SPR-3(017), Project Code: RPFP-04-05 - Year 14, Midwest Roadside Safety Facility, University of Nebraska-Lincoln, April 18, 2008.

15. Reid, J.D., and Sicking, D.L., *Zone of Intrusion*, Final Report to the Florida Department of Transportation, Transportation Research Report No. TRP-03-242-10, Project No.: PR4893118-V2, Midwest Roadside Safety Facility, University of Nebraska-Lincoln, Lincoln, Nebraska, October 15, 2010.

16. Schmidt, T.L., Bielenberg, R.W., Faller, R.K., Lechtenberg, K.A., Reid, J.D., and Sicking, D.L., *Dynamic Evaluation of the Powell Contracting Ltd Temporary Concrete Barrier*, Final Report to Powell Contracting Ltd. Transportation Record No. TRP-03-273-12, Midwest Roadside Safety Facility, University of Nebraska-Lincoln, January 25, 2013.

17. Stolle, C.J., Polivka, K.A., Faller, R.K., Sicking, D.L., Bielenberg, R.W., Reid, J.D., Rohde, J.R., Allison, E.M., and Terpsma, R.J., *Evaluation of Box Beam Stiffening of Unanchored Temporary Concrete Barriers*, Final Report to the New York State Department of Transportation, Transportation Research Report No. TRP-03-202-08, Project No.: C-06-17, Midwest Roadside Safety Facility, University of Nebraska-Lincoln, March 14, 2008.

18. Schmidt, J.D., Faller, R.K., Lechtenberg, K.A., Sicking, D.L., and Reid, J.D., *Development and Testing of a New Vertical-Faced Temporary Concrete Barrier for Use on Composite Panel Bridge Decks*, Final Report to the Kansas Department of Transportation, Transportation Research Report No. TRP-03-220-09, Sponsor Agency Code: SPR-3(017) Supplement No. 57, Midwest Roadside Safety Facility, University of Nebraska-Lincoln, October 13, 2009.

19. Wiebelhaus, M.J., Terpsma, R.J., Lechtenberg, K.A., Reid, J.D., Faller, R.K., Bielenberg, R.W., Rohde, J.R., and Sicking, D.L., *Development of a Temporary Concrete Barrier to Permanent Concrete Median Barrier Approach Transition*, Final Report to the Midwest States Regional Pooled Fund Program, Transportation Research Report No. TRP-03-208-10, Project No.: SPR-3(017), Project Codes: RPFP-06-07 and RPFP-06-09 - Year 16, Midwest Roadside Safety Facility, University of Nebraska-Lincoln, Lincoln, Nebraska, July 15, 2010.

20. Howard, C.N., Stolle, C.J., Lechtenberg, K.A., Faller, R.K., Reid, J.D., and Sicking, D.L., *Dynamic Evaluation of a Pinned Anchoring System for New York State's Temporary Concrete Barriers*, Final Report to the New York State Department of Transportation, Transportation Research Report No. TRP-03-216-09, Project No.: TPF-5(193), Supplement No. 8, Midwest Roadside Safety Facility, University of Nebraska-Lincoln, September 8, 2009.

21. Lechtenberg, K.A., Faller, R.K., Reid, J.D., and Sicking, D.L., *Dynamic Evaluation of a Pinned Anchoring System for New York State's Temporary Concrete Barriers - Phase II*, Final Report to the New York State Department of Transportation, Transportation Research Report No. TRP-03-224-10, Project No.: TPF-5(193), Supplement #11, Midwest Roadside Safety Facility, University of Nebraska-Lincoln, January 27, 2010.

22. Rosenbaugh, S.K., Bielenberg, R.W., Faller, R.K., Reid, J.D., Rohde, J.R., Sicking, D.L., Lechtenberg, K.A., and Holloway, J.C., *Termination and Anchorage of Temporary Concrete Barriers*, Final Report to the Midwest State's Regional Pooled Fund Program, Transportation Research Report No. TRP-03-209-09, Project No.: SPR-3(017), Project Code: RPFP-06-02 - Year 16, Midwest Roadside Safety Facility, University of Nebraska-Lincoln, Lincoln, Nebraska, October 29, 2009.

23. Polivka, K.A., Faller, R.K., Rohde, J.R., Holloway, J.C., Bielenberg, B.W., and Sicking, D.L., *Development and Evaluation of a Tie-Down System for the Redesigned F-Shape Concrete Temporary Barrier*, Final Report to the Midwest States Regional Pooled Fund Program, Transportation Research Report No. TRP-03-134-03, Project No. SPR-3(017)-Year 13, Project Code: RPFP-03-06, Midwest Roadside Safety Facility, University of Nebraska-Lincoln, August 22, 2003.

24. Sheikh, N.M., Bligh, R.P., and Menges, W.L., *Crash Testing and Evaluation of the 12 ft Pinned F-Shape Temporary Barrier*, Research Report No. 405160-3-1, The

Texas A&M Transportation Institute, The Texas A&M University System, College Station, TX, April 2008.

25. Mak, K.K., and Sicking, D.L., *Rollover Caused by Concrete Safety Shaped Barrier Volume I - Technical Report*, Research Report No. RF7051, The Texas A&M Transportation Institute, The Texas A&M University System, College Station, TX, January 1989.

26. White, M., Jewell, J., and Peter, R., *Crash Testing of Various Textured Barriers*, Caltrans Research Report No. 65-68 0445, California Department of Transportation, September 2002.

27. Bullard, Jr., D.L., Bligh, R.P., Menges, W.L., and Haug, R.R., *Volume I: Evaluation of Existing Roadside Safety Hardware Using Updated Criteria - Technical Report*, Contractor's Final Report for NCHRP Project 22-14(03), the Texas A&M Transportation Institute, The Texas A&M University System, College Station, TX, March 2010.

28. Mohan, P., Ritter, M., Marzougui, D., Brown, D., Kan, C., and Opiela, K., *Modeling, Testing, and Validation of the 2007 Chevy Silverado Finite Element Model*, Research Report No. 2009-W-005, National Crash Analysis Center, the George Washington University, Ashburn, VA, October 2009.

29. J.D. Reid and N.R. Hiser, *Friction Modeling Between Solid Elements*, International Journal of Crashworthiness, Vol. 9, No. 1, 2004, pp. 65-72.

30. Bronstad, M.E., Calcote, L.R., and Kimball, C.E., Jr., *Concrete Median Barrier Research Volume 2: Research Report*, Research Report No. 03-3716-2, Southwest Research Institute, March 1976.

31. Buth, E., Arnold, A., Campise, W.L., Hirsch, T.J., Ivey, D.L., and Noel, J.S., *Safer Bridge Railings Volume II: Appendices A, B, D, and E*, Research Report No. FHWA-RD-82-073, The Texas A&M Transportation Institute, The Texas A&M University System, College Station, TX, June 1984.

32. Buth, E., Arnold, A., Campise, W.L., Hirsch, T.J., Ivey, D.L., and Noel, J.S., *Safer Bridge Railings Volume II: Appendices A, B, D, and E*, Transportation Research Report No. FHWA-RD-82-073, Texas A&M Transportation Institute, College Station, TX, June 1984.

33. *LSTC Models Overview*. Livermore Software Technology Corporation, <http://www.lstc.com/models>.

34. *Development & Validation of a Finite Element Model for the 2010 Toyota Yaris Passenger Sedan,* National Crash Analysis Center, Techical Summary NCAC 2011-T-001, November 2011.

Appendix A. 2000P SIMULATIONS WITH THE F-SHAPE BARRIER

A.1 Introduction

A physical analysis of one impact between a 2000P vehicle and an F-shape concrete barrier was conducted and reviewed in Section 3.4. However, simulation models do not always closely resemble physical testing, and continued work is needed to improve any model. While finite element software allows for intricate analysis of component interactions with roadside barriers and the barriers' responses, research studies on intricate dynamic evaluation of concrete barriers are not widely available. Thus, simulations were conducted to review the behavior of a vehicle impacting a concrete barrier and to determine factors affecting the simulation. Results from these simulations would provide insight into contact definitions and expected simulated vehicle motion for the Silverado model.

A.2 Model Description

In 2010, a study was conducted to determine the zone of intrusion of a 2000P vehicle impacting a 40-in. (1,016-mm) tall F-shape permanent concrete barrier [A-1]. LS-DYNA simulations were performed according to NCHRP Report No. 350 standards utilizing a C2500 pickup truck model to determine the ZOI of the barrier at different speeds.

The vehicle model and barrier materials from the 2010 ZOI study served as the basis for the 2000P simulations. The vehicle model, contact definitions, the barrier material model, and simulation controls were copied from this model. An LS-DYNA model of a 32-in. (813-mm) tall F-shape concrete barrier was drawn and meshed for use

with the 2000P vehicle. The mesh on the barrier was 40 mm by 40 mm, and the barrier material was the standard simulated rigid material.

Simulation and parameter work performed in the late 1980s by TTI showed coefficients of friction between the vehicle and the barrier to be between 0.4 and 0.8 [A-2]. However, the coefficient of friction determined from simulation parameter studies may not correlate with the coefficient of friction best defining the impact in the simulation.

The friction behavior between two objects in simulations is dependent on a number of factors, including mesh size, material, and simulation timestep [A-3]. In the 2010 ZOI study, the barrier model utilized coefficients of friction of 0.05, 0.3, and 0.6. The 0.6 coefficient of friction was chosen to review the C2500 simulated impact for this study.

A.3 Simulation Results

Simulation results were compared to a full-scale test that was conducted on the F-shape barrier system at similar impact conditions [A-4]. A comparison between the simulation and the full-scale crash test is shown in Figure A-1. Differences between the full-scale results and the simulation results provided insight into potential improvements in the vehicle model.

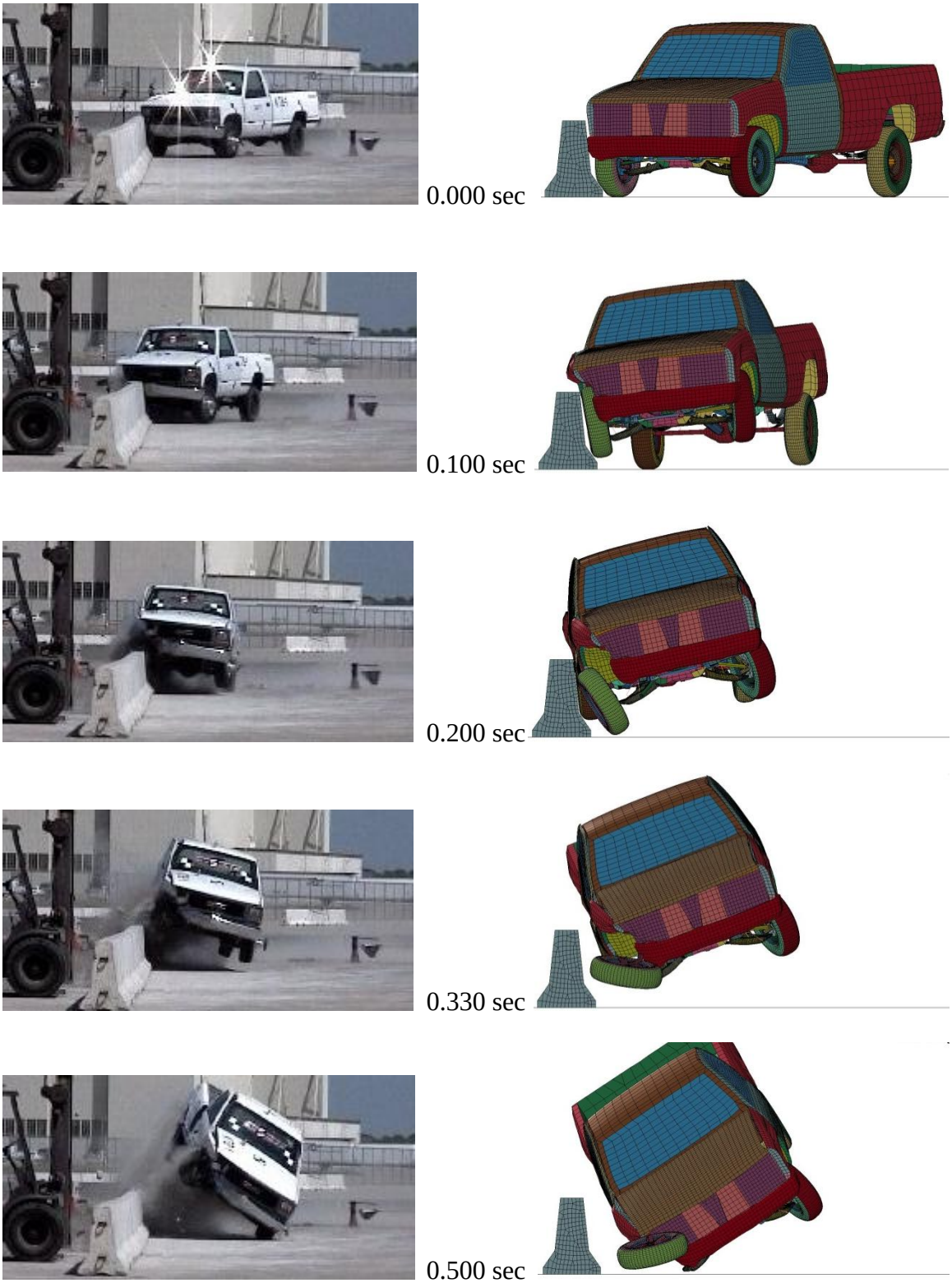

Figure A-1. Sequential Comparison of Test No. KTB-1 and the Baseline Simulation

The simulation results diverged from the full-scale test in several areas. The most notable differences in the simulated model were that the vehicle rolled toward the barrier, the impacting tire did not climb the upper sloped face, and the front tires steered away from the barrier during the impact.

For this model, the zone of intrusion of the vehicle was consistent with the ZOI observed in the full-scale test. For C2500 impacts into rigid concrete barriers, the corner of the hood has protruded the farthest behind the front face of the barrier. In the simulation, the hood protruded the farthest as well. As measured from the protruding hood member, the ZOI for the simulation model was 16.5 in. (418 mm).

During an impact with a sloped concrete barrier, the impacting tire deforms significantly. Much of this deformation is elastic, although the tire may undergo plastic or permanent deformation when it is punctured during the impact. Deformation of the impacting tire was reviewed. The deformed tire shape is shown in Figure A-2. Unfortunately, comparing the simulated tire deformation to full-scale results was not possible as it is difficult to photograph tire deformation during full-scale crash testing.

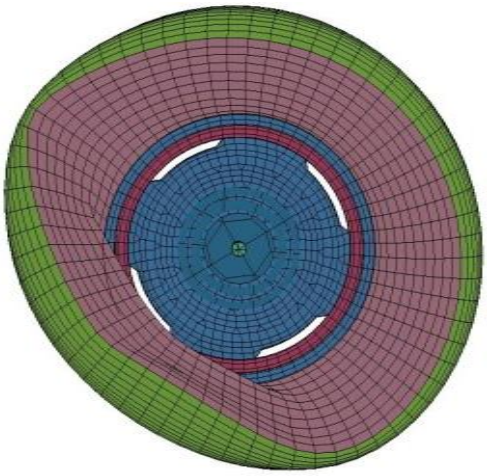

Figure A-2. Deformed Tire Shape with a 0.6 Coefficient of Friction

In the full-scale test, the impacting tire climbed up the upper sloped face of the barrier. However, in the simulation, the impacting tire did not climb the upper sloped face at all. A plot of the vehicle tire vertical deflection is shown in Figure A-3. The height of the barrier overall was 32 in. (813 mm). The height of the toe was 3 in. (76 mm), and the height of the toe and lower sloped face was 10 in. (254 mm) above ground level. During the impact, the tire compressed, and the center hub height change was not as large as the climb of the bottom of the tire.

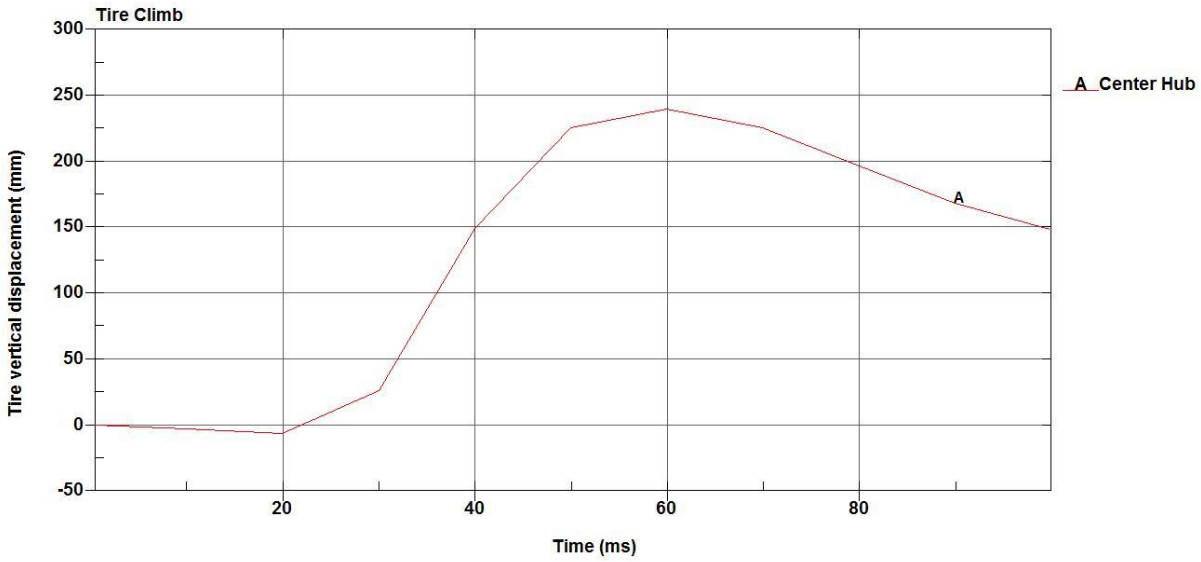

Figure A-3. Baseline Model Tire Climb

The vehicle rolled toward the barrier during the impact sequence in the baseline simulation, which is inconsistent with all full-scale test results into permanent or rigid concrete barrier systems. Vehicle roll toward the barrier was observed in some full-scale tests involving unrestrained temporary barriers, but unrestrained temporary barriers were not evaluated during this study. The roll angles for the baseline simulation and test no. FTB-1 are plotted in Figure A-4. Initially, the roll angle of the model correlated with the roll angle of the full-scale model (between 0 and 50 ms). However, after 50 ms (which

was approximately the time when the impacting tire contacted the upper slope of the barrier), the full-scale vehicle began to roll away from the barrier. In the simulated model, the vehicle continued to roll toward the barrier. At approximately 200 ms after impact, the rear tire contacted the toe of the barrier. For the simulated model, the vehicle ceased to roll towards the barrier temporarily at 200 ms after impact. For the full-scale test, the vehicle roll angle continued to increase steadily as the rear tire climbed the upper sloped face at 200 ms after impact. Finally, the roll angular rate became constant as the vehicle exited the barrier while airborne.

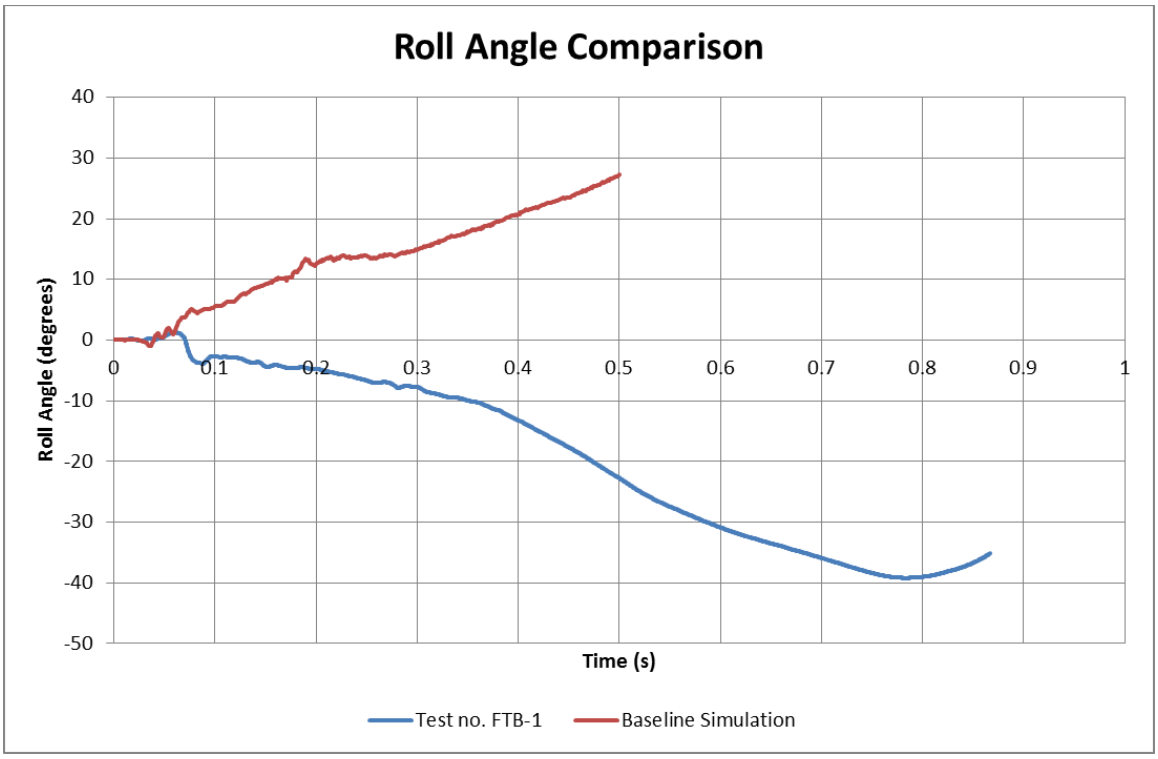

Figure A-4. Roll Angle Comparison

A.4 2000P Vehicle Impact into F-Shape Barrier Conclusions

Simulation results diverged greatly from the expected results. The vehicle behavior must be evaluated in stages to assess the cause of the divergences. Since the

divergence began in the impact stage, analysis of the rest of the stages shows little merit. If the baseline model were to be improved, efforts must be undertaken to increase the vehicle climb up the barrier.

The tire model in the C2500 simulated vehicle was developed and tested rigorously [A-5]. Based on the behavior of this tire during compression and the amount of work required to improve the model, it was assumed that the tire was not the issue. The contact between the vehicle and the barrier, the barrier mesh, the barrier material, the vehicle suspension, and the timestep were noted as potential improvements that should be evaluated to improve the vehicle model.

A.5 References

A-1. Reid, J.D., and Sicking, D.L., *Zone of Intrusion*, Final Report to the Florida Department of Transportation, Transportation Research Report No. TRP-03-242-10, Project No.: PR4893118-V2, Midwest Roadside Safety Facility, University of Nebraska-Lincoln, Lincoln, Nebraska, October 15, 2010.

A-2. Mak, K.K., and Sicking, D.L., *Rollover Caused by Concrete Safety Shaped Barrier Volume I - Technical Report*, Research Report No. RF7051, The Texas A&M Transportation Institute, The Texas A&M University System, College Station, TX, January 1989.

A-3. Reid, J.D., *LS-DYNA Introductory Training Class Notes*, University of Nebraska-Lincoln, Fall 2011.

A-4. Bielenberg, B.W., Faller, R.K., Rohde, J.R., Ried, J.D., Sicking, D.L., and Holloway, J.C., *Development of Tie-Down and Transition Systems for Temporary Concrete Barrier on Asphalt Road Surfaces*, Final Report to the Midwest States Regional Pooled Regional Pooled Fund Program, Transportation Research Report No. TRP-03-180-06, Midwest Roadside Safety Facility, University of Nebraska-Lincoln, February 23, 2007.

A-5. Boesch, D.A., *Front Suspension and Tire Modeling – For Use in Culvert Grate Impact Simulation*, Master's Thesis presented to the College of Engineering, University of Nebraska-Lincoln, April 2004.

Appendix B. C2500 VEHICLE ANTI-ROLL BAR RESEARCH

While analyzing the results of the 2000P simulation, it was noted that the anti-roll bar in the C2500 simulated vehicle was improperly defined. An anti-roll bar, as shown in Figure B-1, is comprised of a single steel tube with outer and inner diameters of 1.341 and 0.860 in. (34.05 and 21.85 mm), respectively. The bar is tubular to minimize the weight, but it is thick enough to resist torque, bending shear, and bending moments. An 88-degree bend and a 25-degree bend in the bar provide proper alignment and maximize the component strength while minimizing stresses due to loading.

B.1 Physical Roll Bar

Pins connect the lower control arm to the end of the anti-roll bar on each side. The pin is composed of a ¼-in. (6-mm) diameter, 8⅛-in. (206-mm) long hex head bolt. A 1⅜-in. (35-mm) diameter washer was placed on the end with a 1⅜-in. (35-mm) diameter semi-stiff rubber gasket. A ¾-in. (19-mm) diameter, 6½-in. (165-mm) long hollow tube with rubber gaskets on both ends was put onto the bolt and a tubular stiffener wrapped around the bolt are used to link the anti-roll bar and the suspension. Rotational tolerance is allowed in the anti-roll bar's connection to the pin. However, no translational motion is allowed, giving the pin connection three degrees of freedom.

Figure B-1. Actual Anti-Roll Bar and Pin Connection

The model of the anti-roll bar, pins, and lower control arms are shown in Figure B-2. The anti-roll bar must be able to transfer torque as the two ends of the anti-roll bar displace, but this is dependent on the connections that define the ends of the anti-roll bar. The pin is modeled as a beam element, and the node at the lower end of the pin is merged with a node on the lower A-arm, acting as a spherical joint. Thus, the connection between the pin and the lower A-arm currently has three unrestrained degrees of freedom. The anti-roll bar is also modeled as a beam element, and the nodes at the ends of the anti-roll bar are merged with the nodes in the pins, giving the joint three unrestrained degrees of freedom. Overall, the anti-roll bar has six unrestrained degrees of freedom in the current simulated model.

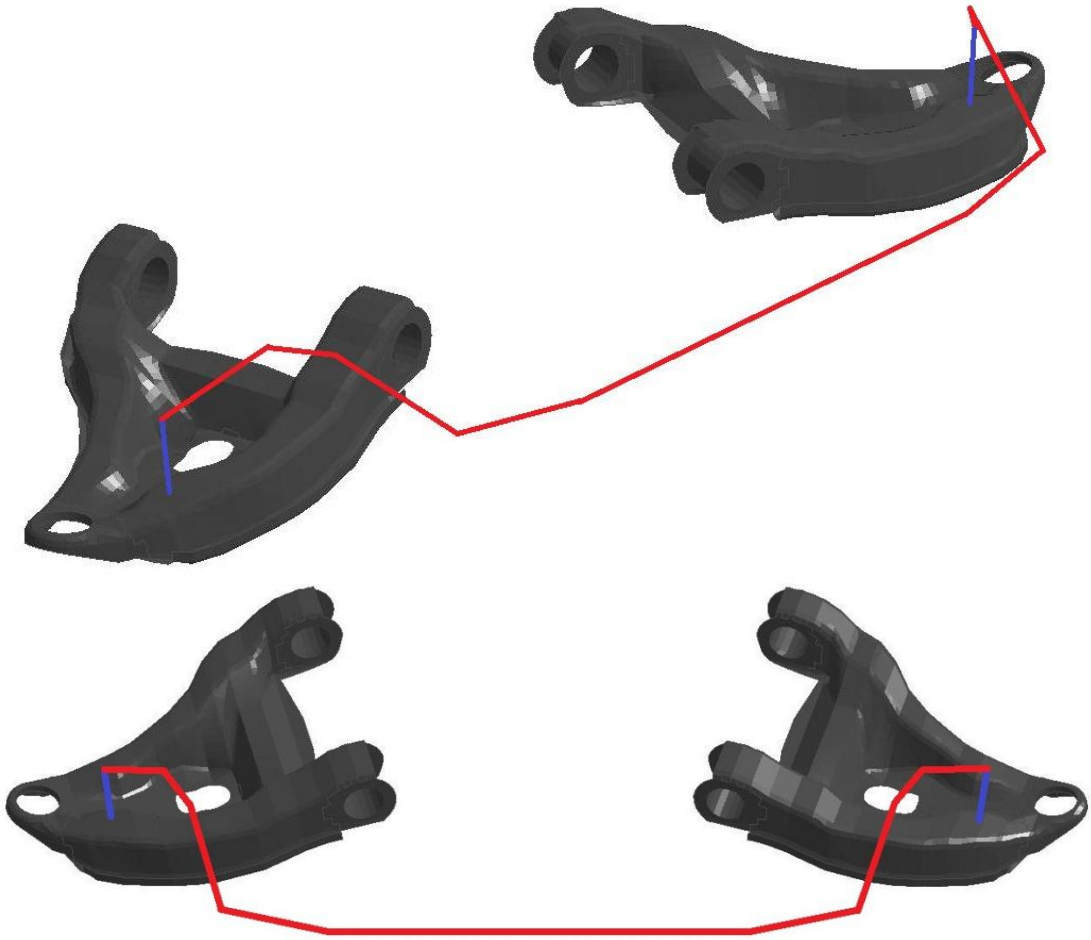

Figure B-2. Simulated Anti-Roll Bar, Pins, and Lower Control Arms

B.2 Anti-Roll Bar Modeling Research

Anti-roll bars, common safety measures which were patented as early as 1965 [B-1], are often used to mitigate risk of rollover in minor to moderate turning situations. Vehicle dynamics dictate the need for simple, reliable steering mechanisms as well as mechanisms to stabilize vehicle motion during roll.

An anti-roll bar is designed to resist the roll tendency of a vehicle when the vehicle is cornering or turning [B-2,B-3]. As a vehicle body rotates, the tires camber changes in the direction of the turn. The outside wheel tends to deflect and cause

suspension compression while the inside turning wheels are typically subjected to an opposite tensile force, or rather, the spring on the inside suspension tends to unload. This generates a roll moment applied to the vehicle which counteracts the frictional moment caused by the lateral ground force at the turning wheels. By centering the steering through the vehicle's roll center, suspension designs can be minimalistic, and optimum configurations of the anti-roll bar and suspension can be developed.

In 2003, Kemal Caliskan published a thesis detailing the design and optimization of rollbars using finite-element analysis [B-4]. He explained that roll bars were commonly constructed from SAE 5160 with a modulus of elasticity of 29.9 Mpsi (206.0 GPa) and a Poisson's ratio of 0.27, with a yield strength of 171 kpsi (1180 MPa) and a density of 487 lb/ft^3 (7800 kg/m^3). However, most of this work was involved in the design of an anti-roll bar, and the paper recognized some inaccuracies in the data and method. Thus, aside from any corrections to the anti-roll bar constraints, research will still need to be performed to verify the material and sectional model of the anti-roll bar in order to accurately obtain vehicle suspension behavior.

For his thesis, Dustin Boesch remodeled the FEA model of the suspension of the C2500 pickup truck [B-5]. However, he did not review the anti-roll bar or the steering linkage.

B.3 Solid-Element Anti-Roll Bar Model

An anti-roll bar was meshed using solid elements. The end of the sway bar where it attaches to the pin has an irregular geometry, as the tube is squished to form a rectangular cross-section. Despite multiple meshing attempts, this part of the anti-roll bar was unable to be meshed correctly and cohesively. It was decided that this part of the

anti-roll bar did not contribute significantly to the torsion or bending of the anti-roll bar, nor did it pose a significant risk of bending. Thus, this portion was modeled as a nodal rigid body (which is not visible in pictures). The meshed model of the anti-roll bar is shown in Figure B-3.

Figure B-3. Meshed Model of the Anti-Roll Bar

B.3.1 Anti-Roll Bar Issues

While a solid model of the roll bar had been developed, the constraints that control the motion of the ends of the anti-roll bar must be better defined. The complicated connection between the pin and the lower A-arm would require a limited-motion, three-degree-of-freedom joint with increased resistance as it deflects from the vertical orientation. A similar joint would have to be constructed between the pin and the anti-roll bar. Thus, despite having a new model of a roll bar, without the constraints to add to it, the model could not be implemented.

B.3.2 Future Work

Further work is yet to be performed with this sway bar model to determine if it improved the model behavior. Physical testing must be conducted on an anti-roll bar to verify that the new anti-roll bar provides better results than the previous model. Further research also must be conducted into determining better constraints for the roll-bar model. Work with this model was ceased, as it would require significant time and resources to configure and constrain a more accurate roll bar in the 2000P model, and this was outside of the scope of the project.

B.4 Conclusions

Concerns arose with the anti-roll bar model and constraints in the C2500 vehicle model. The complicated constraints applied to the anti-roll bar in the physical vehicle were insufficiently modeled. As such, the joint models were reviewed in the model, and a C2500 roll bar was modeled using solid elements for further testing. In future simulations with this vehicle, further research should be conducted on the constraints on the actual anti-roll bar and the various methods to implement those constraints into the model.

B.5 References

B-1. Boesch, D.A., *Front Suspension and Tire Modeling – For Use in Culvert Grate Impact Simulation*, Master's Thesis presented to the College of Engineering, University of Nebraska-Lincoln, April 2004.

B-2. Shreve, R.H. *Vehicle Suspension Including Anti-Roll Bar Assembly*. Patent No. 3218053, Filed Oct 26, 1962.

B-3. Gillespie, T.D. *Fundamentals of Vehicle Dynamics*. Society of Automotive Engineers: 1992.

B-4. Caliskan, K., *Automated Analysis of Anti-Roll Bars*, A Thesis presented to the Middle East Technical University, Cancaya Ankara, Turkey, September 2003.

B-5. Bosch, R., Bosch Automotive Handbook. Wiley: Germany, 7th Ed, 2007, pp. 780-786, et.

B-6. Reid, J.D., and Coon, B.E. *Finite Element Modeling of Cable Hook bolts*. 7th International LS-DYNA Conference. Lincoln Nebraska.